CENTRALE LYON

N° d'ordre NNT: 2026ECDL0013

THÈSE DE DOCTORAT DE L'ÉCOLE CENTRALE DE LYON

École Doctorale N° 162
MEGA - Mécanique, Énergétique, Génie Civil, Acoustique

Spécialité de doctorat : Acoustique

Soutenue publiquement le 18 mai 2026, par
Giovanni COCO

Propagation of Shock Waves Generated by an Unducted Single Fan: Acoustic Signature on the Fuselage

---

Devant le jury composé de

GERVAIS, Yves Université de Poitiers	Professeur	**Président**
COTTÉ, Benjamin ENSTA Paris	Maître de conférences HDR	**Rapporteur**
AVALLONE, Francesco Politecnico di Torino	Professeur	**Rapporteur**
BAILLY, Christophe École Centrale de Lyon	Professeur	**Directeur de thèse**
DRAGNA, Didier École Centrale de Lyon	Maître de conférences HDR	**Co-Directeur de thèse**
DE LABORDERIE, Hélène Safran Aircraft Engines	Docteure Ingénieure	**Co-Encadrante**

«In real life, mistakes are likely to be irrevocable. Computer simulation, however, makes it economically practical to make mistakes on purpose. If you are astute, therefore, you can learn much more than they cost.»

John McLeod

Abstract

The transition toward sustainable aviation has intensified interest in unducted aero-engines as a means of achieving substantial reductions in fuel consumption. The absence of a conventional engine nacelle in such configurations, however, removes a primary location for acoustic treatment and allows non-linear acoustic fluctuations generated at blade tips to propagate directly toward the aircraft fuselage. Existing aeroacoustic prediction methods often rely on linear acoustic analogies that neglect non-linear propagation effects or require computationally expensive body-fitted meshes to account for installation phenomena.

The objective of this dissertation is to develop and validate a high-fidelity numerical framework for predicting the acoustic signature induced by an unducted single fan engine on the fuselage, with particular emphasis on non-linear propagation and installation effects. The work addresses key methodological challenges related to robust CFD/CAA coupling and the efficient representation of rigid boundaries within Cartesian computational domains.

The proposed framework is based on a three-dimensional non-linear Euler solver employing high-order, low-dispersion numerical schemes combined with a dedicated shock-capturing strategy. A major contribution of this thesis is the development of a volumetric source method that enables the injection of prescribed acoustic fields from analytical solutions or independent flow simulations without generating spurious reflections. In addition, a novel reflection approach is introduced to model the fuselage as a perfectly rigid obstacle through forcing terms in the momentum equations, enabling accurate boundary treatment on uniform Cartesian grids.

Application of the developed tools provides new physical insight into the mechanisms governing fuselage noise. The results indicate that non-linear propagation effects lead to a limited reduction in sound pressure levels for upstream-propagating waves, whereas refraction by the fuselage boundary layer represents the dominant factor shaping the acoustic signature. Parametric analyses further show that shielding effectiveness increases monotonically with boundary layer thickness and that laminar velocity profiles yield substantially higher attenuation than turbulent profiles.

Overall, the findings suggest that conventional linear approaches may overestimate forward-fuselage noise levels and demonstrate the relevance of boundary layer characterization in installed noise prediction. The numerical framework established in this work offers an efficient and reliable tool for the aeroacoustic analysis and preliminary design of future unducted propulsion systems.

Keywords: non-linear propagation, computational aeroacoustics, shock-waves, unducted single fan, non-linear Euler equations, volumetric source terms

Résumé

La transition vers une aviation durable a renforcé l'intérêt pour les architectures de propulsion non carénées, capables de réduire significativement la consommation de carburant. L'absence de nacelle dans ces configurations supprime toutefois un emplacement privilégié pour les traitements acoustiques et permet aux ondes de choc générées aux extrémités transsoniques des pales, communément appelées "buzz-saw noise", de se propager directement vers le fuselage. Les méthodes actuelles de prédiction aeroacoustique reposent fréquemment sur des formulations linéaires négligeant les effets de propagation non linéaire ou nécessitent des maillages conformes coûteux pour modéliser les effets d'installation.

L'objectif de cette thèse est de développer et de valider un cadre numérique haute fidélité destiné à la prédiction de la signature acoustique d'une soufflante non carénée sur le fuselage, en prenant en compte les effets de propagation non linéaire et d'installation. Le travail répond à des enjeux méthodologiques majeurs liés au couplage robuste CFD/CAA et à la modélisation efficace de frontières rigides dans des domaines de calcul cartésiens.

Le cadre proposé repose sur un solveur tridimensionnel des équations d'Euler non linéaires, utilisant des schémas numériques d'ordre élevé à faible dispersion, associés à une stratégie dédiée de capture des chocs. Une contribution majeure de cette thèse est le développement d'une méthode de sources volumiques permettant l'injection de champs acoustiques prescrits issus de solutions analytiques ou de simulations d'écoulement indépendantes, sans génération de réflexions parasites. En complément, une nouvelle méthode de réflexion est proposée pour modéliser le fuselage comme un obstacle parfaitement rigide au moyen de termes sources dans les équations de quantité de mouvement, assurant un traitement précis des frontières sur des grilles cartésiennes uniformes.

L'application de ces outils met en évidence que les effets de propagation non linéaire n'entraînent qu'une réduction limitée des niveaux de pression acoustique pour les ondes se propageant vers l'amont, tandis que la réfraction induite par la couche limite du fuselage constitue le mécanisme dominant de façonnement de la signature acoustique. Les études paramétriques montrent en outre que l'efficacité du masquage acoustique augmente de manière monotone avec l'épaisseur de la couche limite et que les profils laminaires offrent une atténuation nettement supérieure à celle des profils turbulents.

Ces résultats suggèrent que les approches linéaires classiques peuvent surestimer les niveaux de bruit sur l'avant du fuselage et soulignent l'importance d'une caractérisation précise de la couche limite dans la prédiction du bruit installé. Le cadre numérique développé dans cette thèse constitue ainsi un outil fiable et efficace pour l'analyse aeroacoustique et la conception préliminaire des systèmes de propulsion non carénés de nouvelle génération.

Mots-clés : propagation non linéaire, aéroacoustique numérique, ondes de choc, soufflante non carénée, équations d'Euler non linéaires, termes sources volumiques

Remerciements

La thèse est une aventure, mais elle ne le serait pas sans les personnes que l'on rencontre tout au long du chemin. Je tiens tout d'abord à remercier mes directeurs de thèse, Christophe Bailly, Didier Dragna et Hélène de Laborderie, pour leur soutien constant tout au long de ce parcours, leur humanité et leur expertise scientifique inestimable. Je vous dois cette réussite ainsi que mon évolution, tant sur le plan professionnel que personnel.
Je remercie également tous les membres du jury de thèse : Yves Gervais, Benjamin Cotté et Francesco Avallone, d'avoir accepté d'évaluer mon travail de recherche et pour les échanges enrichissants lors de la soutenance.
Merci au LMFA qui m'a accueilli, ainsi qu'à toutes les personnes que j'ai croisées au cours de ces années. Merci à tous les permanents de l'équipe Acoustique pour les discussions passionnantes lors des cafés scientifiques, des pauses-café, des raclettes et des barbecues. Merci au personnel administratif pour la gestion de toutes les démarches administratives, des missions et des nombreux déplacements effectués pendant la thèse. Merci à tous les collègues de l'équipe Safran pour les échanges enrichissants et les précieux conseils.
Un remerciement tout particulier à toute la communauté des doctorants, postdoctorants et stagiaires que j'ai eu la chance de rencontrer durant ces trois années : je vous souhaite à tous un avenir fait de réussite, d'épanouissement et de satisfaction. Merci aux « anciens », partis vers d'autres horizons, qui m'ont immédiatement accueilli et initié à la vie du laboratoire : Jean, Léo, Simon, Alexis et Daniel.
Merci à tous ceux avec qui j'ai partagé une grande partie de cette aventure : Loïc (Gigi), toujours prêt à donner un coup de main ou à raconter une anecdote amusante ; Jules, pour ta spontanéité débordante, les éclats de rire et ton italien parfait, mamma mia ; Hugo, pour tes conseils essentiels sur l'utilisation et le choix des cartes de couleurs, dès le premier jour, et plus généralement pour ton soutien constant ; Igor pour être toujours à l'heure pour le café et le baby. Merci à Sandra pour sa gentillesse et pour avoir arrêté de boire des cappuccinos l'après-midi (du moins je l'espère), et à Sarp pour son indispensable kit d'urgence de jeux de société et ses délicieux desserts turcs.
Merci à Allan pour toutes nos conversations, toujours agréables et stimulantes, qu'il s'agisse d'observer le chantier du H10 ou de résoudre les problèmes techniques les plus complexes, pour lesquels tu trouvais toujours une solution (après tout, je ne fais que faire tourner des RANS).
Merci à Milo d'avoir supporté les élucubrations de ma dernière année de doctorat en tant que cobureau, pour l'accès à Gestor et pour tous les moments de rire (tu es le meilleur, ne l'oublie jamais). Merci à Pierre-Louis d'avoir été le meilleur pâtissier que le laboratoire ait jamais connu et pour les pauses baby-foot (appelle-moi si tu as besoin d'un petit 5-5). Merci à Emilian pour sa sensibilité et son ironie franche, toujours juste et souvent surprenante. Merci à Yuling, évidemment pour le bowling, mais aussi pour sa spontanéité et son énergie positive. Merci enfin aux derniers arrivés, Ajit, Thomas, Maud, Enzo et Julien : je vous souhaite le meilleur pour la suite. Merci également à toutes celles et ceux que je n'ai pas cités dans ces quelques lignes.
Merci à ceux qui, au fil de cette aventure, sont devenus des amis et des confidents. Merci à Laura (ciccia), qui sait toujours comment me redonner le sourire, et pour toutes les journées passées à ~~ne pas~~ travailler. Merci à Manju d'avoir toujours été présente, surtout lorsque j'en avais le plus besoin, pour ses créations artistiques et pour cette peinture sur toile qui me rappellera la maison où que j'aille. Merci à Emanuele, qui continue de me supporter et de me soutenir, même à distance.
Merci à mes amis de toujours : Giulio, Cesare, Chiara, Martina, Alessia, Giuseppe et Gabriele. Nous avons grandi ensemble, et cette étape importante est aussi la vôtre.
Enfin, merci à ma famille pour leur soutien indéfectible et tous les sacrifices au fil des années.
Je dédie le fruit de ce travail à ceux qui ne sont plus parmi nous, mais qui veillent sur moi depuis là-haut.

Table of contents

1 Introduction **1**

1.1 Global socio-economic context . . . 1

1.2 Aircraft Noise Sources . . . 3

1.3 Objectives . . . 5

2 Numerical Methods **7**

2.1 Governing Equations . . . 7

2.2 Finite difference schemes . . . 9

2.3 Selective filters . . . 11

2.4 Runge-Kutta algorithms . . . 13

2.5 Shock-capturing scheme . . . 15

2.6 Perfectly Matched Layer . . . 17

2.7 Conclusion . . . 20

3 A new method to prescribe incoming waves **23**

3.1 State of the art . . . 23

3.1.1 Acoustic Analogy Formulations . . . 23

3.1.2 Direct Use of Acoustic Data on Control Surfaces . . . 27

3.1.3 Method of Characteristics . . . 27

3.1.4 Volumetric Source Terms . . . 29

3.2 General Formulation . . . 32

3.3 Numerical Setup . . . 35

3.4 Results . . . 36

3.4.1 Oblique plane waves . . . 36

3.4.2 Sawtooth wave train . . . 39

3.4.3 2D Monopole with uniform flow . . . 43

3.4.4 3D Monopole with uniform mean flow . . . 47

3.5 Conclusion . . . 51

4 Reflection Method **53**

4.1 State of the art . . . 53

4.1.1 Immersed Boundary Methods . . . 53
4.1.2 Impedance Mismatch Method . . . 56
4.1.3 Equivalent Source Method . . . 56
4.1.4 Curvilinear Body-Fitted Grids . . . 56
4.1.5 Impedance and Transmittance Boundary Condition . . . 57
4.2 General formulation . . . 60
4.3 Results . . . 62
4.3.1 Characteristics Formulation . . . 63
4.3.2 Integral Formulation . . . 64
4.3.3 Integral Formulation with a Gaussian Distribution . . . 66
4.3.4 1D Pulse on a Perfectly Rigid Wall . . . 70
4.3.5 2D Pulse with Uniform Mean Flow . . . 74
4.3.6 Scattering of a Pulse by a Cylinder . . . 77
4.4 Conclusion . . . 80

5 Application to unducted single fan 81
5.1 Introduction . . . 81
5.2 Numerical setup . . . 83
5.3 Comparison with Ffowcs-Williams Hawkings . . . 85
5.4 Acoustic Signature on the Fuselage . . . 89
5.4.1 Non-linear Effects . . . 89
5.4.2 Boundary layer effects around the fuselage . . . 92
5.5 Conclusion . . . 106

6 Sensitivity to the source 109
6.1 Numerical Setup . . . 109
6.2 Comparison with Ffowcs-Williams Hawkings . . . 110
6.3 Acoustic Signature on the Fuselage . . . 112
6.4 Conclusion . . . 121

7 Conclusion 123

A Convolution 127
A.1 Calculation for S_1 . . . 127
A.2 Calculation for S_2 . . . 128
A.3 Total acoustic pressure field . . . 129
A.4 Integral calculation . . . 129

B N-wave injection 131

C Integral calculation for the reflection method **133**

C.1 Calculation of p_2 and p_3 133

C.2 Calculation of I 135

D Boundary conditions verification **137**

E Verification of acoustic pressure on the fuselage **139**

1 Introduction

This chapter presents the socio-economic and scientific context in which this thesis is situated. It first examines current trends in the aviation market, the emerging needs of the near future, and the importance of developing new technologies to address these challenges and comply with increasingly stringent regulations. The discussion then addresses the main noise-generation mechanisms in aircraft, with particular emphasis on the unducted single fan configuration. Finally, the objectives of the thesis and the structure of the present manuscript are outlined.

1.1 Global socio-economic context

The air traffic environment is constantly growing and evolving. According to the International Air Transport Association (IATA) report [1], the global economy is growing at a rate of about 3 percent per year. Despite some setbacks dictated by the Covid-19 pandemic first, and the war in Ukraine later, which impacted monetary policies and financial sector vulnerabilities, the number of global air passengers is still expected to continue growing.

As shown in Figure 1.1, three different scenarios are assumed: a basic one that is equivalent to today's; a more pessimistic one in the case of more protectionist policies, deterioration of the geopolitical environment and greater policy instability; and a more optimistic one with more favorable macro-economic conditions. In all three cases, a more or less pronounced increase in passenger numbers is expected regardless. Even in the worst-case scenario, the number of passengers could increase from 4 billion in 2025 to nearly 6 billion in 2040, while the most liberal scenario would even reach more than 9 billion passengers. All of this, of course, translates into an increase in air traffic, with a consequent rise in emissions of pollutants and noise produced.

This increase is also partly due to the development of air transport in emerging countries, and the center of gravity of air traffic is gradually shifting to regions in Asia, as illustrated in Fig. 1.2. This continued growth implies a whole range of economic, regulatory and environmental consequences. The increasing accessibility of air travel will lead to a decrease in the average

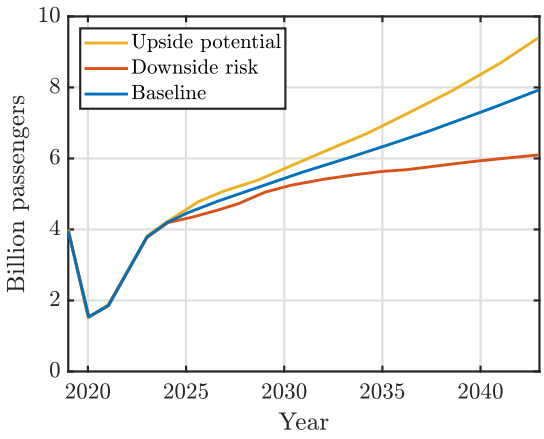

Figure 1.1: Number of global air passengers in billions: evolutionary estimate over time under three different scenarios [1].

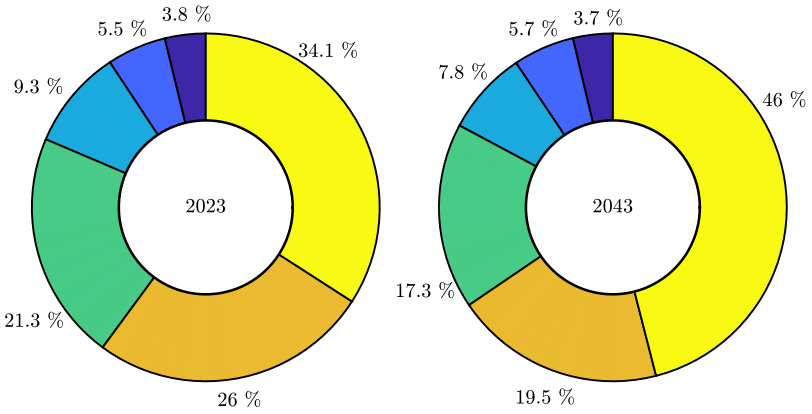

Figure 1.2: Regional passenger traffic, share of total in %, 2023 and 2043 forecast [1]. Legend: Africa, Middle East, Latin America & Caribbean, North America, Europe, Asia Pacific

ticket price, and this will necessarily have to translate into a reduction in the cost of operations to try to maintain some profit. In addition, more efficient engines with lower thrust specific fuel consumption will be needed. From an environmental point of view, efforts will have to be made to reduce emissions of air pollutants and noise. This implies increasingly greener and quieter aircraft.

Within the framework of regulations imposed by the International Civil Aviation Organization (ICAO) [2], it becomes critically important to develop increasingly high-performance technologies that can adequately respond to the increasingly stringent level of regulations in place. Focusing now in more detail in the field of acoustics, ICAO distinguishes between two types of noise: community noise, i.e., that relating to people living near airport areas, and ramp noise, relating more specifically to ramp operators during aircraft operations near the runway.

ICAO standards define the Effective Perceived Noise Level (EPNL), a metric that includes a psychoacoustic correction accounting for the frequency-dependent sensitivity of the human ear, as well as the duration of exposure to peak Sound Pressure Levels. EPNL is used for aircraft noise certification and serves to assess the noise perceived on the ground during specific flight phases (Approach, Cutback, and Sideline). It therefore characterizes the external noise footprint of the aircraft during take-off and landing and is not intended to describe cabin noise conditions. Furthermore, airports may impose local regulations that are often more stringent than current ICAO standards. For instance, within the European Union [3], all workers exposed to levels above 80 dBA must be provided with appropriate hearing protection, and the use of such protection becomes mandatory when the daily average exposure exceeds 85 dBA.

With regard to the acoustic environment inside the cabin, other regulatory requirements and design criteria apply. These include mandatory constraints on the intelligibility of emergency announcements, as well as limits related to occupational exposure for flight and cabin crew. In addition, aircraft manufacturers define internal acoustic targets as part of their product design and marketing strategy, while airlines may establish their own cabin noise objectives to ensure a high level of environmental comfort for passengers.

Noise thus remains the number one cause of complaints for all residents in airport areas. This leads local authorities to impose noise charges or flight restrictions if a particular aircraft does not meet local standards. All this thus plays a key role for both airlines and manufacturers, for whom fees still represent a financial loss, while flight restrictions limit their business. Therefore, it becomes increasingly important to well understand the mechanisms of noise generation and sound propagation for an aircraft, and to develop new technologies to mitigate it.

1.2 Aircraft Noise Sources

Multiple aircraft components contribute to overall noise generation, with their relative importance depending on the aircraft architecture, geometry, and flight phase. In general, these sources contribute both to the external noise footprint of the aircraft and, through different transmission

paths, to the noise perceived inside the cabin. The main noise sources typically include the propulsion system, high-lift devices, landing gear, and aerodynamic surfaces such as wings, tail, and fuselage. Figure 1.3 provides a schematic overview of these various noise sources and their relative locations on the aircraft.

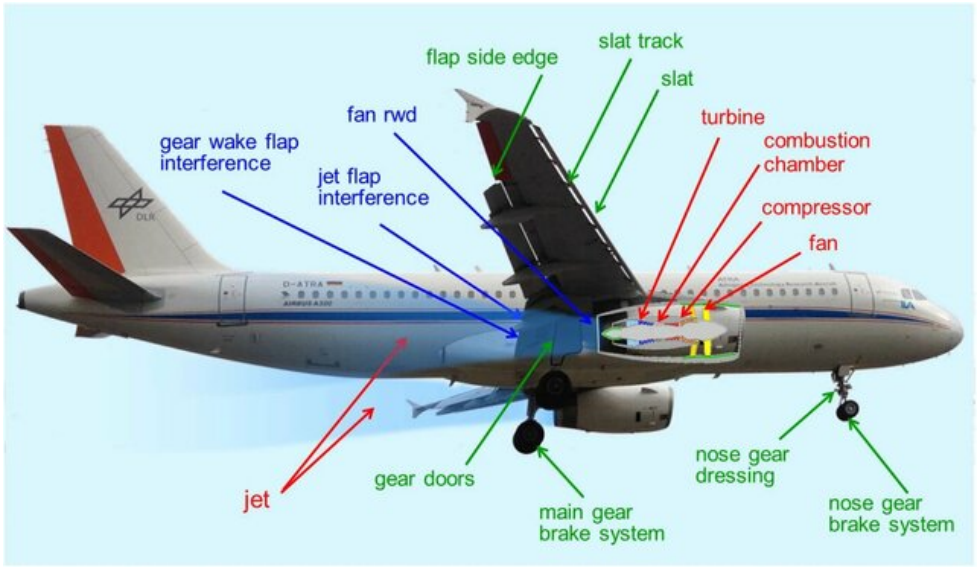

Figure 1.3: Aircraft noise sources and interactions, ©Henri Siller and Jan Delfs, DLR, 2019.

From the perspective of the acoustic environment inside the cabin, however, the dominant contributors differ from those primarily governing external certification metrics. In cruise conditions, the boundary layer developing along the fuselage constitutes a major broadband excitation source. The associated unsteady wall pressure fluctuations excite the fuselage structure, which in turn radiates noise into the cabin through structural transmission paths.

In addition, onboard systems play a significant role in cabin acoustics. The environmental control system (ECS), including air conditioning packs and ventilation ducts, generates both broadband and tonal noise components that directly affect passenger comfort. Contributions also arise from the propulsion system, transmitted through the airframe structure, and from airframe devices during approach and landing phases. Nevertheless, for typical cruise conditions, boundary layer excitation, engine-induced noise transmission through the airframe, and internal systems such as the ECS are generally the primary contributors to the noise perceived by passengers inside the cabin.

In the context outlined in Section 1.1, there is a clear need for innovative solutions to meet increasingly stringent regulatory requirements. One such solution is the unducted single fan configuration, which can significantly reduce fuel consumption relative to conventional architectures. The unducted single fan concept features an unshrouded propulsion system composed of a propeller module coupled with a conventional gas generator that houses the turbomachinery stages. By removing the nacelle and operating at higher bypass ratios, this

configuration offers significant improvements in propulsive efficiency. However, the absence of an acoustic liner and duct confinement fundamentally alters the engine noise radiation mechanisms.

Unducted single fan noise sources

In an unducted single fan engine, the dominant noise sources are primarily associated with the rotating blade rows. Unlike a conventional turbofan, where the fan and core are enclosed within a nacelle, an unducted single fan lacks a duct and acoustic liner treatments, and its acoustic signature is therefore largely governed by rotor aerodynamics and rotor-stator interactions.
The acoustic field generated by an unducted single fan occupies different regions of the spectrum and includes both tonal and broadband components. Tonal noise is dominated by harmonics of the blade passing frequency (BPF) associated with the rotor. Broadband noise is mainly associated with turbulence-blade interaction and trailing-edge noise.
A specific feature of unducted single fan propulsion systems operating at high rotational speeds is the possible onset of transonic flow near the blade tips, especially in cruise. In such conditions, shockwave formation might occur, generating non-linear pressure fluctuations. These fluctuations will progressively be dampened by non-linear effects. The resulting pressure field will contribute to the acoustic excitations on the fuselage structure at the BPF and its harmonics.
The relative importance of each mechanism depends on flight phase and operating condition.
A more detailed classification of unducted single fan noise sources can be organized as follows:

- *Harmonic noise*: Periodic components associated with blade rotation, including thickness noise, steady loading noise, non-linear fluctuations and rotor-stator interaction tones. The spectrum consists of discrete harmonics at integer multiples of the BPF.
- *Broadband noise*: Generated by turbulence-blade interaction, boundary-layer development, and trailing-edge scattering. This component spreads over a wide frequency range.

Installation effects are especially important for unducted single fan architectures. The noise sources are thus modified by the presence of the fuselage, pylon, and empennage, changing the acoustic radiation pattern.
Among the various unducted single fan noise-generation mechanisms described above, the present thesis focuses exclusively on the propagation of non-linear fluctuations and their contribution to fuselage acoustic excitation.

1.3 Objectives

The primary objective of this thesis is to predict the propagation of shock waves generated by the unducted single fan engine onto the aircraft fuselage. This analysis requires accounting for non-linear effects in acoustic wave propagation as well as the influence of the fuselage boundary

layer and fuselage scattering. Acoustic wave propagation is modeled using numerical simulations based on the solution of the non-linear Euler equations in conservative form.
Three principal areas of development are addressed in this work:

- The development of a numerical method for introducing rotating shock waves into aeroacoustics simulations through volumetric source terms.
- The development of a three-dimensional non-linear Euler solver for shockwave propagation within the computational domain.
- The development of a numerical approach to model the presence of the fuselage in the computational domain, assuming a perfectly rigid and reflective wall boundary condition.

The structure of the manuscript is organized as follows. Chapter 2 presents the governing nonlinear Euler equations and describes the numerical methods employed, including finite-difference discretization, time integration, and boundary condition treatments. Chapter 3 introduces an original method developed in this thesis for generating waves that propagate exclusively outward from a control surface of arbitrary geometry. This method is validated using three academic test cases and subsequently applied to the unducted single fan configuration. Chapter 4 presents a second numerical approach developed to model a rigid wall within the computational domain using volumetric source terms that account for the wall pressure field; this method is also validated through academic test cases and further applied in the unducted single fan application case. Finally, Chapter 5 addresses the unducted single fan application, examining nonlinear effects in shockwave propagation induced by blade rotation, the resulting acoustic signature on the fuselage, and the influence of the boundary layer on the perceived noise.

2 Numerical Methods

This chapter provides a comprehensive description of the numerical methodology employed throughout the doctoral research, focusing on accuracy, stability, and computational efficiency for acoustic simulations. The core governing equations are the full three-dimensional non-linear Euler equations in conservative form, chosen specifically to model acoustic wave propagation and assess non-linear effects. Spatial discretization relies on optimized central finite difference schemes constructed to minimize dispersion and dissipation errors. Time advancement utilizes a low-storage, explicit six-stage optimized Runge-Kutta algorithm. A selective filter is used to damp grid-to-grid oscillations, and a shock-capturing scheme is implemented to selectively introduce dissipation near shock fronts. Perfectly Matched Layers are implemented as effective absorbing boundary conditions.

2.1 Governing Equations

The full non-linear Euler equations [4] are solved to model acoustic waves propagation. They are a simplification of the Navier-Stokes equations, in which thermal and viscous effects are neglected. These equations are expressed in conservative form, in terms of the conserved quantities: mass, momentum, and energy. The equations are written in three-dimensional Cartesian coordinates as follows:

$$\frac{\partial \boldsymbol{U}}{\partial t} + \frac{\partial \boldsymbol{E}}{\partial x} + \frac{\partial \boldsymbol{F}}{\partial y} + \frac{\partial \boldsymbol{G}}{\partial z} = 0 \tag{2.1}$$

with

$$\boldsymbol{U} = (\rho, \rho u, \rho v, \rho w, \rho e_t) \tag{2.2}$$

$$\boldsymbol{E} = \Big(\rho u, \rho u^2 + p, \rho uv, \rho uw, u\left(\rho e_t + p\right)\Big) \tag{2.3}$$

$$\boldsymbol{F} = \Big(\rho v, \rho uv, \rho v^2 + p, \rho vw, v\left(\rho e_t + p\right)\Big) \tag{2.4}$$

$$\boldsymbol{G} = \Big(\rho w, \rho uw, \rho vw, \rho w^2 + p, w\left(\rho e_t + p\right)\Big) \tag{2.5}$$

where t denotes time; x, y, and z represent the spatial coordinates; $\boldsymbol{U}$ is the vector of conservative variables; $\boldsymbol{E}$, $\boldsymbol{F}$, and $\boldsymbol{G}$ are the flux vectors; ρ is the density; u, v, and w are the velocity components in the x-, y-, and z-directions, respectively; p is the pressure; and e_t is the total energy per mass unit, given by:

$$\rho e_t = \frac{p}{\gamma - 1} + \frac{1}{2}\rho\left(u^2 + v^2 + w^2\right) \tag{2.6}$$

with γ the ratio of specific heats set to 1.4, assuming that air behaves as in ideal gas.
The decision not to linearize Euler's equations for acoustic wave propagation arises from the focus of this work on shock waves generated by an unducted single fan. The objective is to assess the non-linear effects during propagation and their impact on the resulting sound pressure levels.
In this work, the non-linear Euler equations are solved in perturbative form, as an exact formulation of the primitive system in Eq. (2.1). To do this, the conservative field vector $\boldsymbol{U}$ and the flux vectors $\boldsymbol{E}$, $\boldsymbol{F}$ and $\boldsymbol{G}$ are decomposed into their mean $\bar{(\cdot)}$ and oscillatory $(\cdot)'$ components:

$$\boldsymbol{U} = \bar{\boldsymbol{U}} + \boldsymbol{U'} \tag{2.7}$$

$$\boldsymbol{E} = \bar{\boldsymbol{E}} + \boldsymbol{E'} \tag{2.8}$$

$$\boldsymbol{F} = \bar{\boldsymbol{F}} + \boldsymbol{F'} \tag{2.9}$$

$$\boldsymbol{G} = \bar{\boldsymbol{G}} + \boldsymbol{G'} \tag{2.10}$$

where the shorthand notations $\bar{\boldsymbol{E}} = \boldsymbol{E}(\bar{\boldsymbol{U}})$, $\bar{\boldsymbol{F}} = \boldsymbol{F}(\bar{\boldsymbol{U}})$ and $\bar{\boldsymbol{G}} = \boldsymbol{G}(\bar{\boldsymbol{U}})$ have been used, and the mean fields are defined as:

$$\bar{\boldsymbol{U}} = \left(\rho_0, \rho_0 u_0, \rho_0 v_0, \rho_0 w_0, (\rho e_t)_0\right) \tag{2.11}$$

$$\bar{\boldsymbol{E}} = \left(\rho_0 u_0, \rho_0 u_0^2, \rho_0 u_0 v_0, \rho_0 u_0 w_0, u_0\left((\rho e_t)_0 + p_0\right)\right) \tag{2.12}$$

$$\bar{\boldsymbol{F}} = \left(\rho_0 v_0, \rho_0 u_0 v_0, \rho_0 v_0^2, \rho_0 v_0 w_0, v_0\left((\rho e_t)_0 + p_0\right)\right) \tag{2.13}$$

$$\bar{\boldsymbol{G}} = \left(\rho_0 w_0, \rho_0 u_0 w_0, \rho_0 v_0 w_0, \rho_0 w_0^2, w_0\left((\rho e_t)_0 + p_0\right)\right) \tag{2.14}$$

Accordingly, Eq. (2.1) is rewritten as follows:

$$\frac{\partial \boldsymbol{U'}}{\partial t} + \frac{\partial \boldsymbol{E'}}{\partial x} + \frac{\partial \boldsymbol{F'}}{\partial y} + \frac{\partial \boldsymbol{G'}}{\partial z} = 0 \tag{2.15}$$

The mean flow is further assumed to be stationary and to satisfy the Euler equations throughout the computational domain:

$$\frac{\partial \bar{\boldsymbol{E}}}{\partial x} + \frac{\partial \bar{\boldsymbol{F}}}{\partial y} + \frac{\partial \bar{\boldsymbol{G}}}{\partial z} = 0 \tag{2.16}$$

2.2 Finite difference schemes

Throughout the research work, all simulations were carried out employing optimized central finite difference schemes for spatial derivation [5]. These schemes are constructed by minimizing dispersion and dissipation errors in the wavenumber space up to $k\Delta x = \pi/2$, where k is the wavenumber and Δx is the spacing of a uniform mesh. This corresponds to an accuracy of up to four points per wavelength. This optimization provides distinct advantages over standard schemes, particularly when considering the accurate calculation of short waves.

To explain the construction and functioning of the schemes employed, one considers a generic variable u and writes the spatial derivative $\partial u/\partial x$ at a point x_0. The derivative can be approximated using a central finite-difference scheme with a $2N+1$ points stencil, which reads:

$$\frac{\partial u}{\partial x}(x_0) = \frac{1}{\Delta x}\sum_{j=-N}^{N} a_j u(x_0 + j\Delta x) \tag{2.17}$$

where the coefficients a_j satisfy the relation $a_j = -a_{-j}$ to avoid dissipation effects.
For a standard scheme, the coefficients a_j are determined by canceling terms in the Taylor series expansion of Eq. (2.17) to achieve maximum order. For instance, standard schemes with 9, 11, and 13 points (denoted as FDs9p, FDs11p, and FDs13p, respectively) have orders of 8, 10, and 12, respectively.
In contrast, the optimized schemes used during the research are developed starting from dispersion properties. The effective wavenumber k^* of the scheme is obtained by applying a spatial Fourier transform to Eq. (2.17):

$$k^*\Delta x = 2\sum_{j=1}^{N} a_j \sin(jk\Delta x) \tag{2.18}$$

Dispersion error arises from the discrepancy between the effective wavenumber k^* and the exact wavenumber k. Optimized schemes using 9, 11, and 13 points (denoted as FDo9p, FDo11p, and FDo13p, respectively) are designed to minimize this error for a wide range of wavenumbers, extending up to $k\Delta x = \pi/2$. These schemes are of fourth order, and their coefficients a_j are determined by minimizing the integral error:

$$\int_{\ln(k\Delta x)_l}^{\ln(k\Delta x)_h} \left|k^*\Delta x - k\Delta x\right| \mathrm{d}\left(\ln(k\Delta x)\right) \tag{2.19}$$

The wavenumber limits are set as $\ln(k\Delta x)_l = \pi/16$, and $\ln(k\Delta x)_h = \pi/2$ for FDo9p and FDo11p, with the upper limit equal to $3\pi/5$ for FDo13p.
Figure 2.1 illustrates the relationship between the effective wave number k^* and the exact wave number k for the optimized schemes. The black line denotes the reference relation $k^*\Delta x = k\Delta x$. The optimized schemes exhibit reduced dispersion, as evidenced by their close agreement with this line. Increasing the number of points in the finite-difference stencil further decreases

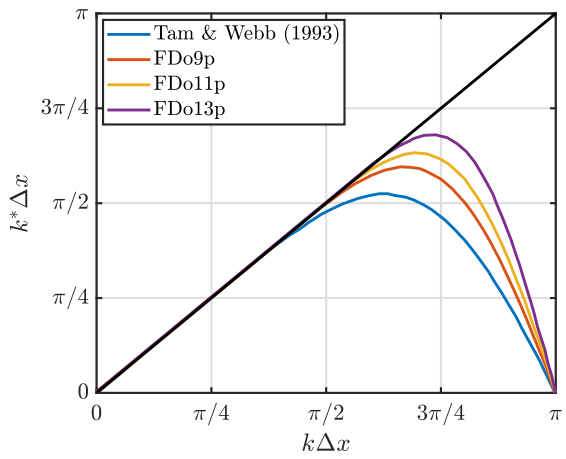

Figure 2.1: $k^*\Delta x$ versus $k\Delta x$ for the optimized finite-difference schemes [5] and for the DRP scheme of Tam and Webb [6]

dispersion errors, as demonstrated by the progression from the Tam and Webb [6] Dispersion-Relation-Preserving (DRP) scheme to the FDo13p scheme. It is noted that none of the schemes accurately resolves waves with $k\Delta x = \pi$, corresponding to the Shannon frequency of two points per wavelength.

These optimized schemes demonstrate significant advantages over their standard counterparts. The dispersion error is reduced, as shown in Fig. 2.2. Optimized schemes exhibit substantially lower dispersion errors for short waves with $k\Delta x > \pi/4$, especially near $k\Delta x = \pi/2$ where the reduction can be over an order of magnitude, compared to standard schemes.

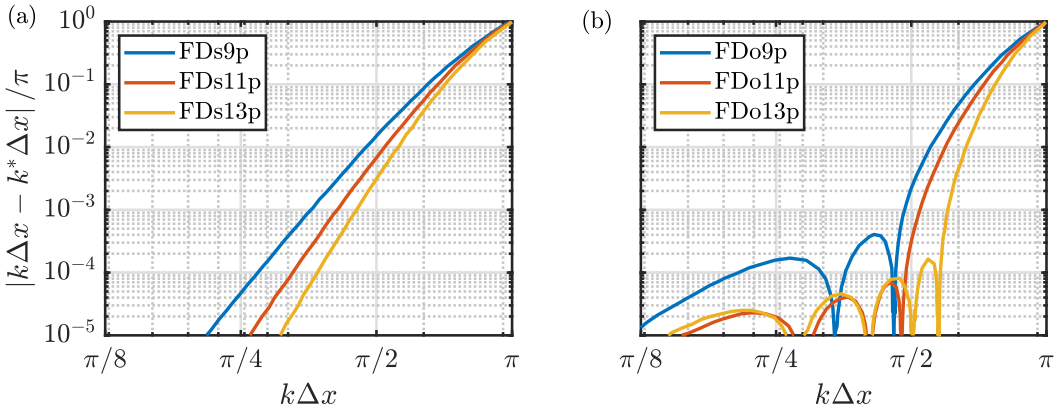

Figure 2.2: Dispersion error for (a) the three standard finite difference-schemes and (b) the three optimized finite-difference schemes [5].

Furthermore, when assessed against specific error criteria, the optimized schemes consistently display superior accuracy limits compared to standard schemes utilizing the same stencil size. Notably, FDo11p and FDo13p effectively capture waves with approximately four points per wavelength. It has been demonstrated that optimized schemes, particularly FDo11p and FDo13p,

exhibit higher efficiency, signifying better accuracy for a given computational cost, compared to standard schemes. In this work, the FDo11p scheme is employed.

2.3 Selective filters

Although very efficient and accurate, central finite-difference schemes fail to resolve grid-to-grid oscillations, which can destabilize numerical computations. Selective filters effectively mitigate this issue by introducing artificial dissipation without disrupting physical long waves.
A central filter with a $2N+1$ point stencil applied to a generic variable u on a uniform mesh yields:

$$u^f(x_0) = u(x_0) - \sigma_d D_u(x_0), \quad \text{with } D_u(x_0) = \sum_{j=-N}^{N} d_j u(x_0 + j\Delta x) \tag{2.20}$$

where the relation $d_j = d_{-j}$ ensures no dispersion and σ_d is a constant between 0 and 1.
Standard selective filters derive coefficients d_j by canceling terms in the Taylor series expansion of the filter in Eq. (2.20) for $k\Delta x \to 0$, aiming to maximize the order of accuracy.
Optimized selective filters are instead constructed in Fourier space. The spatial Fourier transform of the filter in Eq. (2.20) yields:

$$D_k(k\Delta x) = d_0 + \sum_{j=1}^{N} 2d_j \cos(jk\Delta x) \tag{2.21}$$

with $D_k(k\Delta x = 0) = 0$ and $D_k(k\Delta x = \pi) = 1$ for normalization.
The function $D_k(k\Delta x)$ quantifies dissipation at different wavenumbers. Optimized filters are designed by minimizing $D_k(k\Delta x)$ within the range $\pi/16 \leq k\Delta x \leq \pi/2$.
The coefficients d_j are optimized by minimizing the integral dissipation:

$$\int_{\ln(\pi/16)}^{\ln(\pi/2)} D_k(k\Delta x)\, \mathrm{d}\left(\ln(k\Delta x)\right) \tag{2.22}$$

Two additional conditions are imposed: $D_k > 0$ to ensure purely dissipative behavior and limitations on the variation of D_k with respect to $k\Delta x$ to control damping function behavior.
The damping functions for the optimized selective filters are shown in Fig. 2.3. Long waves experience negligible dissipation, whereas dissipation becomes significant for wavenumbers approaching $k\Delta x = \pi$. Increasing the number of points N in the selective filter from 3 to 6 yields a more selective filtering behavior.
Figure 2.4 presents a logarithmic-scale comparison between standard and optimized selective filters over the range $\pi/8 \leq k\Delta x \leq \pi$. Optimized selective filters offer several key advantages with respect to the standard ones. They are less dissipative for short waves with $k\Delta x > \pi/4$, especially near $k\Delta x = \pi/2$, where the difference compared to standard filters is substantial. Furthermore, optimized filters demonstrate higher accuracy limits for both weakly and negligibly

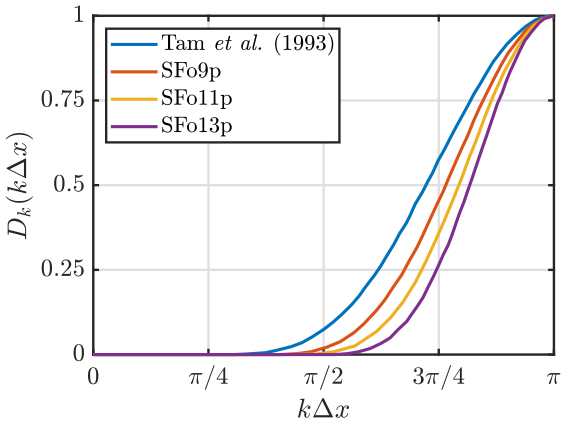

Figure 2.3: Damping functions for the optimized selective filters [5] and the optimized filter proposed by Tam *et al.* [7].

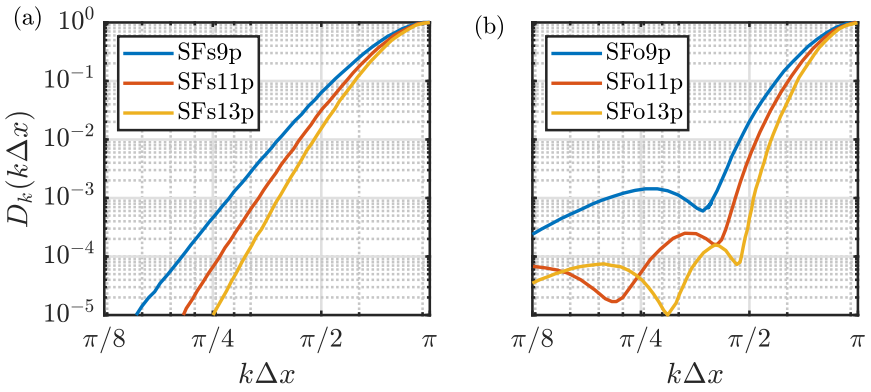

Figure 2.4: Damping functions for (a) the standard selective filters and (b) the optimized selective filters [5].

dissipated wavenumbers. This implies they preserve a broader range of wavenumbers compared to standard filters. Furthermore, similar to optimized finite-difference schemes, optimized filters demonstrate superior numerical efficiency. This is evident in the lower values of the product of accuracy limits and the number of stencil points, suggesting improved accuracy for a fixed computational cost.

Throughout this work, the optimized selective filter centered on 11 points (SFo11p) is employed [5]. No selective filtering is applied at the boundaries of the computational domain, where Perfectly Matched Layers [8] are used instead.

The optimized central finite difference schemes and selective filters employed in this work provide a robust framework for spatial discretization. By minimizing dispersion and dissipation errors, these methods effectively capture a wider range of wavenumbers with higher accuracy and numerical efficiency compared to standard schemes.

2.4 Runge-Kutta algorithms

For time integration, the choice has been made to use a low-storage, explicit Runge-Kutta (RK) algorithm, specifically a six-stage optimized scheme (RKo6s) developed by Berland *et al.* [9]. This choice is motivated by the need for accuracy and efficiency in solving the time-dependent governing equations. Actually, explicit RK algorithms offer a convenient and widely used method for time integration. In the context of Computational Fluid Dynamics (CFD) and Computational Aeroacoustics (CAA), low-storage RK algorithms are particularly attractive as they minimize memory requirements. These algorithms achieve this by utilizing only two storage locations per variable at each sub-step.

To derive the formulation of a p-stage explicit RK algorithm, one considers the following differential equation:

$$\frac{\partial u}{\partial t} = F\left(u\right) \tag{2.23}$$

with $F(u)$ a function of u.

The algorithm for advancing the solution u from the nth to the $(n+1)$th time step is given by:

$$u^0 = u^n \tag{2.24}$$

$$u^l = u^n + \alpha_l \Delta t F(u^{l-1}) \text{ for } l = 1, ..., p \tag{2.25}$$

$$u^{n+1} = u^p \tag{2.26}$$

where u^n represents the solution at the nth iteration, Δt is the time step, and α_l are the coefficients specific to the algorithm.

For linear $F(u)$, the algorithm can be expressed as:

$$u^{n+1} = u^n + \sum_{j=1}^{p} \prod_{l=p-j+1}^{p} \alpha_l \Delta t^j \frac{\partial^j u^n}{\partial t^j} \tag{2.27}$$

where one defines $\gamma_j = \prod_{l=p-j+1}^{p} \alpha_l$.

For a standard p-stage RK scheme, one sets $\gamma_j = 1/j!$, for $j = 1, ..., p$, ensuring that the algorithm matches the Taylor series expansion of $u\left(t_n + \Delta t\right)$.

For an optimized RK algorithms, one wants to prioritize dispersion and dissipation properties for enhanced accuracy. Supposing a linear $F(u)$, the amplification factor G_{RK} of the RK algorithm can be determined by applying a temporal Fourier transform:

$$G_{RK}\left(\omega\Delta t\right) = \frac{\hat{u}^{n+1}\left(\omega\right)}{\hat{u}^{n}\left(\omega\right)} = 1 + \sum_{j=1}^{p} \gamma_j \left(\mathrm{i}\omega\Delta t\right)^j \tag{2.28}$$

where ω is the angular frequency.

To compare this with the exact amplification factor $\mathrm{e}^{\mathrm{i}\omega\Delta t}$, one can write $\left|G_{RK}\left(\omega\Delta t\right)\right| \mathrm{e}^{\mathrm{i}\omega^*\Delta t}$, with $|G_{RK}|$ the amplification rate and ω^* the effective angular frequency. The dissipation is then given by $1 - \left|G_{RK}\left(\omega\Delta t\right)\right|$, and the difference in phase is $\omega^*\Delta t - \omega\Delta t$.

The optimized six-stage RK algorithm (RKo6s) is constructed by minimizing both dissipation and dispersion errors up to an angular frequency of $\omega\Delta t = \pi/2$. This is a second-order algorithm that is defined by coefficients γ_j that minimize

$$\int_{\ln(\pi/16)}^{\ln(\pi/2)} \left(1 - \left|G_{RK}\left(\omega\Delta t\right)\right|\right) \mathrm{d}\big(\ln\left(\omega\Delta t\right)\big) + \int_{\ln(\pi/16)}^{\ln(\pi/2)} \left(\left|\omega^*\Delta t - \omega\Delta t\right| / \pi\right) \mathrm{d}\big(\ln\left(\omega\Delta t\right)\big) \tag{2.29}$$

while also satisfying these conditions for the dissipation rate:

$$\begin{cases} 1 - |G_{RK}| > 0 \\ \partial\left[\ln\left(1 - |G_{RK}|\right)\right] / \partial\left[\ln\left(\omega\Delta t\right)\right] \geq -5 \end{cases} \tag{2.30}$$

for $0 \leq \omega\Delta t \leq \pi$, similar to the constraints applied to the selective filters.

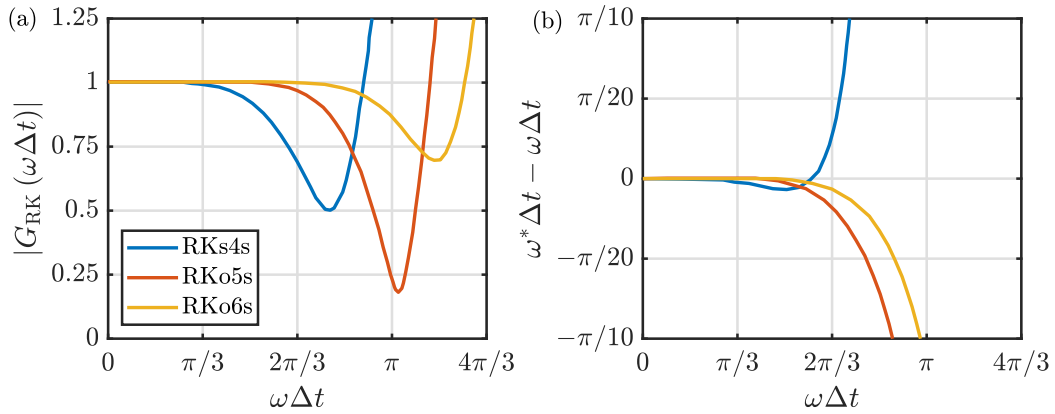

Figure 2.5: (a) Amplification rate and (b) difference in phase for the standard and the optimized Runge-Kutta schemes [5].

The optimized RK algorithms exhibit several significant advantages over the standard algorithm.

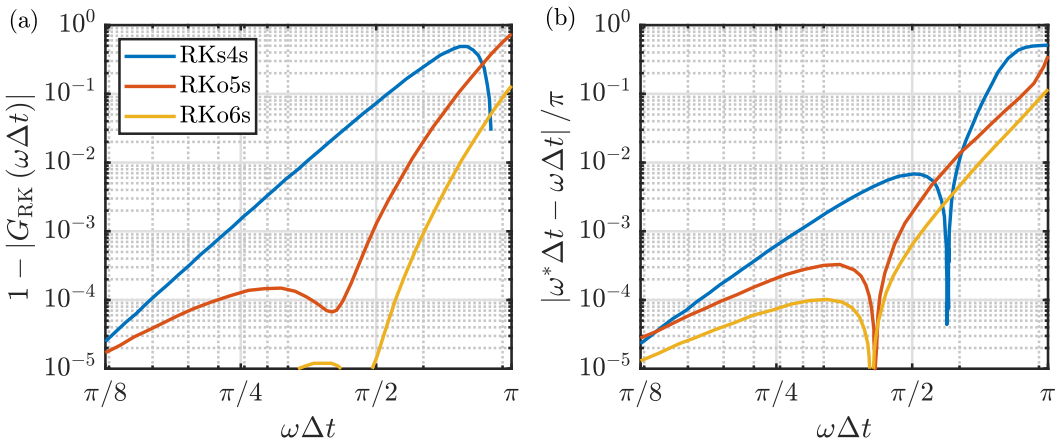

Figure 2.6: (a) Dissipation and (b) dispersion error for the standard and the optimized Runge-Kutta schemes [5].

The amplification rates and the difference in phase for the standard and the optimized Runge-Kutta schemes are shown in Fig. 2.5. The RKo6s algorithm demonstrates significantly lower dissipation and dispersion errors over a broader range of angular frequencies. This is particularly evident in the amplification rate remaining closer to unity and phase difference staying closer to zero compared to the standard scheme. Figure 2.6 presents the dissipation and dispersion errors on a logarithmic scale. The optimized schemes exhibit lower dissipation and dispersion than the standard scheme over the range $\pi/8 \leq \omega\Delta t \leq \pi$.

Furthermore, the optimized algorithm exhibits higher stability limits than the standard one, allowing for larger time steps without compromising stability. This enhanced stability, combined with their accuracy, contributes to its overall computational efficiency. Plus, when considering the trade-off between accuracy and computational cost, the optimized algorithms prove more efficient. They deliver higher accuracy for a given computational cost, making them a preferable choice, especially for long-time integration problems.

The use of a six-stage optimized Runge-Kutta algorithm (RKo6s) for time integration in this thesis is justified by its superior accuracy, stability, and numerical efficiency. The optimized algorithm effectively minimizes dissipation and dispersion errors, enabling accurate and efficient simulation of wave propagation phenomena.

2.5 Shock-capturing scheme

Shock-capturing filters are essential in numerical simulations when dealing with high-amplitude waves that lead to the formation of shock waves. These filters are employed alongside low-dispersion and low-dissipation numerical schemes to maintain numerical stability while preserving accuracy in representing the acoustic phenomena.

The primary motivation for using shock-capturing filters stems from the limitations of low-dissipation schemes in handling sharp gradients inherent in shock waves. These schemes,

often relying on centered finite differences, struggle to accurately represent the high-frequency components present in shocks. This inadequacy leads to spurious oscillations, known as Gibbs oscillations, near the shock front, which can destabilize the simulation and produce inaccurate results. Shock-capturing filters mitigate these oscillations by selectively introducing artificial dissipation in the vicinity of shocks.

The shock-capturing scheme used in this work is the one developed by Sabatini *et al.* [10], which is a direct evolution of the one developed by Bogey *et al.* [11]. This approach involves introducing artificial dissipation exclusively where required, specifically in the vicinity of shock fronts, ensuring that smooth regions of the solution remain unaffected. The methodology comprises two steps. First, the locations of discontinuities are identified using a shock sensor. Subsequently, a second-order filter in conservative form is applied, characterized by a strength parameter σ^{sc} that is significant in the vicinity of shock regions and negligible elsewhere. The sensor is specifically conceived for acoustic applications, and it is based on the smoothness indicators used in Weighted Essentially Non-Oscillatory (WENO) schemes [12, 13].

First of all, the following parameters are calculated:

$$\beta_0 = \frac{13}{12}\left(p'_{i-2} - 2p'_{i-1} + p_i\right)^2 + \frac{1}{4}\left(p'_{i-2} - 4p'_{i-1} + 3p'_i\right)^2 \tag{2.31}$$

$$\beta_1 = \frac{13}{12}\left(p'_{i-1} - 2p'_i + p'_{i+1}\right)^2 + \frac{1}{4}\left(p'_{i-1} - p'_{i+1}\right)^2 \tag{2.32}$$

$$\beta_2 = \frac{13}{12}\left(p'_i - 2p'_{i+1} + p'_{i+2}\right)^2 + \frac{1}{4}\left(3p'_i - 4p'_{i+1} + p'_{i+2}\right)^2 \tag{2.33}$$

The parameters β_k, with $k = 0, 1, 2$, are calculated using centered and non-centered finite difference approximations of the first and second derivatives of the pressure perturbation p'_i. They serve as indicators of the solution's regularity. From these, coefficients α_k and ω_k are computed as:

$$\alpha_k = \frac{1}{\left(\beta_k + \epsilon\right)^2} \tag{2.34}$$

$$\omega_k = \frac{\alpha_k}{\sum_l \alpha_l} \tag{2.35}$$

with $k = 0, 1, 2$ and $\epsilon = 10^{-18}$ to avoid division by zero.

Looking at Eq. (2.35), it can be easily shown that in regions without shock waves ω_k tends to $\frac{1}{3}$, since β_k is very small. The working principle of the shock detector, therefore, is to measure the deviation from this value. One therefore defines the coefficient r as:

$$r = \left(\sum_{k=0}^{2} \left|\omega_k - \frac{1}{3}\right|\right)^2 \tag{2.36}$$

Thus one calculates the filtering strength as:

$$\sigma_i^{\text{sc}} = \frac{\sigma_{\max}^{\text{sc}}}{2}\left(1 - \frac{r_{\text{th}}}{r} + \left|1 - \frac{r_{\text{th}}}{r}\right|\right) \tag{2.37}$$

with r_{th} a threshold value equal to 0.8.
By construction, the filter strength $\sigma_i^{\text{sc}} = 0$ in the areas without shock waves, that is for $r < r_{\text{th}}$, while it gradually grows up to $\sigma_{\max}^{\text{sc}} \in [0, 1]$ in the areas where the shock wave is detected.
To apply the filter in a conservative form, weighted averages are used to determine the filtering strengths at intermediate points:

$$\sigma_{i-1/2}^{\text{sc}} = \frac{1}{5}\left(2\sigma_{i-1}^{\text{sc}} + 2\sigma_i^{\text{sc}} + \sigma_{i+1}^{\text{sc}}\right) \tag{2.38}$$

$$\sigma_{i+1/2}^{\text{sc}} = \frac{1}{5}\left(\sigma_{i-1}^{\text{sc}} + 2\sigma_i^{\text{sc}} + 2\sigma_{i+1}^{sc}\right) \tag{2.39}$$

One can thus apply the filter on a conservative variable U such that:

$$U_i^{\text{sc}} = U_i - \left(\sigma_{i+1/2}^{\text{sc}} D_{i+1/2}^{\text{sc}} - \sigma_{i-1/2}^{\text{sc}} D_{i-1/2}^{\text{sc}}\right) \tag{2.40}$$

where $D_{i-1/2}^{\text{sc}}$ and $D_{i+1/2}^{\text{sc}}$ are dumping functions defined as

$$D_{i-1/2}^{\text{sc}} = \sum_{j=1-n}^{n} c_j U_{i+j} \tag{2.41}$$

$$D_{i+1/2}^{\text{sc}} = \sum_{j=1-n}^{n} c_j U_{i+j-1} \tag{2.42}$$

The coefficients c_j of the shock filter are derived from the coefficients d_j of a corresponding non-conservative centered filter. To optimize the shock filter, a specific 4-point conservative filter is designed in the Fourier space by Bogey *et al.* [11] in order to have dissipation features similar to the standard second-order filter while reducing errors.
This selective application of artificial dissipation, guided by the shock detector, allows for a more accurate and stable simulation of propagation in the presence of shock waves.

2.6 Perfectly Matched Layer

This section delves into the methodology of Perfectly Matched Layers (PML) as absorbing boundary conditions, particularly within the context of Euler equations. This method serves as a crucial tool for simulating wave propagation in unbounded domains by effectively eliminating reflections at artificial boundaries. This is achieved through the construction of modified governing equations within a designated PML zone that can absorb outgoing waves.
The PML technique was initially introduced in 1994 for computational electromagnetics by Berenger [14]. A key advantage of the PML method lies in its theoretical ability to create

reflectionless absorption for multidimensional waves, irrespective of their angle or frequency. Consequently, PML zones can often be designed to be thinner compared to other types of buffer or sponge zones. The original PML formulation involved splitting physical variables, which was later identified as dynamically stable but weakly well-posed. Subsequent research from Hu [8] demonstrated the equivalence of the PML technique to a complex change of variables in the frequency domain. This understanding allowed for the derivation of PML equations using unsplit physical variables.

The extension of PML to computational fluid dynamics and aeroacoustics began with the linearized Euler equations. It was shown that the initial PML equations perfectly matched the linearized Euler equations, theoretically absorbing acoustic, vorticity, and entropy waves without reflection. However, numerical instabilities were observed, associated with the differing signs of the phase and group velocities of acoustic waves, particularly in the presence of a mean flow. A vital condition for the PML technique to function correctly was identified: all physical waves must exhibit consistent phase and group velocities [15, 16].

To ensure this condition, a space-time transformation was introduced prior to applying the PML technique. This transformation ensures that, in the transformed coordinates, all waves have consistent phase and group velocities, leading to dynamically stable and computationally effective absorbing boundary conditions. This involved modifying the governing equations to ensure the phase and group velocities of linear waves are consistent, which is necessary for effective wave absorption within the PML. The implementation of this space-time transformation is a crucial step in ensuring the stability and effectiveness of PML for the Euler equations.

The steps for deriving the PML equations are now illustrated. A two-dimensional case with uniform flow v_0 along the vertical z-axis is considered. The two-dimensional non-linear Euler equations are written for perturbations in the conservative form:

$$\frac{\partial \boldsymbol{U'}}{\partial t} + \frac{\partial \left(\boldsymbol{E} - \bar{\boldsymbol{E}}\right)}{\partial x} + \frac{\partial \left(\boldsymbol{F} - \bar{\boldsymbol{F}}\right)}{\partial z} = 0 \tag{2.43}$$

The assumption is made that the mean field is time-independent and thus meets the stationary Euler equations:

$$\frac{\partial \bar{\boldsymbol{E}}}{\partial x} + \frac{\partial \bar{\boldsymbol{F}}}{\partial z} = 0 \tag{2.44}$$

A change of variables is now made:

$$\hat{t} = t + \tilde{\beta} z, \quad \hat{x} = x, \quad \hat{z} = z \tag{2.45}$$

where $\tilde{\beta} = \beta / c_0$ and $\beta = M/(1 - M^2)$, with M the Mach number, in the case where the mean density is uniform and constant all over the computational domain. Otherwise, the choice of β needs further analysis starting from the dispersion relation [8].

Changing space-time coordinates involves calculating differentials in the new reference system.

The differentials are thus computed from Eq. (2.45):

$$\frac{\partial}{\partial x} = \frac{\partial \hat{x}}{\partial x}\frac{\partial}{\partial \hat{x}} + \frac{\partial \hat{z}}{\partial x}\frac{\partial}{\partial \hat{z}} + \frac{\partial \hat{t}}{\partial x}\frac{\partial}{\partial \hat{t}} = \frac{\partial}{\partial \hat{x}} \tag{2.46}$$

$$\frac{\partial}{\partial z} = \frac{\partial \hat{x}}{\partial z}\frac{\partial}{\partial \hat{x}} + \frac{\partial \hat{z}}{\partial z}\frac{\partial}{\partial \hat{z}} + \frac{\partial \hat{t}}{\partial z}\frac{\partial}{\partial \hat{t}} = \frac{\partial}{\partial \hat{z}} + \tilde{\beta}\frac{\partial}{\partial \hat{t}} \tag{2.47}$$

$$\frac{\partial}{\partial t} = \frac{\partial \hat{x}}{\partial t}\frac{\partial}{\partial \hat{x}} + \frac{\partial \hat{z}}{\partial t}\frac{\partial}{\partial \hat{z}} + \frac{\partial \hat{t}}{\partial t}\frac{\partial}{\partial \hat{t}} = \frac{\partial}{\partial \hat{t}} \tag{2.48}$$

Equation (2.43) is rewritten in the new coordinate system by using Eqs. (2.46-2.48):

$$\frac{\partial \boldsymbol{U'}}{\partial \hat{t}} + \tilde{\beta}\frac{\partial\left(\boldsymbol{F}-\bar{\boldsymbol{F}}\right)}{\partial \hat{t}} + \frac{\partial\left(\boldsymbol{E}-\bar{\boldsymbol{E}}\right)}{\partial \hat{x}} + \frac{\left(\boldsymbol{F}-\bar{\boldsymbol{F}}\right)}{\partial \hat{z}} = 0 \tag{2.49}$$

A transformation in the frequency domain is applied to spatial coordinates x and z:

$$\frac{\partial}{\partial \hat{x}} \rightarrow \frac{1}{1+\frac{\sigma_x}{\mathrm{i}\omega}}\frac{\partial}{\partial \hat{x}} = \frac{\mathrm{i}\omega}{\mathrm{i}\omega+\sigma_x}\frac{\partial}{\partial \hat{x}} = \left(1-\frac{\sigma_x}{\mathrm{i}\omega+\sigma_x}\right)\frac{\partial}{\partial \hat{x}} \tag{2.50}$$

$$\frac{\partial}{\partial \hat{z}} \rightarrow \frac{1}{1+\frac{\sigma_z}{\mathrm{i}\omega}}\frac{\partial}{\partial \hat{z}} = \frac{\mathrm{i}\omega}{\mathrm{i}\omega+\sigma_z}\frac{\partial}{\partial \hat{z}} = \left(1-\frac{\sigma_z}{\mathrm{i}\omega+\sigma_z}\right)\frac{\partial}{\partial \hat{z}} \tag{2.51}$$

with

$$\sigma_x = \frac{1}{\Delta t}\left[\frac{x-x_0}{L}\right]^3 \tag{2.52}$$

$$\sigma_z = \frac{1}{\Delta t}\left[\frac{z-z_0}{L}\right]^3 \tag{2.53}$$

where x_0 and z_0 are the starting points of the zone where PML is applied on the x- and z-axis, respectively, L is the width of the PML zone and Δt is the time step.
Equation (2.49) is rewritten after applying the transformations in Eqs. (2.50-2.51):

$$\begin{aligned}&-\mathrm{i}\omega\frac{\partial \boldsymbol{U'}}{\partial \hat{t}} - \mathrm{i}\omega\tilde{\beta}\frac{\partial\left(\boldsymbol{F}-\bar{\boldsymbol{F}}\right)}{\partial \hat{t}} + \frac{\partial\left(\boldsymbol{E}-\bar{\boldsymbol{E}}\right)}{\partial \hat{x}} + \frac{\left(\boldsymbol{F}-\bar{\boldsymbol{F}}\right)}{\partial \hat{z}}\\ &-\frac{\sigma_x}{\mathrm{i}\omega+\sigma_x}\frac{\partial\left(\boldsymbol{E}-\bar{\boldsymbol{E}}\right)}{\partial \hat{x}} - \frac{\sigma_z}{\mathrm{i}\omega+\sigma_z}\frac{\left(\boldsymbol{F}-\bar{\boldsymbol{F}}\right)}{\partial \hat{z}} = 0\end{aligned} \tag{2.54}$$

Auxiliary variables $\boldsymbol{\phi_x}$ and $\boldsymbol{\phi_z}$ are defined as follows:

$$\boldsymbol{\phi_x} = \frac{1}{\mathrm{i}\omega+\sigma_x}\frac{\partial\left(\boldsymbol{E}-\bar{\boldsymbol{E}}\right)}{\partial \hat{x}} \Rightarrow \frac{\partial \boldsymbol{\phi_x}}{\partial \hat{t}} + \sigma_x\boldsymbol{\phi_x} - \frac{\partial\left(\boldsymbol{E}-\bar{\boldsymbol{E}}\right)}{\partial \hat{x}} = 0 \tag{2.55}$$

$$\boldsymbol{\phi_z} = \frac{1}{\mathrm{i}\omega+\sigma_z}\frac{\partial\left(\boldsymbol{F}-\bar{\boldsymbol{F}}\right)}{\partial \hat{z}} \Rightarrow \frac{\partial \boldsymbol{\phi_z}}{\partial \hat{t}} + \sigma_z\boldsymbol{\phi_z} - \frac{\partial\left(\boldsymbol{F}-\bar{\boldsymbol{F}}\right)}{\partial \hat{z}} = 0 \tag{2.56}$$

The definitions in Eqs. (2.55-2.56) are applied in Eq. (2.54). This yields:

$$\frac{\partial \boldsymbol{U'}}{\partial \hat{t}} + \tilde{\beta}\frac{\partial\left(\boldsymbol{F}-\bar{\boldsymbol{F}}\right)}{\partial \hat{t}} + \frac{\partial\left(\boldsymbol{E}-\bar{\boldsymbol{E}}\right)}{\partial \hat{x}} + \frac{\left(\boldsymbol{F}-\bar{\boldsymbol{F}}\right)}{\partial \hat{z}} - \sigma_x\boldsymbol{\phi_x} - \sigma_z\boldsymbol{\phi_z} = 0 \tag{2.57}$$

Equations (2.55-2.57) are now rewritten in the original space-time coordinate system by using Eqs. (2.46-2.48). This gives:

$$\frac{\partial \boldsymbol{U'}}{\partial t} + \frac{\partial \left(\boldsymbol{E} - \bar{\boldsymbol{E}}\right)}{\partial x} + \frac{\left(\boldsymbol{F} - \bar{\boldsymbol{F}}\right)}{\partial z} - \sigma_x \boldsymbol{\phi_x} - \sigma_z \boldsymbol{\phi_z} = 0 \tag{2.58}$$

$$\frac{\partial \boldsymbol{\phi_x}}{\partial t} + \sigma_x \boldsymbol{\phi_x} - \frac{\partial \left(\boldsymbol{E} - \bar{\boldsymbol{E}}\right)}{\partial x} = 0 \tag{2.59}$$

$$\frac{\partial \boldsymbol{\phi_z}}{\partial t} + \tilde{\beta} \frac{\partial \left(\boldsymbol{F} - \bar{\boldsymbol{F}}\right)}{\partial t} + \sigma_z \boldsymbol{\phi_z} - \frac{\partial \left(\boldsymbol{F} - \bar{\boldsymbol{F}}\right)}{\partial z} = 0 \tag{2.60}$$

A new auxiliary variable $\boldsymbol{\xi}$ is introduced, which is defined as follows:

$$\boldsymbol{\xi} = \boldsymbol{\phi_z} + \tilde{\beta}\left(\boldsymbol{F} - \bar{\boldsymbol{F}}\right) \tag{2.61}$$

The form of PML equations for 2D Euler equations with a uniform mean flow along the z-axis is finally found:

$$\frac{\partial \boldsymbol{U'}}{\partial t} + \frac{\partial \boldsymbol{E}}{\partial x} + \frac{\partial \boldsymbol{F}}{\partial z} - \sigma_x \boldsymbol{\phi_x} - \sigma_z \left[\boldsymbol{\xi} - \tilde{\beta}\left(\boldsymbol{F} - \bar{\boldsymbol{F}}\right)\right] = 0 \tag{2.62}$$

$$\frac{\partial \boldsymbol{\phi_x}}{\partial t} + \sigma_x \boldsymbol{\phi_x} - \frac{\partial \boldsymbol{E}}{\partial x} = 0 \tag{2.63}$$

$$\frac{\partial \boldsymbol{\xi}}{\partial t} + \sigma_z \boldsymbol{\phi_z} - \frac{\partial \boldsymbol{F}}{\partial z} = 0 \tag{2.64}$$

The mean fluxes $\bar{\boldsymbol{E}}$ and $\bar{\boldsymbol{F}}$ have been removed from the spatial derivatives because the assumption was made that the mean flow respects the stationary Euler equations in Eq. (2.44). The derivation can be repeated in the case of a uniform flow in the x-direction, obtaining a similar form.
The derivation for the three-dimensional case follows the same steps, with the addition of course of a third dimension, finding a form similar to that presented above. The system of equations to solve in this case with a uniform flow along the x-axis is given by:

$$\frac{\partial \boldsymbol{U'}}{\partial t} + \frac{\partial \boldsymbol{E}}{\partial x} + \frac{\partial \boldsymbol{F}}{\partial y} + \frac{\partial \boldsymbol{G}}{\partial z} - \sigma_y \boldsymbol{\phi_y} - \sigma_z \boldsymbol{\phi_z} - \sigma_x \left[\boldsymbol{\xi} - \tilde{\beta}\left(\boldsymbol{E} - \bar{\boldsymbol{E}}\right)\right] = 0 \tag{2.65}$$

$$\frac{\partial \boldsymbol{\phi_y}}{\partial t} + \sigma_y \boldsymbol{\phi_y} - \frac{\partial \boldsymbol{F}}{\partial y} = 0 \tag{2.66}$$

$$\frac{\partial \boldsymbol{\phi_z}}{\partial t} + \sigma_z \boldsymbol{\phi_z} - \frac{\partial \boldsymbol{G}}{\partial z} = 0 \tag{2.67}$$

$$\frac{\partial \boldsymbol{\xi}}{\partial t} + \sigma_x \boldsymbol{\phi_x} - \frac{\partial \boldsymbol{E}}{\partial x} = 0 \tag{2.68}$$

2.7 Conclusion

The numerical methodology adopted in this thesis provides a robust, accurate, and computationally efficient framework for high-fidelity computational aeroacoustics simulations. The approach is based on the solution of the full three-dimensional non-linear Euler equations in conservative form, which is essential for accurately modeling acoustic wave propagation, capturing

non-linear effects, and resolving shock-waves. Spatial discretization is performed using optimized central finite-difference schemes, such as the eleven-point stencil FDo11p, which are specifically designed to minimize numerical dispersion and dissipation. This formulation enables accurate resolution of short wavelength acoustic waves with as few as four points per wavelength, thereby enhancing numerical efficiency. Time integration is carried out using a low-storage, explicit six-stage optimized Runge–Kutta scheme (RKo6s), selected for its extended stability limits and reduced temporal dispersion and dissipation over the relevant frequency range.

The stability and consistency of the numerical framework are ensured through the integration of tailored dissipation and boundary treatment strategies. An optimized selective filter based on an eleven-point stencil is applied globally to suppress grid-to-grid oscillations while introducing minimal artificial dissipation and preserving long wavelength acoustic waves. In regions containing discontinuities, a dedicated shock-capturing strategy is employed, relying on a sensor derived from Weighted Essentially Non-Oscillatory smoothness indicators to selectively activate artificial dissipation in the vicinity of shock fronts only. This approach ensures numerical robustness without compromising acoustic accuracy elsewhere in the domain. Absorbing boundary conditions are implemented using Perfectly Matched Layers, which incorporate an appropriate space-time transformation to ensure the same sign between phase and group velocities, thereby effectively eliminating spurious wave reflections at the computational boundaries. This carefully designed numerical framework, emphasizing low dispersion and low dissipation while incorporating targeted robustness mechanisms, forms the foundation for all simulations presented in the subsequent chapters.

For clarity, Table 2.1 summarizes the numerical methodology adopted throughout this work, including spatial discretization, time integration scheme, filtering strategy, shock treatment, and boundary conditions.

Numerical component	**Method**	**Type**	**Key Parameters**
Spatial discretization	Finite difference scheme	FDo11p	$\Delta x = \text{const}$
Time integration	Runge-Kutta scheme	RKo6s	CFL $= 0.5$
Selective filter	Centered scheme	SFo11p	$\sigma_{\text{sf}} = 0.8$
Shock-capturing filter	Shock sensor-based filter	WENO	$r_{\text{th}} = 0.8$, $\sigma^{\text{sc}}_{\text{max}} = 0.5$
Boundary conditions	Perfectly Matched Layer	Auxiliary variables	Thickness: $L = 30\Delta x$ Profile: $\sigma_i = \frac{1}{\Delta t}\left[\frac{x_i - x_0}{L}\right]^3$

Table 2.1: Summary of the numerical methodology adopted in the present work.

3 A new method to prescribe incoming waves

Prescribing incoming acoustic pressure and velocity perturbations without generating spurious waves is always a tricky subject in computational aeroacoustics. This is all the more true when the time-dependent signal to be injected is extracted from a separate numerical simulation in fluid mechanics. This chapter presents an original volumetric source term method to inject unidirectional acoustic waves from an arbitrary shaped control surface within the computational domain. A review of existing methods in the scientific literature is first provided, followed by the methodological framework and the derivation of the source terms. Finally, results from three representative academic configurations are presented to validate the proposed method.

3.1 State of the art

This section reviews existing approaches for computing acoustic quantities from separate Computational Fluid Dynamics (CFD) simulations, either through integral formulations based on acoustic analogies or via Computational Aeroacoustics (CAA) simulations. Among the most widely used coupling techniques between CFD and CAA are the Ffowcs Williams–Hawkings (FWH) and the Kirchhoff integral formulations, and the characteristic boundary method. Another approach involves introducing the desired acoustic quantities through source terms directly in the governing equations. Each of these methods is presented below, with a focus on their advantages, capabilities, and limitations.

3.1.1 Acoustic Analogy Formulations

The prediction of noise generated by complex moving sources, particularly rotating blades, relies heavily on rigorous theoretical prediction methodologies. Among the most foundational integral methods in aeroacoustics are those derived from the Lighthill acoustic analogy [17, 18], notably

the Ffowcs Williams-Hawkings (FWH) [19] equation, and the Kirchhoff formulation for moving surfaces [20]. While both have proven utility in rotor noise prediction, their theoretical bases and practical implementation constraints reveal crucial differences that define the current state of the art. A comparison of the two methods is provided by Brentner and Farassat [21].

The Ffowcs Williams & Hawkings equation

The FWH intgral method is one of the most widely adopted approach for CFD/CAA coupling. By enclosing the acoustic source within a porous control surface, equivalent source terms are derived to solve the wave equation in the farfield. The Ffowcs Williams-Hawkings equation represents the most general form of the Lighthill acoustic analogy. It is derived through an exact rearrangement of the Navier-Stokes equations into the form of an inhomogeneous wave equation. Consequently, the FWH equation is analytically superior for aeroacoustics because its validity is based upon the conservation laws rather than the wave equation, meaning it remains valid even when the integration surface is located within the non-linear flow region.
To derive the FWH equation, consider a surface defined by $f(\boldsymbol{x}, t) = 0$, moving at the velocity $v(\boldsymbol{x}, t)$, with a stationary fluid occupying the region outside the surface. The surface is specified such that $\nabla f = \boldsymbol{n}$, where $\boldsymbol{n}$ denotes the outward-pointing unit normal vector. The fluid contained within the surface ($f < 0$) may be replaced by a quiescent fluid together with a surface distribution of sources that preserves the conservative character of the flow field. Under this formulation, the generalized conservation equations for mass and momentum can be expressed as follows:

$$\frac{\partial}{\partial t}\left[(\rho - \rho_0)\, H(f)\right] + \frac{\partial}{\partial x_i}\left[\rho u_i H(f)\right] = Q\delta(f) \tag{3.1}$$

$$\frac{\partial}{\partial t}\left[\rho u_i H(f)\right] + \frac{\partial}{\partial x_j}\left[\left(\rho u_i u_j + P_{ij}\right) H(f)\right] = L_i\delta(f) \tag{3.2}$$

where

$$Q = \rho_0 U_i n_i \tag{3.3}$$

$$U_i = \left(1 - \frac{\rho}{\rho_0}\right) v_i + \frac{\rho u_i}{\rho_0} \tag{3.4}$$

$$L_i = P_{ij} n_j + \rho u_i \left(u_n - v_n\right) \tag{3.5}$$

$$P_{ij} = (p - p_0)\, \delta_{ij} - \tau_{ij} \tag{3.6}$$

where $Q\delta(f)$ and $L_i\delta(f)$ denote the surface source distributions of mass and momentum, respectively. Here, the subscript $(\cdot)_0$ denotes freestream quantities, whereas the subscript i indicates the i-th direction of the reference frame. The tensor P_{ij} represents the compressive stress, δ denotes the Dirac delta distribution, and δ_{ij} is the Kronecker delta. The following

relations

$$\frac{\partial H(f)}{\partial t} = \delta(f)\frac{\partial f}{\partial t} = -\delta(f)v_n \tag{3.7}$$

$$\frac{\partial H(f)}{\partial x_i} = \delta(f)\frac{\partial f}{\partial x_i} = \delta(f)n_i \tag{3.8}$$

have been used in Eqs. (3.1) and (3.2).
Taking the time derivative of Eq. (3.1) and subtracting the divergence of Eq. (3.2), the FWH equation can be expressed as follows:

$$\Box^2 p'(\boldsymbol{x}, t) = \frac{\partial^2}{\partial x_i \partial x_j}\left[T_{ij}H(f)\right] - \frac{\partial}{\partial x_i}\left[L_i\delta(f)\right] + \frac{\partial}{\partial t}\left[Q\delta(f)\right] \tag{3.9}$$

where $\Box^2(\cdot)$ is the d'Alembert operator and

$$T_{ij} = \rho u_i u_j + \left(p' - c^2\rho'\right)\delta_{ij} - \tau_{ij} \tag{3.10}$$

is the Lighthill's stress tensor.
Equation (3.9) is the FWH equation, which inherently includes three distinct source terms on the right-hand side:

- The term $\frac{\partial}{\partial t}\left[Q\delta(f)\right]$ is the thickness noise, determined entirely by the kinematics and geometry of the body.
- The term $-\frac{\partial}{\partial x_i}\left[L_i\delta(f)\right]$ is the loading noise, generated by the force exerted on the fluid by the body.
- The term $\frac{\partial^2}{\partial x_i \partial x_j}\left[T_{ij}H(f)\right]$ is a volume quadrupole source, which accounts for non-linear flow effects, including shock generation, variations in sound speed, turbulence and vorticity.

This decomposition of sources offers a significant advantage, providing physical insight into the noise generation mechanisms that aids in the design of quieter rotors.

The Kirchhoff equation

The Kirchhoff formulation for moving bodies is also an inhomogeneous wave equation, but its development is rooted in the domain of wave propagation. The acoustic field in the region $f < 0$ is replaced by an elementary quiescent fluid $p' = 0$. A distribution of sources on the surface $f = 0$ is then required to maintain the fictitious discontinuities introduced in the original field.

Considering the generalized derivatives for the wave equation, one can write:

$$\frac{1}{c}\frac{\partial}{\partial t}\left(p'H(f)\right) = \frac{1}{c}\frac{\partial p'}{\partial t}H(f) - M_n p'\delta(f) \tag{3.11}$$

$$\frac{1}{c}\left[\frac{1}{c}\frac{\partial}{\partial t}\left(p'H(f)\right)\right] = \frac{1}{c^2}\frac{\partial^2 p'}{\partial t^2}H(f) - \frac{1}{c}\frac{\partial p'}{\partial t}M_n\delta(f) - \frac{1}{c}\frac{\partial}{\partial t}\left(p'M_n\delta(f)\right) \tag{3.12}$$

$$\nabla\left(p'H(f)\right) = \nabla p'H(f) + p'\boldsymbol{n}\delta(f) \tag{3.13}$$

$$\nabla\cdot\nabla\left(p'H(f)\right) = \nabla^2 p'H(f) + \nabla p'\cdot\boldsymbol{n}\delta(f) + \nabla\cdot\left(p'\boldsymbol{n}\delta(f)\right) \tag{3.14}$$

where $M_n = v_n/c$ is the local normal Mach number of the surface $f = 0$.
The Kirchhoff equation is obtained by subtracting Eq. (3.14) from Eq. (3.12):

$$\Box^2\left(p'H(f)\right) = -\left(\frac{\partial p'}{\partial n} + \frac{M_n}{c}\frac{\partial p'}{\partial t}\right)\delta(f) - \frac{1}{c}\frac{\partial}{\partial t}\left[M_n p'\delta(f)\right] - \frac{\partial}{\partial x_i}\left[p'n_i\delta(f)\right] \tag{3.15}$$

The integral solution utilizes source terms distributed only on a specified closed surface. A key difference is that the Kirchhoff governing equation is only valid in the region of the fluid where the wave equation is the appropriate governing equation; that is, the region must be linear. Furthermore, the Kirchhoff source terms are not easily related to physical mechanisms such as thickness, loading, or non-linear effects, thereby providing less guidance for acoustic design efforts.

A comparison between the FWH and the Kirchhoff equations

Analytically, the FWH and the Kirchhoff equations are equivalent if the integration surface for both methods is positioned in the linear flow region. However, the FWH formulation, unlike the Kirchhoff formulation, provides the ability to include non-linear flow effects in the surface integration.
The main disadvantage of the traditional FWH method is that accurate noise prediction for bodies moving at transonic speeds requires the inclusion of the quadrupole source term. Because the quadrupole is a volume source, its calculation necessitates a computationally expensive volume integration over the entire source region. While approximations can reduce this computational effort, the volume integration cannot be completely avoided.
The Kirchhoff approach avoids this computational pitfall by relying solely on surface source terms, making it attractive for predicting transonic rotor noise. However, this advantage introduces a critical constraint: the Kirchhoff surface must be chosen to reside in the linear flow region. This requirement presents a significant knowledge gap, as the location of the linear region is problem-dependent and often not well defined. To maintain accuracy, the Kirchhoff surface should ideally be placed far from the source region, yet CFD solutions tend to be less accurate and less resolved away from the body. If the integration surface is not positioned correctly and intrudes into the non-linear region, the predicted acoustic pressure may become substantially erroneous, and the nature or magnitude of the resulting error can be difficult to recognize or estimate.
A significant advancement is the alternative implementation of the FWH equation, which utilizes

a permeable integration surface away from the physical body. This formulation retains the original FWH governing equation but is adapted to use input variables commonly available from modern CFD codes. This modified approach demonstrates the core advantage of the FWH formulation: the relaxation of integration surface placement restrictions.
The choice between the FWH and Kirchhoff integral methods hinges on balancing computational efficiency against analytical rigor and physical interpretability. If the flow field is sufficiently linear and the surface placement can be assuredly outside the non-linear source region, the Kirchhoff method offers computational efficiency by eliminating volume integration. However, the FWH equation, drawing its foundation from the conservation laws of fluid dynamics, provides superior analytical validity and robustness, particularly when integrating in the non-linear region or when physical understanding of the generated noise components is paramount. The modern approach of using a modified FWH formulation on a permeable surface seeks to harness the computational benefit of surface integration while retaining the inherent accuracy and flexibility of the Lighthill acoustic analogy.
However, while effective for linear propagation in a homogeneous medium, this method does not account for non-linear propagation effects [22] or the presence of physical obstacles within the extrapolation domain, which limits its applicability to the present work and therefore is not considered further.

3.1.2 Direct Use of Acoustic Data on Control Surfaces

An alternative strategy relies on the direct use of acoustic data on a control surface. Perturbations can be imposed explicitly, as done by de Cacqueray *et al.* [23] to characterize non-linear propagation effects of supersonic jet noise and Emmanuelli *et al.* [24] to prescribe the incoming non-linear acoustic wave at the computational domain inlet. A formal two-way coupling between two solvers can also be used for more complex computational domains, as investigated by Langelais *et al.* [25] for noise on a launch pad.

3.1.3 Method of Characteristics

The method of characteristics, first developed by Thompson [26, 27] and generalized by Poinsot and Lele [28] with the Navier-Stokes characteristic boundary conditions method, provides an alternative approach for enforcing boundary conditions.
The method was further improved by Daviller *et al.* [29] to prevent divergence of the mean inlet velocity from the target value, enabling accurate introduction of both turbulent and acoustic velocity components. The method of characteristics was used by Thisse *et al.* [30] and Daroukh *et al.* [31] for instance as a computational fluids dynamics - Euler coupling strategy to introduce acoustic waves.
The method of characteristics can be applied to both the Euler and Navier–Stokes equations and is suitable for use at the boundaries of the computational domain to either introduce

prescribed quantities or allow wave transmission without reflection. Near the domain boundaries, spatial derivatives must be computed using one-sided finite differences schemes, which can decrease numerical accuracy. The technique involves rewriting the governing equations through characteristic analysis to modify the hyperbolic terms associated with waves propagating in the x-direction, as illustrated in Fig. 3.1.

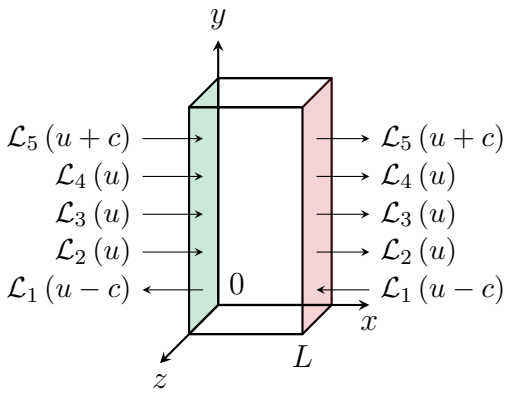

Figure 3.1: Characteristics waves entering the computational domain at the inlet plane $x = 0$ and leaving at the outlet plane $x = L$.

The reformulated equations include terms involving the normal and tangential spatial derivatives of the considered inlet (or outlet) plane, which depend on the amplitudes $\mathcal{L}_i$ of the characteristic waves traveling at specific velocities λ_i. These are defined as:

$$\lambda_1 = u - c \tag{3.16}$$

$$\lambda_2 = \lambda_3 = \lambda_4 = u \tag{3.17}$$

$$\lambda_5 = u + c \tag{3.18}$$

where λ_1 and λ_5 represents the propagation velocities of acoustic waves traveling in the negative and positive x-directions, respectively, λ_2 denotes the velocity of entropy waves, λ_3 and λ_4 corresponds to the advection velocities o the v and w components in the x-direction.
To introduce incoming waves into the computational domain, one must solve a corresponding set of equations known as the Local One-Dimensional Inviscid (LODI) system. These equations are evaluated at each boundary point where an incoming wave is prescribed. As the name implies, the formulation is inherently one-dimensional and does not directly represent physical conditions. Instead, it defines compatibility relationships between the physical boundary conditions to be imposed and the amplitudes of the characteristic waves. These relationships can be expressed as

follows:

$$\frac{\partial \rho}{\partial t} + \frac{1}{c^2}\left[\mathcal{L}_2 + \frac{1}{2}\left(\mathcal{L}_5 + \mathcal{L}_1\right)\right] = 0 \tag{3.19}$$

$$\frac{\partial p}{\partial t} + \frac{1}{2}\left(\mathcal{L}_5 + \mathcal{L}_1\right) = 0 \tag{3.20}$$

$$\frac{\partial u}{\partial t} + \frac{1}{2\rho c}\left(\mathcal{L}_5 - \mathcal{L}_1\right) = 0 \tag{3.21}$$

$$\frac{\partial v}{\partial t} + \mathcal{L}_3 = 0 \tag{3.22}$$

$$\frac{\partial w}{\partial t} + \mathcal{L}_4 = 0 \tag{3.23}$$

When the velocity λ_i is directed outward from the computational domain, the corresponding characteristic wave amplitudes $\mathcal{L}_i$ can be directly computed within the domain using one-sided finite differences. In contrast, the incoming characteristics $\mathcal{L}_i$ depend on the boundary conditions imposed. For the introduction of acoustic waves in a subsonic medium, non-reflecting boundary conditions are typically applied as follows:

$$\mathcal{L}_1 = \lambda_1 \left(\frac{\partial p}{\partial x} - \rho_0 c_0 \frac{\partial u}{\partial x}\right) \tag{3.24}$$

$$\mathcal{L}_2 = \mathcal{L}_3 = \mathcal{L}_4 = 0 \tag{3.25}$$

$$\mathcal{L}_5 = \lambda_5 \left(\frac{\partial \tilde{p}}{\partial x} + \rho_0 c_0 \frac{\partial \tilde{u}}{\partial x}\right) \tag{3.26}$$

where the quantities denoted by $\tilde{(\cdot)}$ represent the values imposed at the boundary during each iteration for the waves entering the computational domain.

A mesh conforming to the surface geometry is in general used. Moreover, the method of characteristics is inherently one-dimensional and performs optimally only when the acoustic wave vector is normal to the injection surface [32, 33]. Furthermore, this method can only be applied at the domain boundaries, preventing the introduction of prescribed quantities within the interior of the domain. This limitation poses a challenge for injecting waves from a control surface unless the mesh elements conform to the geometry of that surface. Depending on the specific application, this constraint may be particularly restrictive when employing a uniform Cartesian mesh.

3.1.4 Volumetric Source Terms

A different approach based on volumetric source terms has been initially developed by Maeda and Colonius [34]. The authors proposed a framework to generate one-way acoustic waves using volumetric source terms in the governing equations. This section presents the method developed by the authors mentioned above and summarizes the principal results.

The main advantage of this method relies in introducing a prescribed acoustic field into the computational domain without the necessity to use non-centered finite differences schemes at the boundaries. The source term approach offers a specialized methodology to address this challenge

by generating unidirectional acoustic waves directly within the fluid volume using the full Euler or Navier–Stokes equations. This approach is specifically designed to suppress waves propagating backward from the source surface, thereby mitigating reflections from imperfect non-reflecting computational boundaries.

The core strategy lies in defining a volumetric source term that models the singular distribution of acoustic energy originating from an arbitrary, smooth two-dimensional surface. The model is fundamentally rooted in the compressible, inhomogeneous Euler equations:

$$\frac{\partial \rho}{\partial t} + \nabla \cdot (\rho \boldsymbol{u}) = S_1 \tag{3.27}$$

$$\frac{\partial (\rho \boldsymbol{u})}{\partial t} + \nabla \cdot (\rho \boldsymbol{u}\boldsymbol{u} + p\mathcal{I}) = \boldsymbol{S_2} \tag{3.28}$$

$$\frac{\partial \rho e_t}{\partial t} + \nabla \cdot \left[(\rho e_t + p)\, \boldsymbol{u} \right] = S_3 \tag{3.29}$$

where S_1, $\boldsymbol{S_2}$ and S_3 are the scalar mass, vector momentum and scalar energy sources, respectively, and $\mathcal{I}$ is the identity matrix.

By reformulating the conservation equations in terms of linear perturbations about a quiescent state, the wave equation is obtained:

$$\frac{1}{c_0^2}\frac{\partial^2 p'}{\partial t^2} - \nabla^2 p' = \frac{\partial S_1}{\partial t} - \nabla \cdot \boldsymbol{S_2} \tag{3.30}$$

The right-hand side in Eq. (3.30) includes the contributions of the mass source term S_1 and the momentum source terms $\boldsymbol{S_2}$.

The energy source S_3 is configured to prevent entropy generation at the surface. The derivation relies on the Green's function solution to the linearized wave equation to determine the necessary combination of sources required for one-way propagation:

$$p(\boldsymbol{x}, t) = \int_0^t \mathrm{d}\tau \int_{-\infty}^{\infty} \mathrm{d}\boldsymbol{x'} G\left(t, \tau, \boldsymbol{x}, \boldsymbol{x'}\right) \left(\frac{\partial S_1}{\partial t} - \nabla \cdot \boldsymbol{S_2} \right) \tag{3.31}$$

The unidirectional effect is achieved by constructing the volumetric source as a linear combination of monopole and dipole sources, a concept borrowed from active noise reduction (anti-sound) [35–37] where superposition is utilized to actively cancel waves propagating in an unwanted direction.

For a one-dimensional plane wave, one can define the mass and momentum source as:

$$S_1 = f(t)\delta(x - x_s) \tag{3.32}$$

$$S_2 = g(t)\delta(x - x_s) \tag{3.33}$$

where $f(t)$ and $g(t)$ are two arbitrary functions that satisfy the causality condition $f(t) = g(t) = 0$ for $t < 0$, x_s is the source position and δ is the Dirac support. In simulations, one chooses a smeared Dirac delta function to regularize the singular distribution onto the computational cells

neighboring the surface. A common form used is the Gaussian function. The support width of the smeared delta function is typically chosen to be on the order of the characteristic grid size. By using Eq. (3.31), the convolution is carried out and gives the associated pressure signal:

$$p(x,t) = \frac{1}{2}\left[cf\left(t - \frac{|x_s - x|}{c}\right) + g\left(t - \frac{|x_s - x|}{c}\right)\operatorname{sgn}(x - x_s)\right] \tag{3.34}$$

where c is the speed of sound.

The mass source S_1 acts as a monopole, generating outgoing waves of the same sign in both positive and negative x-directions, while the momentum source S_2 acts as a dipole, generating waves of opposite sign, as shown in Fig. 3.2.

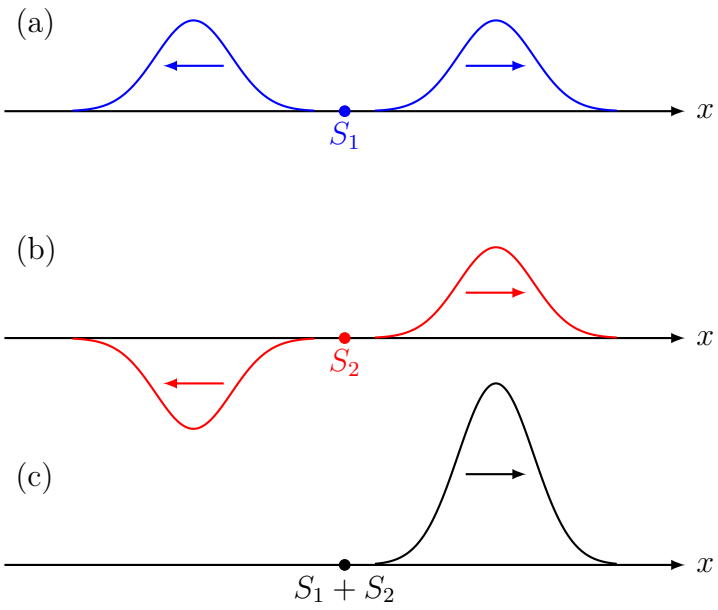

Figure 3.2: Diagram illustrating (a) a monopole generated by the mass source S_1, (b) a dipole generated by the momentum source S_2, and (c) the resulting wave obtained from the superposition of both sources.

Unidirectionality is achieved when the sources are balanced, causing cancellation in the negative x-direction. By choosing $f(t) = g(t)/c$, Eq. (3.34) becomes:

$$p(x,t) = H(x - x_s)\, g\left(t - \frac{|x - x_s|}{c}\right) \tag{3.35}$$

This results in a plane wave propagating solely in the positive x-direction, as the waves traveling in the negative x-direction cancel each other out.

For curved surfaces, such as a spherical shell, the momentum source S_2 introduces an additional monopole component originating from the geometry. Achieving a one-way solution propagating outward requires a more complex definition for $f(t)$ that includes a geometrical component related to the anti-derivative of the source function, $G_g(t)$.

The source approach allows for modeling arbitrary, smooth surfaces by combining the planar and spherical one-way sources as fundamental building blocks. However, it is noted that the model for a one-way cylindrical wave is an approximation, valid only when the characteristic wavelength is much smaller than the radius of the source.

A critical finding regarding the numerical method is that the necessary regularization of the singular source term introduces a limitation on convergence. While the underlying finite-volume scheme may be higher-order for smooth solutions, the regularization of the singular source on the scale of the grid spacing forces the overall numerical solution to be first-order accurate.

The proposed method was rigorously verified against analytical solutions and validated against experimental data across both linear and non-linear acoustic regimes.

As discussed by Maeda and Colonius [34], their simulations successfully verified the generation of a one-way plane Gaussian pulse in air and a one-way spherical sinusoidal pulse in water. These verification cases confirmed the cancellation mechanism, showing how the monopole component from the mass source and the opposite-signed dipole component from the momentum source cancelled the backward-propagating wave. Furthermore, validation of the spherical pulse demonstrated that inclusion of the geometrical component $G_g(t)$ was essential for accurate agreement with the analytical solution.

The source term approach presents a powerful alternative to traditional immersed boundary methods for acoustic modeling [38–40]. Although the derived source terms are successfully applied to the full non-linear Euler equations, the underlying mathematical formulation for the one-way behavior relies entirely on linear perturbation theory. The accuracy of the one-way cancellation mechanism may be theoretically challenged if the acoustic fields near the source become highly non-linear, although the validation cases suggest strong performance even in weakly to moderately non-linear regimes.

In summary, the source term approach presented by Maeda and Colonius [34] provides a highly flexible and validated methodology for generating unidirectional acoustic waves, suitable for direct numerical simulations in complex domains relevant to aeroacoustics applications, provided the numerical limitations imposed by source regularization are acknowledged and managed.

The model, however, is limited to quiescent media and based on a one-dimensional formulation. The original method developed during the thesis and presented in Section 3.2 extends this concept by formulating source terms directly from the non-linear Euler equations, without any linearization assumptions. As a result, the derived source terms inherently incorporate non-linear contributions. This approach enables the introduction of waves from arbitrarily shaped surfaces in the presence of a mean flow while consistently accounting for non-linear effects.

3.2 General Formulation

A spatial domain Ω containing an acoustic source region is considered, as shown in Fig. 3.3. An arbitrary stationary control volume V is defined such that the source region lies within it. The

outer boundary of this volume is a control surface described by the zero level set of a scalar function $f(\mathbf{x}) = 0$, with $f < 0$ in V and $f > 0$ outside V. The set of points describing the surface is denoted $\mathbf{x_s}$, with thus $f(\mathbf{x_s}) = 0$. The surface equation is constructed so that its gradient satisfies $|\boldsymbol{\nabla} f(\mathbf{x_s})| = 1$. In addition, we introduce $\boldsymbol{n} = \boldsymbol{\nabla} f(\mathbf{x_s})$ the unit normal vector to the surface.

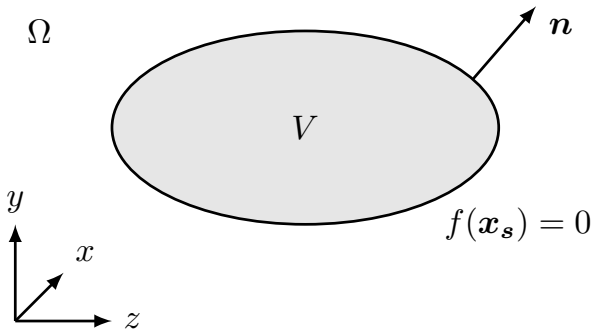

Figure 3.3: Spatial domain Ω containing a control volume V. The outer surface enclosing V is denoted by $f(\mathbf{x_s}) = 0$, and $\boldsymbol{n}$ the unit normal vector.

The non-linear Euler equations written in a perturbative form are solved throughout the whole domain Ω:

$$\frac{\partial \rho}{\partial t} + \frac{\partial}{\partial x_i}\left(\rho u_i - \rho_0 u_{0_i}\right) = 0 \tag{3.36}$$

$$\frac{\partial}{\partial t}\left(\rho u_i\right) + \frac{\partial}{\partial x_j}\left(\rho u_i u_j - \rho_0 u_{0_i} u_{0_j}\right) + \frac{\partial}{\partial x_i}\left(p - p_0\right) = 0 \tag{3.37}$$

$$\frac{\partial}{\partial t}\left(\rho e_t\right) + \frac{\partial}{\partial x_i}\left[u_i\left(\rho e_t + p\right) - u_{0_i}\left((\rho e_t)_0 + p_0\right)\right] = 0 \tag{3.38}$$

where ρ is density, t is time, x_i is the spatial coordinate along the i-direction, u_i is the component along the i-direction of the velocity vector $\mathbf{u}$, and p is the pressure. Finally, e_t is the total energy per mass unit, given by:

$$\rho e_t = \frac{p}{\gamma - 1} + \frac{1}{2}\rho u_i^2 \tag{3.39}$$

for a perfect gas, with γ the ratio of specific heats set to 1.4. Equation (3.39) is then used to calculate p. The notation $(\cdot)_0$ denotes the base flow quantities, assumed to be known as the governing equations are formulated exclusively for perturbations.

Similarly to the strategy of the Ffowcs Williams & Hawkings (FWH) analogy [19], Eqs. (3.36), (3.37) and (3.38) are then multiplied by the Heaviside function applied to the surface $H(f)$, and the source terms are identified by isolating the resulting right-hand side contributions.

For the mass conservation equation, this gives:

$$H(f)\left[\frac{\partial \rho}{\partial t} + \frac{\partial}{\partial x_i}\left(\rho u_i - \rho_0 u_{0_i}\right)\right] = 0 \tag{3.40}$$

which can be rewritten as:

$$\frac{\partial}{\partial t}\left[\rho H(f)\right] + \frac{\partial}{\partial x_i}\left[\left(\rho u_i - \rho_0 u_{0_i}\right) H(f)\right] = \left(\rho u_i - \rho_0 u_{0_i}\right) \frac{\partial H(f)}{\partial x_i} \tag{3.41}$$

We have used the relation:

$$\frac{\partial H(f)}{\partial x_i} = \frac{\partial H(f)}{\partial f}\frac{\partial f}{\partial x_i} = \delta(f)\, n_i, \tag{3.42}$$

where $\delta(f)$ is the Dirac delta function applied to f, and n_i is the normal vector component along the i-direction. Introducing Eqs. (3.42) into Eq. (3.41) leads to:

$$\frac{\partial}{\partial t}\left[\rho H(f)\right] + \frac{\partial}{\partial x_i}\left[\left(\rho u_i - \rho_0 u_{0_i}\right) H(f)\right] = \Lambda_\rho \tag{3.43}$$

where the source term reads as:

$$\Lambda_\rho = (\rho \mathbf{u} - \rho_0 \mathbf{u}_0) \cdot \mathbf{n}\, \delta(f). \tag{3.44}$$

Note that the terms on the left-hand side of Eq. (3.43) correspond to the field solved outside the control surface, that is Eq. (3.36) written for the variable $\rho H(f)$, while the remaining terms are identified as source terms on the right-hand side. The same methodology applied to the momentum and energy conservation equations provides:

$$\frac{\partial}{\partial t}\left[\rho u_i H(f)\right] + \frac{\partial}{\partial x_j}\left[\left(\rho u_i u_j - \rho_0 u_{0_i} u_{0_j}\right) H(f)\right] + \frac{\partial}{\partial x_i}\left[(p - p_0)\, H(f)\right] = \boldsymbol{\Lambda_{\rho u}} \tag{3.45}$$

$$\frac{\partial}{\partial t}\left[\rho e_t H(f)\right] + \frac{\partial}{\partial x_i}\left\{\left[u_i\left(\rho e_t + p\right) - u_{0_i}\left((\rho e_t)_0 + p_0\right)\right] H(f)\right\} = \Lambda_{\rho e_t} \tag{3.46}$$

with the source terms:

$$\boldsymbol{\Lambda_{\rho u}} = \left[\rho(\mathbf{u}\cdot\mathbf{n})\mathbf{u} - \rho_0(\mathbf{u}_0\cdot\mathbf{n})\mathbf{u}_0 + (p - p_0)\,\mathbf{n}\right]\delta(f) \tag{3.47}$$

$$\Lambda_{\rho e_t} = \left[(\rho e_t + p)\mathbf{u} - ((\rho e_t)_0 + p_0)\mathbf{u}_0\right]\cdot\mathbf{n}\,\delta(f) \tag{3.48}$$

The three newfound source terms at the right-hand side in Eq. (3.43), (3.45), and (3.46) Λ_ρ, $\boldsymbol{\Lambda_{\rho u}}$ and $\Lambda_{\rho e_t}$ are respectively the sources terms for mass, momentum and energy conservation equations. These sources are continuously distributed along the entire outer surface f. They enable the signal generated by the source region within the volume V to be injected into the computational domain in the outward direction only. No propagation should be observed in the volume V.

3.3 Numerical Setup

The Euler equations are solved in their conservative form written in Cartesian coordinates:

$$\frac{\partial \boldsymbol{U}}{\partial t} + \frac{\partial \boldsymbol{E}}{\partial x} + \frac{\partial \boldsymbol{F}}{\partial y} + \frac{\partial \boldsymbol{G}}{\partial z} = \boldsymbol{\Lambda}, \tag{3.49}$$

with

$$\begin{aligned}
\boldsymbol{U} &= (\rho, \rho u, \rho v, \rho w, \rho e_t) \\
\boldsymbol{E} &= \left(\rho u, \rho u^2 + p, \rho uv, \rho uw, u\left(\rho e_t + p\right)\right) \\
\boldsymbol{F} &= \left(\rho v, \rho uv, \rho v^2 + p, \rho vw, v\left(\rho e_t + p\right)\right) \\
\boldsymbol{G} &= \left(\rho w, \rho uw, \rho vw, \rho w^2 + p, w\left(\rho e_t + p\right)\right) \\
\boldsymbol{\Lambda} &= \left(\Lambda_\rho, \Lambda_{\rho u}, \Lambda_{\rho v}, \Lambda_{\rho w}, \Lambda_{\rho e_t}\right)
\end{aligned}$$

where $\boldsymbol{U}$ is the vector of conservative variables, $\boldsymbol{E}, \boldsymbol{F}$, and $\boldsymbol{G}$ are the fluxes vectors, $\boldsymbol{\Lambda}$ is the source term vector defined in Eqs. (3.44), (3.47), and (3.48) over $f(\boldsymbol{x}_s) = 0$, $\boldsymbol{x} = (x, y, z)$ and $\boldsymbol{u} = (u, v, w)$. As mentioned in the previous section, Eq. (3.49) is solved for perturbative variables with respect to a given based flow. The variables are initialized with their ambient values, that is $\boldsymbol{U}(\mathbf{x}, t = 0) = \left(\rho_0, \rho_0 u_0, \rho_0 v_0, \rho_0 w_0, (\rho e_t)_0\right)$.

The Euler equations are solved using a finite difference approach in a uniformly spaced Cartesian grid, i.e. $\Delta x = \Delta y = \Delta z$ where Δx, Δy, Δz are the grid sizes in the x-, y-, and z- direction, respectively. Spatial derivatives are computed with a low dispersion and low dissipation fourth-order, 11-point finite difference scheme [5]. Temporal integration is performed using a low-storage, fourth-order, six-stage Runge–Kutta scheme. The source terms are introduced at the last sub-step of each iteration of the temporal scheme. This choice was made with the unducted single fan application presented in Chapter 5 in mind, where the input signal is obtained from a RANS simulation and is not analytically defined. A selective 11-point filter is applied throughout the computational domain in order to suppress grid-to-grid oscillations. Perfectly Matched Layers (PML) [8] are implemented near the domain boundaries to absorb outgoing acoustic waves. All simulations are conducted with a Courant–Friedrichs–Lewy (CFL) number set to 0.5.

The source terms involve a Dirac delta function that has to be approximated for discretization. For that, we use a normalized Gaussian-shaped spatial support defined by:

$$\delta_b[f(\boldsymbol{x})] = \frac{1}{\sqrt{\pi} b} \exp\left(-\frac{f(\boldsymbol{x})^2}{b^2}\right) \tag{3.50}$$

with $b = b_w/\sqrt{\log 2}$ where b_w is the Gaussian half-width. It can be remarked that δ_b tends to the Dirac function δ when b tends to zero. In the following, $b_w/\Delta x = 1$ is chosen to ensure that the sources remain compact. Choosing $b_w/\Delta x < 1$ may lead to numerical instability and increased error, whereas selecting a value that is too large spreads the sources intensity over a wider region,

also increasing numerical error.

It should also be noted that approximating the Dirac delta function transforms the source terms from a surface distribution to a volumetric one, spread over the surface. The imposed acoustic fields have also to be extended from the control surface to the volumetric source. For that, we keep the same values along the direction normal to the surface. In other words, the width size of the source is assumed to be small with respect to a typical acoustic wavelength.

3.4 Results

Four configurations are considered to evaluate the proposed methodology. The first case examines the injection of an oblique plane wave. The second case addresses the injection of a non-linear harmonic signal that evolves into a sawtooth wave train. The third and fourth cases investigate the injection of cylindrical and spherical waves generated by a monopole in a uniform mean flow, respectively.

In the present methodology, acoustic waves are introduced by imposing the acoustic field on a predefined injection surface. For the three academic cases, this field is specified analytically. In the unducted single fan application presented in Chapter 5, the imposed field is obtained from a previous computational fluid dynamics simulation.

A perfect gas is considered, and p_0, ρ_0, and c_0 denote the pressure, density and speed of sound of the medium at rest. For the first three academic cases, all the variables are made dimensionless with the speed of sound c_0 as velocity scale, ρ_0/γ as density scale, $\rho_0 c_0^2$ as pressure scale, an arbitrary length L and a time scale L/c_0. The reported results are however plotted with dimensional primitive variables for the time and spatial coordinates.

Also, to clearly separate the quantities in the Euler equations from those imposed in the source terms, the latter are indicated in the following with a tilde ($\tilde{}$).

3.4.1 Oblique plane waves

The objective of the first problem is to introduce an oblique plane wave propagating at an angle θ with respect to the horizontal x-axis in a medium at rest. The injection domain is defined by $f(x, y) = x$ (corresponding to $\boldsymbol{x_s} = \ (0, y)$), that is along a vertical line as illustrated in Fig. 3.4. The acoustic pressure $\tilde{p}'$ and acoustic velocity $\tilde{\boldsymbol{u}}'$ for an oblique plane wave read:

$$\tilde{p}'(x, y, t) = A \cos\left[\omega\left(t - \frac{x}{c_0}\cos\theta - \frac{y}{c_0}\sin\theta\right)\right] \tag{3.51}$$

$$\tilde{\boldsymbol{u}}'(x, y, t) = \frac{A}{\rho_0 c_0}\cos\left[\omega\left(t - \frac{x}{c_0}\cos\theta - \frac{y}{c_0}\sin\theta\right)\right]\boldsymbol{\nu} \tag{3.52}$$

where A denotes the wave amplitude and is set to 10^{-4} to be in the linear regime, ω is the angular frequency set to π and $\boldsymbol{\nu} = (\cos\theta, \sin\theta)$ is the unit wave vector.

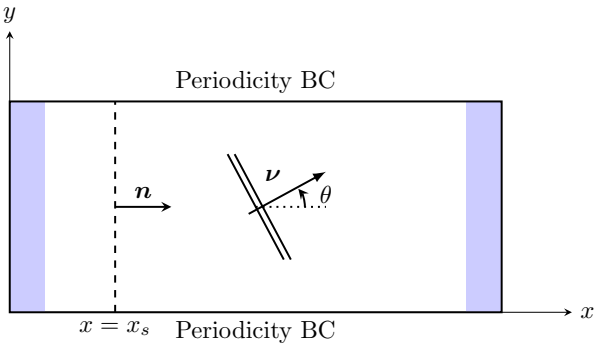

Figure 3.4: Two-dimensional domain used to simulate oblique waves introduced along the vertical line $x = x_s$, with wave vector $\boldsymbol{\nu}$ inclined at an angle θ relative to the horizontal x-axis. Blue regions at the left and right boundaries represent the PML, while periodic boundary conditions are applied along the top and bottom edges.

For this first case, small amplitude waves are considered in order to be able to derive an analytical solution. The expressions of the source terms to be placed on the vertical line at $x = 0$ are determined by using Eqs. (3.44), (3.47) and (3.48). They are thus linearized in neglecting second order terms. By noting that the unit vector normal to the injection line is $\boldsymbol{n} = (1, 0)$, this gives:

$$\Lambda_\rho(\boldsymbol{x}, t) = \rho_0 \tilde{u}'\left(\boldsymbol{x_s}, t\right)\, \delta_b(f) \tag{3.53}$$

$$\Lambda_{\rho u}(\boldsymbol{x}, t) = \tilde{p}'\left(\boldsymbol{x_s}, t\right)\, \delta_b(f) \tag{3.54}$$

$$\Lambda_{\rho v}(\boldsymbol{x}, t) = 0 \tag{3.55}$$

$$\Lambda_{\rho e_t}(\boldsymbol{x}, t) = \frac{\gamma}{\gamma - 1} p_0 \tilde{u}'\left(\boldsymbol{x_s}, t\right)\, \delta_b(f) \tag{3.56}$$

It can be shown analytically that the source terms given in Eqs. (3.53)-(3.56) generate an oblique plane wave whose properties match those in Eq. (3.51). To demonstrate this, the Euler equations are manipulated by following Maeda and Colonius [34] to recast them into the form of a wave equation:

$$\frac{1}{c_0^2}\frac{\partial^2 p'}{\partial t^2} - \nabla^2 p' = S \tag{3.57}$$

where the right-hand side reads

$$S = \frac{\partial \Lambda_\rho}{\partial t} - \nabla \cdot \boldsymbol{\Lambda_{\rho u}} \tag{3.58}$$

The pressure field is then calculated by carrying out the convolution between the source term S and the free-space Green function $g_0(x, y, z, t)$,

$$p'\left(x, y, t\right) = (g_0 * S), \tag{3.59}$$

which leads for $|x| \gg b$ to

$$p' = A_b H(x) \cos\left[\omega\left(t - \frac{x}{c_0}\cos\theta - \frac{y}{c_0}\sin\theta\right)\right] \tag{3.60}$$

with

$$A_b = A \exp\left(-\frac{k_0^2 b^2 \cos\theta^2}{4}\right) \tag{3.61}$$

and $k_0 = \omega/c_0$. Providing that $k_0 b$ is sufficiently small, the acoustic pressure field corresponds to that for the propagation of the oblique plane wave in Eq. (3.51) for $x > 0$. In addition, it is found that the acoustic pressure field is null for $x < 0$. Details on the calculation of the convolution are given in Appendix A.

For numerical simulations, the grid spacing is set to $\Delta x = 0.05$, providing 44 points per wavelength. The computational domain consists of 401×201 points in the x and y directions, respectively. The length of the computational domain is selected to match the y-wise periodicity described in Eqs. (3.51-3.52). As shown in Fig. 3.4, PML are applied at the left and right boundaries, while periodic boundary conditions are imposed on the top and bottom edges. The solution is computed up to $t = 50$.

A snapshot of the acoustic pressure field is shown in Fig. 3.5. As expected, wave propagation is confined to the direction of increasing x, while the signal in the opposite direction remains at least three orders of magnitude lower. A comparison between the analytical and numerical solutions at the final time step, evaluated along the horizontal line $y = 3$, is plotted in Fig. 3.6. An excellent agreement is observed in both phase and amplitude. Beyond $x = 17$, the PML applied at the right boundary progressively attenuates the numerical solution to zero.

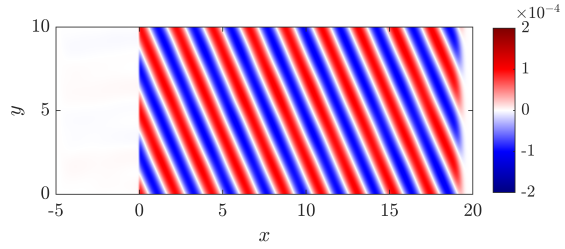

Figure 3.5: Snapshot of the pressure field at $t = 50$ generated by the source terms located at $x = 0$. The wave propagates in the positive x-direction, while only a negligible amplitude is observed in the opposite direction.

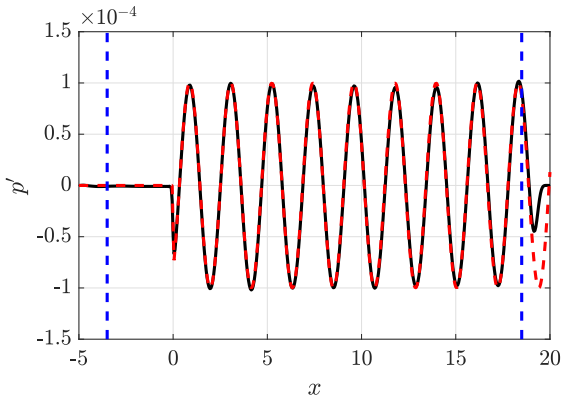

Figure 3.6: Comparison between the analytical solution (dashed red line) and the numerical solution (solid black line) along the horizontal line $y = 3$.

3.4.2 Sawtooth wave train

This case considers a one-dimensional simulation in which a harmonic signal is introduced at a point within the computational domain. The imposed perturbation $\tilde{p}'$ has an amplitude $\Delta p_0 = 0.03 p_0$, which is sufficient to induce non-linear propagation effects. In non-linear acoustics, the compressive (positive) phase of the wave propagates at a higher speed than the expansive (negative) phase, leading to progressive wave steepening and eventual shock formation. This wave-steepening mechanism generates additional harmonics beyond the fundamental frequency of the single-frequency source. Following shock formation, the amplitudes of both the positive and negative pressure peaks decrease with increasing propagation distance [41, 42].

Shock formation distance

The shock formation distance is denoted by $\bar{x}$ and, for a medium at rest, is defined as:

$$\bar{x} = \frac{\rho_0 c_0^2}{\beta k_0 \Delta p_0} \tag{3.62}$$

where $\beta = (\gamma + 1)/2$ is the non-linear factor for air.
In the presence of a uniform mean flow u_0, the shock formation distance is modified by convective effects. To illustrate this influence, the assumption of weak non-linearity is adopted, which enables the formulation of the governing equation for velocity perturbations u' for a sinusoidal wave:

$$\frac{\partial u'}{\partial t} + (c_0 + u_0 + \beta u')\frac{\partial u'}{\partial x} = 0 \tag{3.63}$$

This equation admits an exact implicit solution, known as the Poisson solution. For a wave generated by a source at $x = 0$ and defined by an initial condition at $t = 0$, the Poisson solution can be expressed as:

$$u'(x,t) = g[t - x/(c_0 + u_0 + \beta u'(x,t))] \tag{3.64}$$

Since $p' = p'(u')$, retaining only the first-order term in the speed of sound, consistent with the weakly non-linear acoustic approximation, the linear acoustic relation $u' = p'/(\rho_0 c_0)$ can be employed to derive the acoustic pressure propagation equation:

$$\frac{\partial p'}{\partial t} + c_0 \left(1 + M + \beta \frac{p'}{\rho_0 c_0^2}\right) \frac{\partial p'}{\partial x} = 0 \tag{3.65}$$

where M is the Mach number.
For moderate amplitudes, the non-linear propagation equation is identical for velocity and pressure fluctuations. At very high amplitudes, however, this equivalence no longer holds.
For a source-type problem in which the boundary condition at $x = 0$ is prescribed as a function of time, $u'(x = 0, t) = g(t)$, the distance at which a shock first forms can be determined. This distance corresponds to the location where the waveform develops an infinite slope.
To identify the position at which the waveform attains a vertical slope, the time derivative of the Poisson solution in Eq. (3.64) is evaluated:

$$\begin{aligned} \frac{\partial u'}{\partial t} &= \left(1 + \frac{\beta x}{(c_0 + u_0 + \beta u')^2} \frac{\partial u'}{\partial t}\right) g' \\ &= \frac{g'}{1 - \beta x (c_0 + u_0 + \beta u')^{-2} g'} \end{aligned} \tag{3.66}$$

If the acoustic fluctuations remain moderate in amplitude compared with $c_0 + u_0$, the approximation $c_0 + u_0 + \beta u' \approx c_0(1 + M)$ can be adopted. The time derivative of u' becomes unbounded when the denominator vanishes. Consequently, the shock formation distance is given by:

$$\bar{x} = \frac{c_0^2 (1 + M)^2}{\beta g'_{\max}} \tag{3.67}$$

where $g'_{\max}$ denotes the maximum value of the derivative of the function g.
For a harmonic excitation defined as $g(t) = U_0 \sin(\omega t)$, the expression becomes:

$$\bar{x} = \frac{c_0^2 (1 + M)^2}{\beta U_0 \omega} \tag{3.68}$$

It should be noted that this expression applies to a wave propagating in the same direction as the mean flow. For a wave traveling opposite to the flow, the Mach number appears with a negative sign.

Harmonics evolution

The non-dimensional parameter $\sigma = x/\bar{x}$ is introduced, with shock formation occurring at $\sigma = 1$. The acoustic field is conventionally partitioned into three regions: a shock-free region for $\sigma \leq 1$, a transition region for $1 < \sigma < 3$, and a sawtooth region for $\sigma \geq 3$. A unified analytical solution describing the harmonic evolution across these three regions is provided by Hamilton *et al.* [42]:

$$B_n = \frac{2}{n\pi} P_{\mathrm{sh}} + \frac{2}{n\pi\sigma} \int_{\Phi_{\mathrm{sh}}}^{\pi} \cos\left[n\left(\Phi - \sigma \sin\Phi\right)\right] \, \mathrm{d}\Phi \tag{3.69}$$

where B_n is the amplitude of the nth harmonic, $P_{\mathrm{sh}} = p'/\Delta p_0$ and $\Phi = \omega\phi$, with $\phi = t - x/c_0 + \beta x p'/(\rho_0 c_0^3)$ the Earnshaw variable.

In the analytical solution given in Eq. (3.69), the first term corresponds to the solution in the sawtooth region, whereas the second term represents the Fubini's solution in the shock-free region, and it rapidly vanishes in the sawtooth region as the lower integration limit approaches the upper limit ($\Phi_{\mathrm{sh}} \to \pi$). The respective contributions of the two terms are illustrated in Fig. 3.7. The Fubini's solution dominates in the shock-free region for $\sigma < 1$, whereas the sawtooth solution is valid for $\sigma > 3$. In the transition region, both terms are combined to account for their simultaneous contributions.

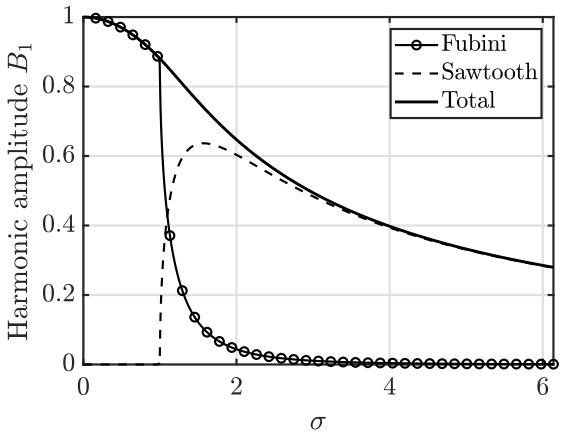

Figure 3.7: Normalized amplitude of the fundamental harmonic B_1 as a function of σ for a wave generated by a monofrequency source [42].

Numerical simulation

The one-dimensional computational domain comprises 3001 grid points over a total length of $L_x = 300$. Three simulations were conducted: one with the fluid at rest, one with a uniform flow u_0 opposing the direction of acoustic wave propagation, and one with a uniform flow aligned with the acoustic wave propagation. In the quiescent-fluid case, the discretization provides 41 points per wavelength for a signal frequency of $f = 0.1$ Hz. The simulation time is set to $T = 600$ s for all three cases. Perfectly Matched Layers are applied at the domain boundaries to absorb outgoing acoustic waves.

The acoustic field imposed in the computational domain at $x = 0$ is defined by the following

relations:

$$\tilde{p}'(t) = \Delta p_0 \cos(\omega t) \tag{3.70}$$

$$\tilde{u}'(t) = \frac{2c_0}{\gamma - 1}\left[\left(1 + \frac{\tilde{p}'}{p_0}\right)^{(\gamma-1)/2\gamma} - 1\right] \tag{3.71}$$

$$\tilde{\rho}'(t) = \rho_0\left[\left(1 + \frac{\tilde{p}'}{p_0}\right)^{1/\gamma} - 1\right] \tag{3.72}$$

where the isentropic relations are used for the imposed acoustic velocity field $\tilde{u}'$ and density field $\tilde{\rho}'$.

The source terms used in non-linear Euler equations are defined as:

$$\Lambda_\rho = \left(\rho_0\tilde{u}' + \tilde{\rho}'u_0 + \tilde{\rho}'\tilde{u}'\right)\,\delta_b(f) \tag{3.73}$$

$$\Lambda_{\rho u} = \left(2\rho_0 u_0\tilde{u}' + \rho_0\tilde{u}'^2 + \tilde{\rho}'u_0^2 + 2\tilde{\rho}'u_0\tilde{u}' + \tilde{\rho}'\tilde{u}'^2 + \tilde{p}'\right)\,\delta_b(f) \tag{3.74}$$

$$\begin{aligned}\Lambda_{\rho e_t} = \Bigg\{&\frac{\gamma}{\gamma-1}\left[p_0u' + p'\left(u_0 + u'\right)\right] + \frac{3}{2}\left(\rho_0 + \tilde{\rho}'\right)\left(u_0 + \tilde{u}'\right)u_0\tilde{u}' \\ &+\frac{1}{2}\left[\rho_0\tilde{u}'^3 + \tilde{\rho}'\left(u_0^3 + \tilde{u}'^3\right)\right]\Bigg\}\,\delta_b(f)\end{aligned} \tag{3.75}$$

It should be noted that higher-order terms are also retained in this case, owing to the non-linear nature of the problem under consideration.

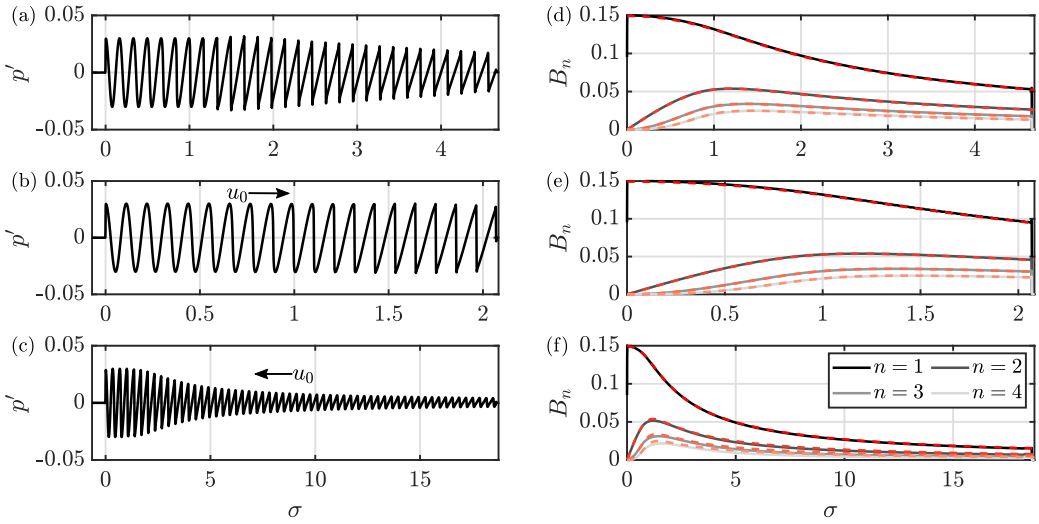

Figure 3.8: Acoustic pressure as a function of σ for (a) $u_0 = 0$, (b) $u_0 = 0.5$, and (c) $u_0 = -0.5$; black arrows indicate the flow direction. Panels (d–f) show the corresponding harmonic amplitudes B_n (solid black) compared with the analytical solution (dashed red) given in Eq. (3.69).

The results of the three simulations are presented in Fig. 3.8. Subplots (a–c) in the first column show the acoustic pressure as a function of σ at $T = 600$ s. In all cases, with and without uniform

flow, the acoustic signal is correctly introduced at the origin of the computational domain at $x = 0$. The presence of a mean flow markedly alters the shock formation distance $\bar{x}$, corresponding to $\sigma = 1$. Subplots (d–f) in the second column display the amplitudes B_n of the first four harmonics as functions of σ. In all configurations, the numerical results exhibit excellent agreement with the theoretical predictions, thereby validating the proposed wave injection method in the non-linear regime.

An academic test case involving the injection of a single N-wave is presented in Appendix B, showing equally good results for the introduction of a wave with a pronounced discontinuity.

3.4.3 2D Monopole with uniform flow

This second case aims at injecting cylindrical waves generated by a monopole immersed in a two-dimensional uniform base flow along the y-axis, with a Mach number $M_y = v_0/c_0 = 0.8$.

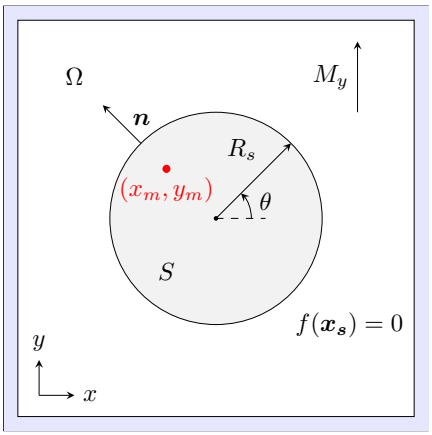

Figure 3.9: Two-dimensional computational domain Ω, featuring a circular control surface $S \in \Omega$ centered at the origin with radius R_s. The acoustic monopole (in red) is located at (x_m, y_m) within the control surface. The blue region denotes the PML used for wave absorption.

As shown in Fig. 3.9, the control surface is a circle centered at the origin of the domain and with a radius $R_s = 5$. Its surface equation is $f(x, y) = \sqrt{x^2 + y^2} - R_s$, corresponding to $\boldsymbol{x_s} = (R_s \cos\theta, R_s \sin\theta)$ with θ between 0 and 2π. The monopole position (x_m, y_m) does not coincide with the center of the control surface. The normal vector to the control surface is defined as:

$$\boldsymbol{n} = \begin{pmatrix} n_x \\ n_y \end{pmatrix} = \begin{pmatrix} \cos\theta \\ \sin\theta \end{pmatrix} \tag{3.76}$$

where n_x and n_y denote the components of the normal vector in the x- and y-directions respectively, and θ is the angle formed with the horizontal x-axis.

In complex notation, the acoustic pressure field generated by a monopole immersed in a uniform flow reads:

$$\tilde{p'}(x, y, t) = -\rho_0 \left(\frac{\partial}{\partial t} + v_0 \frac{\partial}{\partial y} \right) \phi(x, y, t) \tag{3.77}$$

where $\phi(x, y, t)$ is the velocity potential defined as,

$$\phi\left(x, y, t\right) = -\frac{\mathrm{i}A}{4\beta} H_0^{(1)}\left(\frac{k_0}{\beta}\sqrt{(x-x_m)^2 + \frac{(y-y_m)^2}{\beta^2}}\right) \exp\left(-\frac{\mathrm{i}k_0 M_y}{\beta^2}(y-y_m)\right) \exp\left(-\mathrm{i}\omega t\right)$$

In the above equation, $H_0^{(1)}$ is the Hankel function of the first kind, $\beta = (1 - M_y^2)^{1/2}$ is the Prandtl–Glauert factor and A is the source amplitude. The acoustic density is simply given by $\tilde{\rho}'(\boldsymbol{x}, t) = \tilde{p}'(\boldsymbol{x}, t)/c_0^2$ and the acoustic velocity field is $\tilde{\boldsymbol{u}}' = \nabla\phi$.
Equations (3.44), (3.47), and (3.48) are again used to derive the source terms,

$$\Lambda_\rho\left(\boldsymbol{x}, t\right) = \left(\rho_0 \tilde{u}_n' + \tilde{\rho}' v_0 \sin\theta\right)\, \delta_b(f) \tag{3.78}$$

$$\Lambda_{\rho u}\left(\boldsymbol{x}, t\right) = \left(\rho_0 v_0 \tilde{u}' \sin\theta + \tilde{p}' \cos\theta\right)\, \delta_b(f) \tag{3.79}$$

$$\Lambda_{\rho v}\left(\boldsymbol{x}, t\right) = \left(\rho_0 v_0 \tilde{u}_n' + \rho_0 v_0 \tilde{v}' \sin\theta + \tilde{\rho}' v_0^2 \sin\theta + \tilde{p}' \sin\theta\right)\, \delta_b(f) \tag{3.80}$$

$$\Lambda_{\rho e_t}\left(\boldsymbol{x}, t\right) = \left[\left(\frac{\gamma p_0}{\gamma - 1} + \frac{1}{2}\rho_0 v_0^2\right)\tilde{u}_n' + \frac{\gamma}{\gamma - 1} v_0 \tilde{p}' \sin\theta + \rho_0 v_0^2 \tilde{v}' \sin\theta + \frac{1}{2} v_0^3 \tilde{\rho}' \sin\theta\right]\, \delta_b(f) \tag{3.81}$$

where $\tilde{u}_n'$ denotes the velocity component normal to the surface f, namely $\tilde{u}_n' = \tilde{\boldsymbol{u}}' \cdot \boldsymbol{n} = \tilde{u}' \cos\theta + \tilde{v}' \sin\theta$. All the acoustic quantities are obtained by taking the real part of the analytical field evaluated at $(R_s \cos\theta, R_s \sin\theta, t)$. As a reminder, the values of the imposed acoustic quantities along the direction normal to the control surface are set equal to those on the surface. For this case, this implies that $\tilde{p}'$, $\tilde{u}'$, $\tilde{v}'$, and $\tilde{\rho}'$ are constant for a given value of θ.
The source amplitude A is set to 10^{-3} and the angular frequency $\omega = 0.1$. The grid spacing is set to $\Delta x = 0.1$, providing 150 points per wavelength in the upstream-propagating wave region. The computational domain consists of 1001×1001 points in the x and y directions, respectively. The solution is computed up to $T = 300$.
A snapshot of the pressure field is shown in Fig. 3.10. The circular control surface is centered at the origin of the computational domain, while the monopole, marked by a red cross, is located at $(x_m, y_m) = (3, 3)$. The resulting acoustic wavefronts are clearly visible and exhibit asymmetry due to the convective effects of the mean flow. A quantitative comparison between the numerical and analytical solutions along six distinct lines is provided in Fig. 3.11, demonstrating excellent agreement in both amplitude and phase. For the lines $y = 0$ and $x = 0$, shown in Figs. 3.11 (b) and (c) respectively, a discontinuity appears for $x, y \in (-5, 5)$, corresponding to the region enclosed by the control surface. Within this region, no acoustic wave is introduced, a property of the present formulation.

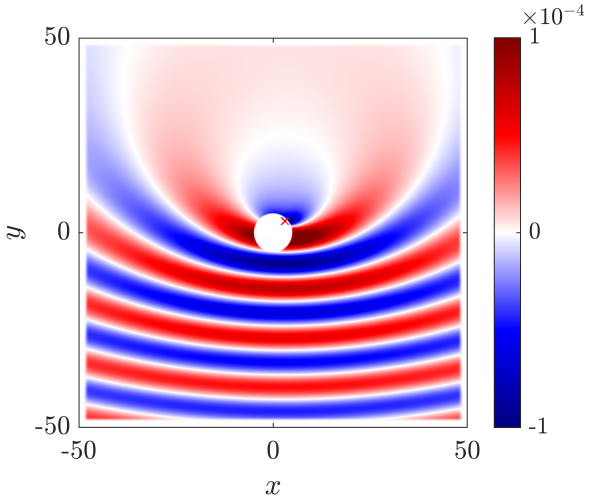

Figure 3.10: Acoustic pressure field at $t = 300$ generated by a two-dimensional monopole immersed in a uniform flow with Mach number $M_y = 0.8$. The monopole, indicated by the red cross, is located at $(x_m, y_m) = (3, 3)$ within a circular control surface centered at the origin with radius $R_s = 5$.

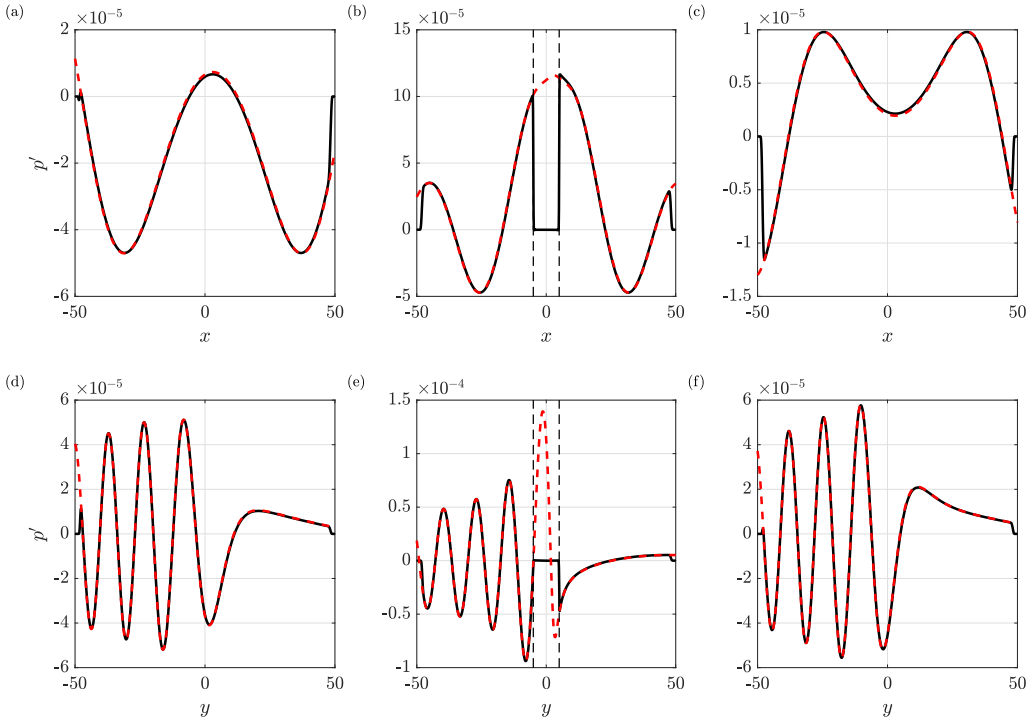

Figure 3.11: Comparison between the analytical solution (dashed red line) and the numerical solution (solid black line) for a 2D monopole immersed in uniform flow at (a) $y = -30$, (b) $y = 0$, (c) $y = 30$, (d) $x = -30$, (e) $x = 0$, (f) $x = 30$. The black vertical dashed lines denote the boundaries of the surface.

A convergence study is carried out by varying the mesh spacing Δx while keeping all other simulation parameters constant. The time-dependent pressure signal is recorded at each iteration

at the point $(x, y) = (0.4, -14)$. For each simulation, the L2-norm error between the analytical and the numerical solutions is computed as follows:

$$\varepsilon = \sqrt{\frac{\int_0^T \left(\mathrm{Re}[\tilde{p}'] - p'\right)^2 \mathrm{d}t}{\int_0^T \mathrm{Re}[\tilde{p}']^2 \mathrm{d}t}}$$

The results for the evolution of ϵ are plotted in Fig. 3.12. The mesh spacing Δx ranges from 0.1 to 1.6, corresponding to 150 and 10 points per wavelength, respectively. For spatial steps between 0.8 and 1.6, the error decreases with a third-order slope. As the mesh is further refined, the convergence rate reduces to between first and second order. This behavior arises because the source terms are introduced only during the final sub-step of the Runge-Kutta cycle, rather than at every sub-step, thereby reducing the scheme's order of convergence. Although the finite-difference numerical schemes employed maintain good accuracy up to five points per wavelength, progressive mesh coarsening also reduces the number of volumetric sources distributed on the surface. This reduction diminishes the effectiveness of the proposed method, due to the combined impact of fewer sources and the increased width of the Gaussian support. A potential solution is the adoption of a non-uniform grid refined in the vicinity of the control surface. This approach would enable improved management of signal injection into the computational domain while retaining a coarser discretization elsewhere, where the mesh is used primarily for wave propagation.

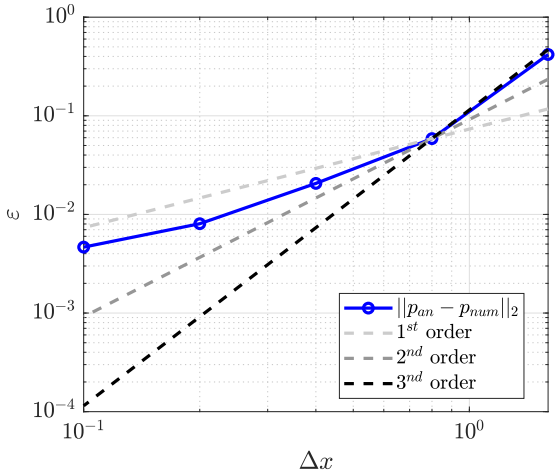

Figure 3.12: L2-norm error between the numerical solution of the two-dimensional monopole case and the analytical solution, evaluated for varying mesh resolutions Δx.

A parametric analysis was conducted to assess the effect of varying the half-width of the Gaussian support $b_{wx}/\Delta x$. The results, shown in Fig. 3.13, indicate that when the support width satisfies $b_{wx}/\Delta x < 1$, the error increases rapidly due to numerical instabilities. Conversely, values of $b_{wx}/\Delta x > 1$ spread the source over a larger volume, reducing its effective intensity and thereby increasing the error. The optimal choice is therefore $b_{wx}/\Delta x = 1$.

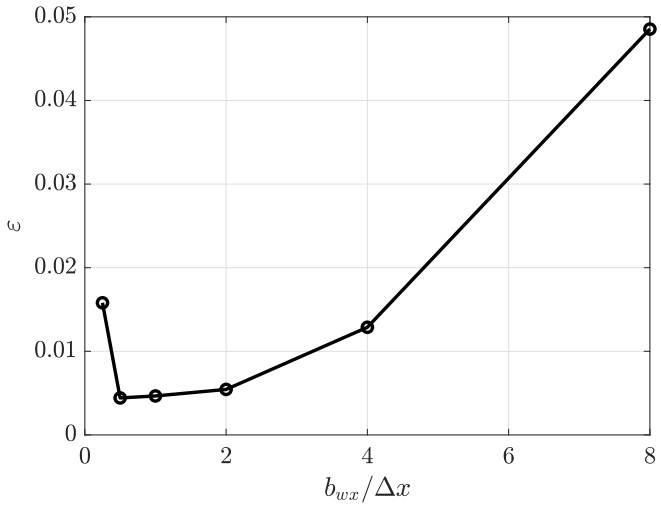

Figure 3.13: Numerical error ε for different Gaussian half-width b_w.

3.4.4 3D Monopole with uniform mean flow

This third configuration extends the two-dimensional case to three dimensions. Introduction of spherical waves generated by a monopolar source in a uniform flow is investigated. The monopole is located at $\boldsymbol{x}_m = (x_m, y_m, z_m)$ and is immersed in a uniform flow at $M_x = 0.8$ along the x-axis. As illustrated in Fig. 3.14, the control surface is a cylinder centered at the origin, aligned with the x-direction, and enclosing the source, with radius $R_s = 10$ and length $L = 30$.

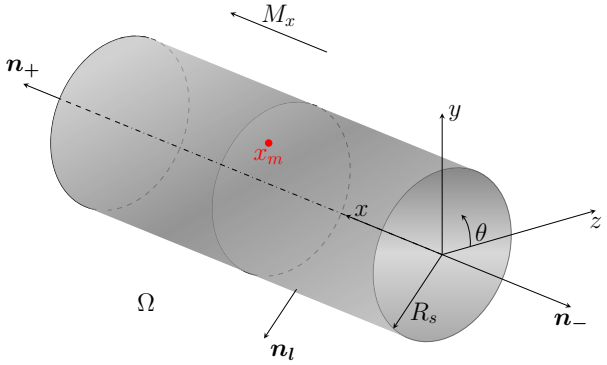

Figure 3.14: Three-dimensional scheme of a cylindrical control volume V with radius R_c, enclosing an acoustic monopole located at $\boldsymbol{x}_m = (x_m, y_m, z_m)$. The configuration is immersed in a uniform flow of Mach number M_x directed along the x-axis.

The lateral surface has for equation $f(x, y, z) = \sqrt{y^2 + z^2} - R_s$ for $-L/2 < x < L/2$. The unit normal vector to the lateral surface of the cylinder $\boldsymbol{n}_l$ is defined as:

$$\boldsymbol{n}_l = (0, \sin\theta, \cos\theta) \tag{3.82}$$

where $\theta = \arctan\big(y/z\big)$ denotes the angle formed with the positive z-axis in a generic yz plane. The two bases have for equations $f(x, y, z) = \pm x - L/2$ for $\sqrt{y^2 + z^2} < R_s$. The unit vectors

normal to the two bases of the cylinder are defined respectively as $\boldsymbol{n}_{\pm} = (\pm 1, 0, 0)$. The injection of the acoustic waves generated by a monopole source in a uniform flow relies on the corresponding analytical solution. From the velocity potential given by:

$$\phi(\boldsymbol{x}, t) = \frac{A}{4\pi R_1} \exp\left[-\mathrm{i}\omega\left(t - \frac{R_2}{c_0}\right)\right] \tag{3.83}$$

with

$$R_1 = \sqrt{(x - x_m)^2 + \beta^2\left[(y - y_m)^2 + (z - z_m)^2\right]}, \tag{3.84}$$

$$R_2 = \frac{R_1 - M_x\,(x - x_m)}{\beta^2}, \tag{3.85}$$

and $\beta^2 = 1 - M_x^2$, the acoustic pressure $\tilde{p}'$ and velocity $\tilde{\boldsymbol{u}}' = \left(\tilde{u}', \tilde{v}', \tilde{w}'\right)$ can be determined as follows,

$$\tilde{p}'(\mathbf{x}, t) = -\rho_0\left(\frac{\partial}{\partial t} + u_0\frac{\partial}{\partial x}\right)\phi(\mathbf{x}, t) \tag{3.86}$$

$$\tilde{\boldsymbol{u}}'(\mathbf{x}, t) = \boldsymbol{\nabla}\boldsymbol{\phi}\,(\mathbf{x}, t) \tag{3.87}$$

with $u_0 = M_x c_0$.

The source terms can then be formulated using Eqs. (3.44), (3.47), and (3.48). For the lateral surface of the cylinder ($-L/2 < x < L/2$), the source terms are expressed as:

$$\Lambda_{\rho}\,(\mathbf{x}, t) = \rho_0 \tilde{u}'_n\,\delta_b(f) \tag{3.88}$$

$$\Lambda_{\rho u}\,(\mathbf{x}, t) = \rho_0 u_0 \tilde{u}'_n\,\delta_b(f) \tag{3.89}$$

$$\Lambda_{\rho v}\,(\mathbf{x}, t) = \tilde{p}'\sin\theta\,\delta_b(f) \tag{3.90}$$

$$\Lambda_{\rho w}\,(\mathbf{x}, t) = \tilde{p}'\cos\theta\,\delta_b(f) \tag{3.91}$$

$$\Lambda_{\rho e_t}\,(\mathbf{x}, t) = \left(\frac{\gamma}{\gamma - 1}p_0 + \frac{1}{2}\rho_0 u_0^2\right)\tilde{u}'_n\,\delta_b(f) \tag{3.92}$$

where $\tilde{u}'_n = \tilde{v}'\sin\theta + \tilde{w}'\cos\theta$ denotes the velocity component in the direction normal to the lateral surface. The acoustic quantities in the source terms are those from the analytical solution on the control surface evaluated at $(x, R_s\sin\theta, R_s\cos\theta, t)$ by taking the real part.

For the bases of the cylinders with normal vectors $\boldsymbol{n}_{\pm}$, the source terms are given by:

$$\Lambda_{\rho}\left(\mathbf{x},t\right) = \pm\left(\rho_0\tilde{u}' + \tilde{\rho}'u_0\right)\,\delta_b(f) \tag{3.93}$$

$$\Lambda_{\rho u}\left(\mathbf{x},t\right) = \pm\left(2\rho_0 u_0\tilde{u}' + \tilde{\rho}'u_0^2 + \tilde{p}'\right)\,\delta_b\left(f\right) \tag{3.94}$$

$$\Lambda_{\rho v}\left(\mathbf{x},t\right) = \pm\rho_0 u_0\tilde{v}'\,\delta_b\left(f\right) \tag{3.95}$$

$$\Lambda_{\rho w}\left(\mathbf{x},t\right) = \pm\rho_0 u_0\tilde{w}'\,\delta_b\left(f\right) \tag{3.96}$$

$$\Lambda_{\rho e_t}\left(\mathbf{x},t\right) = \pm\left[\frac{\gamma}{\gamma-1}\left(\tilde{p}'u_0 + p_0\tilde{u}'\right) + \frac{3}{2}\rho_0 u_0^2\tilde{u}' + \frac{1}{2}\tilde{\rho}'u_0^3\right]\,\delta_b(f) \tag{3.97}$$

Once again, the imposed acoustic quantities on the control surfaces are evaluated at $(x = \pm L/2, y, z, t)$.

The monopole amplitude A is set to 10^{-3} and the angular frequency $\omega = 0.314$. The grid spacing is set to $\Delta x = 0.25$, providing 24 points per wavelength in the upstream-propagating wave region. The computational domain consists of $401 \times 281 \times 461$ points in the x, y, and z directions, respectively. The solution is computed up to $t = 200$. The computational cost of the simulation is 6 hours of wall-clock time on a single compute node utilizing 32 OpenMP threads. The acoustic pressure signal at the final time step is shown in Fig. 3.15 (a) and (b) on the yz and xz planes, respectively. The control surface boundaries are clearly identifiable. A comparison between the analytical and numerical solutions is provided in Fig. 3.16, evaluated on the xz-plane at $y = 0$ in Figs. 3.16 (a-c), on the yz-plane at $x = 0$ in Figs. 3.16 (d-f) and on the xy-plane at $z = 0$ in Figs. 3.16 (g-i). The numerical results closely match the analytical solution in both phase and amplitude. In Figs. 3.16(a), (e), and (h), near-zero oscillations are observed inside the cylindrical region, where no acoustic propagation is expected.

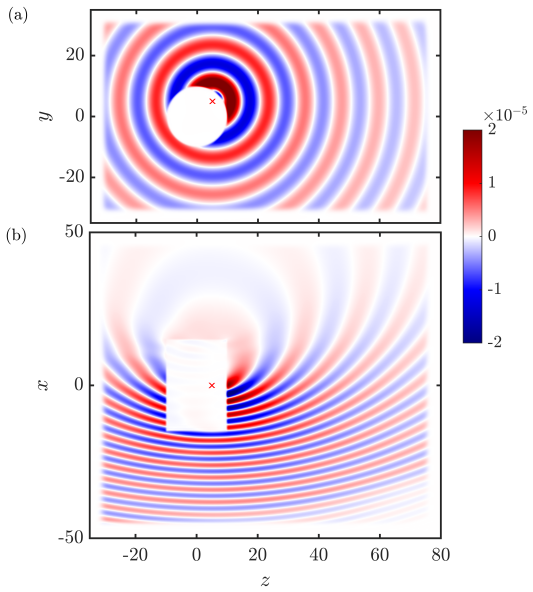

Figure 3.15: Pressure field generated by a three-dimensional monopole immersed in a uniform flow with Mach number $M = 0.8$ at $t = 200$ s on (a) the yz-plane at $x = 0$ and (b) the xz-plane at $y = 0$. The monopole, indicated by the red cross, is located at $(x_m, y_m, z_m) = (0, 5, 5)$ within a cylindrical control surface centered at the origin with radius $R_s = 10$.

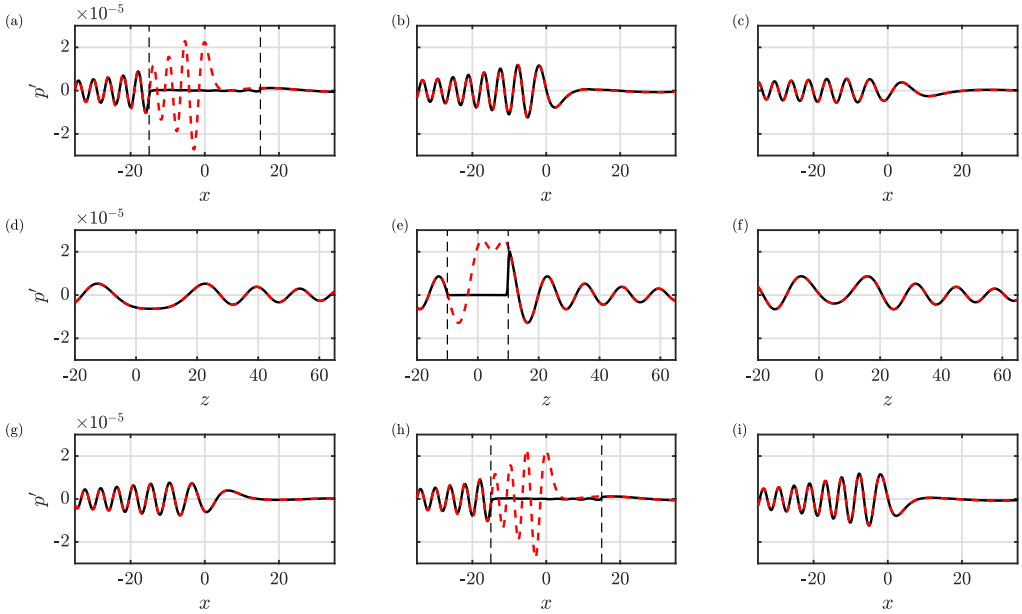

Figure 3.16: Comparison between the analytical solution (dashed red line) and the numerical solution (solid black line) in the xz-plane at $y = 0$ for (a) $z = 0$, (b) $z = 20$, (c) $z = 40$, in the yz-plane at $x = 0$ for (d) $y = -20$, (e) $y = 0$, (f) $y = 20$, and in the xy-plane at $z = 0$ for (g) $y = -20$, (h) $y = 0$, (i) $y = 20$. The black vertical dashed lines denotes the boundaries of the surface.

3.5 Conclusion

The method proposed in this chapter enables the injection of acoustic waves through volumetric source terms distributed along an arbitrary control surface. This non-linear formulation is rigorously derived from fluid mechanics equations to keep them very general. Validation has been carried out for oblique plane waves on a Cartesian grid and for a monopole source in both two and three dimensions under uniform flow and with a cylindrical volume control on a Cartesian mesh. In all cases, the results showed excellent agreement by comparison with corresponding analytical solutions.

The source terms are immersed in the computational mesh, avoiding the need to conform the mesh to the control surface geometry. Mesh refinement near the control surface may be required to properly take into account its shape. It is also recommended the use of compact sources by selecting a Gaussian half-width equal to the mesh spacing. Future work could investigate the numerical error obtained using a uniform Cartesian mesh compared with that from a mesh conforming to the geometry of the control surface.

Building on these findings, the proposed method offers several notable advantages. It can be directly applied on a uniform Cartesian mesh, regardless of the chosen control surface, which greatly simplifies implementation in finite-difference solvers. Because the control surface is fully immersed within the computational domain, no boundary conditions need to be imposed and no mesh adaptation to the surface geometry is required. Unlike characteristic-based wave-injection techniques, the present approach does not require the evaluation of additional terms: only volumetric source terms are added within the Runge–Kutta loop, leaving the computational cost essentially unchanged. Care must be taken to ensure an adequate level of source compactness relative to the mesh resolution, but this requirement is straightforward to satisfy. Overall, the method provides a robust and efficient alternative for CFD/CAA coupling, being also capable of capturing non-linear propagation effects.

The methodology and results presented in this chapter have been published in the Journal of the Acoustical Society of America [43].

4 Reflection Method

This chapter presents an original method for simulating the reflection of acoustic waves from a physical obstacle. The approach employs volumetric source terms in the momentum conservation equations to achieve full reflection of incident acoustic waves. These sources are placed on the obstacle surface. Several academic test cases are provided to demonstrate the method's effectiveness, along with a spatial convergence analysis. The results show second-order accuracy when the mesh conforms to the obstacle geometry, and first-order accuracy when the obstacle is immersed within the mesh.

4.1 State of the art

Accurate simulation of acoustic wave reflection and scattering around complex physical obstacles is crucial in computational aeroacoustics. High-fidelity numerical schemes must manage complex boundaries without introducing artificial effects. Various methods exist to address the challenges posed by irregular geometric features, particularly when using Cartesian computational grids. The following paragraphs provide a brief overview of existing methods used to simulate physical obstacles within a computational domain, emphasizing their main advantages as well as their limitations and implementation challenges.

4.1.1 Immersed Boundary Methods

Immersed Boundary Methods (IBMs) are crucial computational techniques for solving systems of partial differential equations on meshes that do not conform to physical boundaries. IBMs leverage the simplicity and efficiency of structured Cartesian meshes, which is advantageous for complex geometric configurations. While these methods became widely adopted in fluid mechanics after the start of the new millennium, predecessors were conceived as early as the 1960s.

The core strategy of any IBM implementation involves three steps: identifying boundary nodes, enforcing boundary conditions, and reconstructing variables near the interface. Enforcing

boundary conditions is typically achieved by adding a volumetric forcing term to the governing equations, such as the Navier–Stokes momentum equation. This approach avoids the issues inherent in body-fitted grids, such as non-orthogonality and significant per-cell overhead.

Diffused-Interface Immersed Boundary Methods

This foundational class of IBMs, pioneered by Peskin [44] in 1972, relies on a network of Lagrangian markers distributed over the immersed boundary. The method applies a total forcing at each Lagrangian marker, representing the reaction on the flow. Instead of using sharp Dirac delta functions, which localize the force but can lead to numerical instabilities, smoother distribution functions are used to spread the force over surrounding Eulerian grid points. This technique is inherently suited for Fluid–Structure Interaction (FSI) problems, particularly in biological fluid dynamics. However, the choice and expression of the regularized delta functions are crucial for solution smoothness and conservation properties. A more general discussion about this topic is given by Griffith and Patankar [45].

Feedback Forcing Methods

Feedback methods dynamically adjust the forcing term based on the error between the simulated velocity u and the desired boundary velocity u_b. The forcing term is typically calculated as a function of the velocity difference, using a Proportional Integral Derivative (PID) control approach. Goldstein *et al.* [46] and Saiki and Biringen [47] demonstrated this technique, where the forcing term depends on two negative user-defined parameters, α and β. Their function is to dynamically drive the velocity u towards the imposed velocity u_b. Penalization methods (Angot *et al.* [48], Speckil *et al.* [49]) are a specific sub-case of the feedback approach, treating the immersed body as a volume of porous material. In this formulation, the forcing term becomes $f = (u - u_b)/K$, where K is the solidity parameter, akin to a feedback control where $\alpha = 0$ and $\beta = 1/K$. However, the results are unavoidably affected by the choice of these parameters, which are non-objective quantities. Increasing the magnitude of α and β to minimize the difference $|u - u_b|$, stiffens the governing equation, complicating its integration.

Implicit and Projection Methods

These methods seek to determine the forcing implicitly, avoiding the need for arbitrary user-defined parameters characteristic of feedback schemes. Mohd-Yusof [50] proposed solving the time-discrete momentum equation for the forcing term after substituting the interface velocity at the next time step with the desired velocity u_b. This approach does not require ad hoc parameters and maintains the time stability of the numerical integration. Fadlun *et al.* [51] confirmed that this method retains second-order accuracy.

Taira and Colonius [52] introduced an advanced method where both the pressure and the boundary body force are treated as distributed Lagrange multipliers. This scheme is algebraically

similar to a fractional step method but is capable of simultaneously satisfying velocity boundary conditions and ensuring local mass conservation.

Ghost Point Method

A well-known technique is based on the boundary reconstruction to determine flow variables at interface nodes based on surrounding fluid nodes. Rich and Blackman [53] defined "fictitious mesh cells" (ghost cells) inside the body to enforce boundary conditions. Viecelli [54, 55] detailed the necessary procedures for classifying cells and interpolating Eulerian velocities at a material point on the boundary. A specific boundary treatment was then developed by Kurbatskii and Tam [56] for high-order finite difference schemes on Cartesian grids. The difficulty of enforcing wall boundary conditions is overcome by introducing ghost values of pressure at mesh points adjacent to the solid boundary inside the object. This approach avoids the artificial inhomogeneities inherent in body-fitted and unstructured grids. The ghost values are chosen such that the discretized wall boundary condition ($\mathbf{V} \cdot \mathbf{n} = 0$ or $\partial p/\partial n = 0$) is satisfied. The resulting method is accurate even for objects with sharp edges and requires no extra physical boundary conditions beyond the original partial differential equations.
However, implementing this method involves significant programming complexities to identify ghost point types and calculate coupled ghost values, particularly for curved surfaces. Furthermore, when high accuracy is required, complex interpolating functions necessitate a large number of fluid nodes, which extends the spatial support of the interpolation stencil. The geometry is also approximated by straight line segments, which may generate spurious numerical waves, necessitating the use of artificial selective damping techniques, especially in the boundary region, to maintain numerical stability [56].

Limitations for High-Fidelity Simulations

While IBMs excel in managing complex geometries, they face inherent limitations, particularly in resolving thin boundary layers crucial for high-fidelity simulations [57]. Unlike body-fitted meshes, which can be refined anisotropically in the wall-normal direction, IBMs operate on fixed Cartesian grids. Since any direction can be normal or tangential to the immersed boundary, the mesh cannot benefit from near-wall clustering. Consequently, the grid spacing must be fine in all directions, scaling with the viscous unit. The computational load for IBMs scales unfavorably, increasing roughly as compared to for body-fitted meshes. This unfavorable scaling makes IBMs eventually unsuitable for high–Reynolds number flows unless additional wall modeling is employed. In highly turbulent flows, abrupt discontinuities in grid spacing, which can occur with local grid refinement patches, produce spurious numerical stresses and contamination of the flow field, requiring careful numerical scheme selection.

4.1.2 Impedance Mismatch Method

The Impedance Mismatch Method (IMM) [58, 59] is a technique initially developed for high-order finite difference schemes on Cartesian grids. It simulates a rigid obstacle by replacing it with a fluid region having a vastly different acoustic impedance, typically achieved through a high density value. This method avoids the difficulties associated with mapping physical planes to computational planes in body-fitted grids, which can introduce artificial wave scattering. The IMM is highly efficient, as computational time remains unchanged by the presence of a solid object. However, naive application of the IMM can lead to numerical instabilities. The method requires the formulation of an auxiliary problem using continuous dependent variables that implicitly include the matching of discontinuities present in the physical problem. Furthermore, the method produces discontinuities in the derivatives of the acoustic fluctuations at the interface. This requires the jump in density to be replaced by a smoothing function to reduce high wave-number disturbances. Small errors in amplitude and phase can still arise due to the finite choice of the density ratio.

4.1.3 Equivalent Source Method

The Equivalent Source Method (ESM) [60, 61] solves exterior acoustic scattering problems using equivalent sources embedded within the scattering body. The strength of these sources is calculated to satisfy the boundary conditions at collocation points on the obstacle surface. ESM is a meshless approach, which simplifies numerical implementation and avoids the numerical singularity and non-uniqueness problems encountered in the Boundary Element Method (BEM). For large problems, ESM offers faster computation because the number of equivalent sources can be significantly less than the surface wall points, reducing the matrix size. ESM provides accurate predictions, even in diffracted or shadow zones. The time-domain ESM is specifically advantageous for broadband noise and transient events. Sound power calculation provides a tool to check energy conservation and assess prediction accuracy. The primary challenge is the lack of rigorous, analytic methods for determining the optimal number and position of the equivalent sources. The solution accuracy is highly sensitive to the choice of parameters, including the number of equivalent sources, their positions, the time step, and the cutoff singular value. ESM frequently encounters numerical instability linked to the ill-conditioned nature of the influence matrix. Regularization techniques, such as Singular Value Decomposition (SVD) and time-averaging algorithms, are necessary to achieve stable solutions.

4.1.4 Curvilinear Body-Fitted Grids

This traditional approach involves using computational meshes that conform to the shape of the physical obstacle. This technique is common in Computational Fluid Dynamics and Computational Aeroacoustics [24]. For objects with complex or multiple surfaces, multiple

overset curvilinear body-fitted grids (Chimera techniques) can be employed [62]. Curvilinear grids allow for straightforward implementation of wall boundary conditions. They enable high-fidelity simulations around non-Cartesian bodies. High-order explicit and implicit schemes can be successfully applied to these grids to meet low dispersion and dissipation requirements. The necessary coordinate transformation introduces variable coefficients into the governing equations, effectively simulating wave propagation through an inhomogeneous medium. However, generating structured body-fitted meshes is complicated and computationally costly for intricate geometries. Furthermore, communication between overset grids requires accurate, high-order interpolation schemes [62].

4.1.5 Impedance and Transmittance Boundary Condition

An original method based on impedance and transmittance relationships in the frequency domain was recently developed by Bilbao [63] for room acoustics applications, and it can be extended to other contexts as well.

The methodology introduces a formulation based on dual driving terms applied pointwise at boundary locations to the separate mass and momentum conservation equations. This represents a key distinction from conventional IBM approaches presented in Subsection 4.1.1, which typically employ a single pressure-based driving term. In the present acoustic context, however, dual terms are required to model impedance boundary conditions accurately. These terms can be directly tuned to match prescribed boundary impedance and transmittance for the wall.

The development of the method begins with the linearized Euler equations for mass and momentum conservation:

$$\frac{1}{\rho c^2}\frac{\partial p}{\partial t} + \frac{\partial u}{\partial x} = 0, \quad \rho\frac{\partial u}{\partial t} + \frac{\partial p}{\partial x} = 0 \tag{4.1}$$

These equations are then reformulated in terms of traveling waves $a(x,t)$ and $b(x,t)$, defined as:

$$a = p + Z_0 u, \quad b = p - Z_0 u \tag{4.2}$$

where Z_0 and Y_0 are the characteristic impedance and admittance of air, respectively, given by:

$$Z_0 = \rho c, \quad Y_0 = 1/Z_0 = 1/\rho c \tag{4.3}$$

Using these definitions, an equivalent system of equations can be expressed in terms of the newly introduced waves a and b:

$$\frac{\partial a}{\partial t} + c\frac{\partial a}{\partial x} = 0, \quad \frac{\partial b}{\partial t} - c\frac{\partial b}{\partial x} = 0 \tag{4.4}$$

a and b thus describe waves propagating rightward and leftward, respectively, as shown in Fig. 4.1(a).

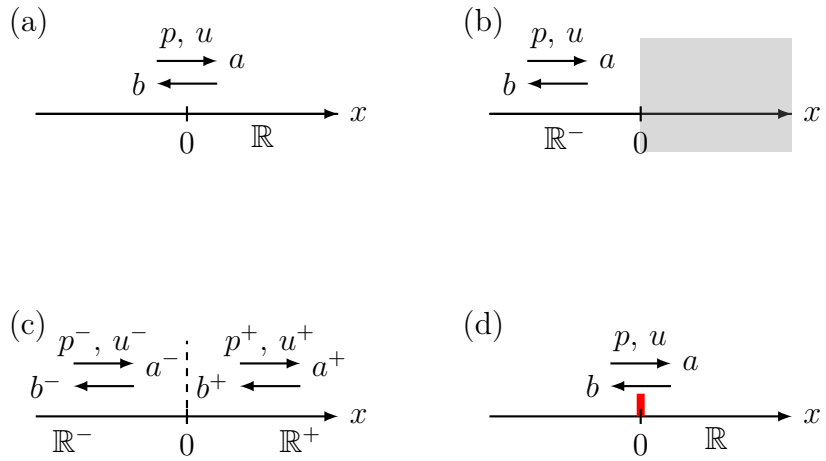

Figure 4.1: One-dimensional domains. (a) Unbounded domain $\mathbb{R}$. (b) Half-space $\mathbb{R}^-$. (c) Barrier separating the two half-spaces $\mathbb{R}^-$ and $\mathbb{R}^+$. (d) Unbounded domain $\mathbb{R}$ with an immersed boundary acting as a forcing term. [63]

An acoustic barrier is now considered. The wall behavior is specified in the frequency domain, in terms of impedance and admittance, using the Laplace transform to relate pressure and velocity:

$$\hat{p}(s) = Z_0 z(s)\hat{u}(s) \quad \text{or} \quad \hat{u}(s) = Y_0 y(s)\hat{p}(s) \tag{4.5}$$

where $\hat{p}(s)$ and $\hat{u}(s)$ are the Laplace transformed quantities for pressure and velocity, respectively, and $z(s)$ and $y(s)$ are dimensionless coefficients for impedance and admittance, respectively.

Half-space with an impedance boundary condition

Now one considers the negative half-space $\mathbb{R}^- = (-\infty, 0]$, as illustrated in Fig. 4.1(b). A boundary condition must be applied at $x = 0$, relating p and u. By prescribing an impedance condition as defined in Eq. (4.5), this condition can be expressed in terms of a and b:

$$\hat{b}(0, s) = \frac{z(s) - 1}{z(s) + 1}\hat{a}(0, s) \tag{4.6}$$

where the reflectance $\mathcal{R}(s)$ can be defined as

$$\mathcal{R}(s) = \frac{z(s) - 1}{z(s) + 1} \leq 1 \quad \text{if} \quad z(s) \in \mathbb{R}^+ \tag{4.7}$$

Using Laplace transform analysis, the solution to the problem can be obtained. Wave $\hat{a}$ retains the same form as in free space, whereas wave $\hat{b}$ includes an additional term relative to the free-space solution, accounting for the reflectance $\mathcal{R}$.

Two-sided barrier and transmission

The one-dimensional domain is now divided into two subdomains $\mathbb{R}^- = (-\infty, 0]$ and $\mathbb{R}^+ = [0, \infty)$, as shown in Fig. 4.1(c). An acoustic barrier is placed at $x = 0$. The Euler equations can be written for both regions as:

$$\frac{1}{\rho c^2}\frac{\partial p^\pm}{\partial t} + \frac{\partial u^\pm}{\partial x} = 0, \quad \rho\frac{\partial u^\pm}{\partial t} + \frac{\partial p^\pm}{\partial x} = 0 \tag{4.8}$$

A discontinuous jump in pressure and velocity is defined at the interface at $x = 0$:

$$p_\Delta(t) = p^-(0,t) - p^+(0,t), \quad u_\Delta(t) = u^-(0,t) - u^+(0,t) \tag{4.9}$$

Furthermore, the average pressure and velocity $\bar{p}(t)$ and $\bar{u}(t)$ are defined as:

$$\bar{p}(t) = \frac{p^-(0,t) + p^+(0,t)}{2}, \quad \bar{u}(t) = \frac{u^-(0,t) + u^+(0,t)}{2} \tag{4.10}$$

Once again, two impedance relations are written for pressure and velocity to describe the dynamics of the acoustic barrier:

$$\hat{p}_\Delta(s) = 2Z_0 z_u(s)\hat{\bar{u}}(s), \quad \hat{u}_\Delta(s) = 2Y_0 y_p(s)\hat{\bar{p}}(s) \tag{4.11}$$

where $z_u(s)$ and $y_p(s)$ are a nondimensional impedance and admittance, respectively.
The Euler equations can be rewritten in terms of traveling waves $a^\pm$ and $b^\pm$ as already done above:

$$\frac{\partial a^\pm}{\partial t} + c\frac{\partial a^\pm}{\partial x} = 0, \quad \frac{\partial b^\pm}{\partial t} - c\frac{\partial b^\pm}{\partial x} = 0 \tag{4.12}$$

The solution can be expressed in the Laplace domain as a function of $\hat{a}^\pm$ and $\hat{b}^\pm$. The impedance conditions given in Eq. (4.11) at $x = 0$ can be rewritten in terms of the four waves:

$$\begin{pmatrix} \hat{b}^-(0,s) \\ \hat{a}^+(0,s) \end{pmatrix} = \begin{pmatrix} \mathcal{R} & \mathcal{T} \\ \mathcal{T} & \mathcal{R} \end{pmatrix} \begin{pmatrix} \hat{a}^-(0,s) \\ \hat{b}^+(0,s) \end{pmatrix} \tag{4.13}$$

where $\mathcal{R}$ and $\mathcal{T}$ are the reflection and transmission coefficients, respectively, defined as:

$$\mathcal{R} = \frac{1}{2}\left(\frac{1-y_p}{1+y_p} + \frac{z_v - 1}{z_v + 1}\right), \quad \mathcal{T} = \frac{1}{2}\left(\frac{1-y_p}{1+y_p} - \frac{z_v - 1}{z_v + 1}\right) \tag{4.14}$$

This system allows the reflection and transmission of waves across the interface at $x = 0$. The coefficients $\mathcal{R}$ and $\mathcal{T}$ can thus be defined to characterize the acoustic barrier dynamics.

Immersed Boundary

A one-dimensional domain with source terms applied at $x = 0$ is now considered, as illustrated in Fig. 4.1(d). In this configuration, the Euler equations take the following form:

$$\frac{1}{\rho c^2}\frac{\partial p}{\partial t} + \frac{\partial u}{\partial x} = -u_\Delta \delta(x), \quad \rho\frac{\partial u}{\partial t} + \frac{\partial p}{\partial x} = -p_\Delta \delta(x) \tag{4.15}$$

where $\delta(x)$ is the Dirac delta function and $p_\Delta(t)$ and $u_\Delta(t)$ are driving functions representing pressure and velocity, respectively. These functions are directly related to the computed acoustic field, since they depend on $\bar{p}(t)$ and $\bar{u}(t)$ defined as:

$$\bar{p} = \int_{-\infty}^{\infty} p(\xi, t)\delta(\xi)\,\mathrm{d}\xi, \quad \bar{u} = \int_{-\infty}^{\infty} u(\xi, t)\delta(\xi)\,\mathrm{d}\xi \tag{4.16}$$

The immittance relationships are thus defined in the Laplace-transformed domain:

$$\hat{p}_\Delta(s) = 2Z_0 z_u(s)\hat{\bar{u}}(s), \quad \hat{u}_\Delta(s) = 2Y_0 y_p(s)\hat{\bar{p}}(s) \tag{4.17}$$

The problem is then reformulated in terms of the waves a and b, which propagate to the right and left, respectively. The solution is obtained by following the same procedure described above. By examining the $\mathbb{R}^-$ and $\mathbb{R}^+$ domains separately, it is found that the solution obtained with the immersed boundary formulation is consistent with the results presented earlier for the "Two-sided barrier and transmission" case.

The main advantage of this immersed boundary approach, combined with appropriately defined source terms, is that it enables obstacles to be modeled without partitioning the domain into two separate regions. This feature is particularly valuable in three-dimensional configurations [64, 65], where complex barrier geometries would otherwise require a mesh adapted to the boundary shape. The present method also enables the direct specification of the desired reflection and transmission coefficients for the barrier, owing to its frequency-domain formulation. However, the source term definition in Eq. (4.16) may be computationally restrictive, as the integrals must be evaluated at every iteration. For large computational domains, this requirement can significantly increase the overall simulation time.

4.2 General formulation

This section presents an original method for simulating an obstacle within the computational domain using volumetric source terms. These terms are applied along the obstacle boundaries and are defined based on the wall pressure recorded at each iteration.

Consider a domain containing one or more sources and solid obstacles. A scalar function $f(\mathbf{x})$ is defined such that $f > 0$ in the fluid region outside the obstacles and $f < 0$ inside the obstacles. The obstacle surfaces are described by points $\mathbf{x}_s$ satisfying $f(\mathbf{x}_s) = 0$. The function f is normalized so that the surface normal vector $\mathbf{n} = \nabla f$ has unit magnitude. On the obstacle surfaces, the impermeability condition $\mathbf{u} \cdot \mathbf{n} = 0$ is imposed. An example of a one-dimensional domain is illustrated in the schematic shown in Fig. 4.2.

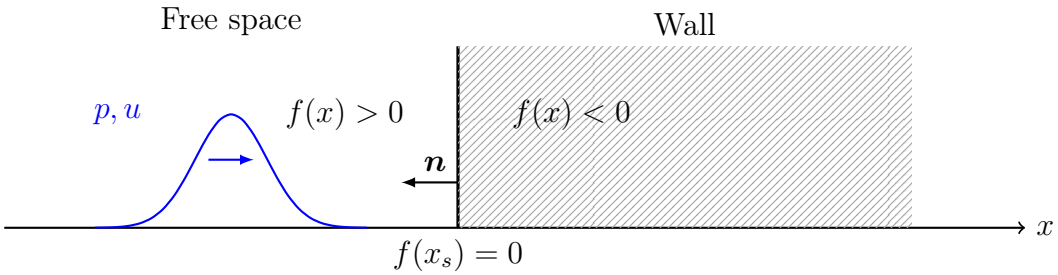

Figure 4.2: Schematic of an acoustic pulse in blue propagating towards a rigid wall defined by $f(x_s) = 0$.

A Heaviside function H is also introduced as

$$H(x) = \begin{cases} 1 & \text{if } x > 0, \\ 1/2 & \text{if } x = 0, \\ 0 & \text{if } x < 0. \end{cases} \tag{4.18}$$

The choice of the value at $x = 0$ is justified later.
The mass conservation equation is given by

$$\frac{\partial \rho}{\partial t} + \frac{\partial}{\partial x_i}(\rho u_i) = 0, \tag{4.19}$$

which is rewritten in terms of fluctuations $\rho' = \rho - \rho_0$ and $(\rho\mathbf{u})' = \rho\mathbf{u} - \rho_0\mathbf{u}_0$ as

$$\frac{\partial \rho'}{\partial t} + \frac{\partial}{\partial x_i}(\rho u_i)' = 0. \tag{4.20}$$

Multiplying Eq. (4.20) by $H[f(\mathbf{x})]$ yields

$$\frac{\partial}{\partial t}(\rho' H) + \frac{\partial}{\partial x_i}[(\rho u_i)' H] = (\rho u_i)' n_i \delta(f). \tag{4.21}$$

The following notations are introduced: $\overline{\rho}' = \rho' H$ and $\overline{\rho\mathbf{u}}' = (\rho\mathbf{u})' H$. To obtain an equation involving only $\overline{\rho}'$ and $\overline{\rho\mathbf{u}}'$, it is noted that $\overline{\rho\mathbf{u}}' = (\rho\mathbf{u})'/2$ on $\mathbf{x}_s$, which leads to

$$\frac{\partial \overline{\rho}'}{\partial t} + \frac{\partial}{\partial x_i}(\overline{\rho u_i})' = 2(\overline{\rho u_i})' n_i \delta(f). \tag{4.22}$$

Using the same approach, the equations for momentum and energy conservation are obtained as

$$\frac{\partial}{\partial t}\left(\overline{\rho u_i}\right)' + \frac{\partial}{\partial x_j}\left(\overline{\rho u_i u_j}\right)' + \frac{\partial}{\partial x_i}\overline{p}' = 2[\left(\overline{\rho u_i u_j}\right)' n_j + \overline{p}' n_i]\,\delta(f) \tag{4.23}$$

$$\frac{\partial}{\partial t}\left(\overline{\rho e_t}'\right) + \frac{\partial}{\partial x_i}\left[(\overline{\rho e_t u_i})' + (\overline{p u_i})'\right] = 2[(\overline{\rho e_t u_i})' + (\overline{p u_i})']n_i\,\delta(f) \tag{4.24}$$

Finally, by enforcing the impermeability condition ($\mathbf{u}_0 \cdot \mathbf{n} = 0$ and $\mathbf{u}' \cdot \mathbf{n} = 0$), the governing

equations reduce to

$$\frac{\partial \overline{\rho}'}{\partial t} + \frac{\partial}{\partial x_i}(\overline{\rho u_i})' = 0. \tag{4.25}$$

$$\frac{\partial}{\partial t}(\overline{\rho u_i})' + \frac{\partial}{\partial x_j}\left(\overline{\rho u_i u_j}\right)' + \frac{\partial}{\partial x_i}\overline{p}' = 2\overline{p}' n_i\, \delta(f) \tag{4.26}$$

$$\frac{\partial}{\partial t}\left(\overline{\rho e_t}'\right) + \frac{\partial}{\partial x_i}\left[(\overline{\rho e_t u_i})' + (\overline{p u_i})'\right] = 0 \tag{4.27}$$

These equations are satisfied by variables defined over the entire computational domain.
To approximate the Dirac delta function, a Gaussian function is employed:

$$\delta(x) \approx \delta_b(x) = \frac{1}{\sqrt{\pi} b} \exp\left(-\frac{x^2}{b^2}\right). \tag{4.28}$$

By integration, the corresponding Heaviside function is obtained as

$$H_b(x) = \frac{1}{2}\left[1 + \operatorname{erf}\left(\frac{x}{b}\right)\right], \tag{4.29}$$

where erf denotes the error function. The function $H_b(x)$ converges pointwise to $H(x)$ as $b \to 0$. In particular, $H_b(0) = 1/2$ for any value of b.

4.3 Results

This section presents the results obtained by applying the reflection method to three analytical cases and three numerical benchmark cases.
The analytical cases comprise a characteristic-based formulation, and two integral formulations incorporating a Dirac delta function and a Gaussian distribution applied to the source terms. These cases are included to facilitate a comprehensive understanding of the proposed method and to verify its validity across different mathematical formulations.
The numerical cases comprise the reflection of a one-dimensional acoustic pulse, the reflection of a two-dimensional pulse from a wall in a uniform flow, and the diffraction of a two-dimensional pulse by a cylinder. All simulations are conducted with a Courant–Friedrichs–Lewy number of 0.5, and all quantities are dimensionless, assuming an ambient pressure $p_0 = 1$, an ambient density $\rho_0 = 1.4$, and speed of sound $c_0 = \sqrt{\gamma p_0/\rho_0} = 1$. Perfectly Matched Layers [8] are applied to the outer 30 grid points at the domain boundaries in both the one- and two-dimensional cases.

4.3.1 Characteristics Formulation

The linearized one-dimensional Euler equations are written with generic source terms:

$$\frac{\partial p}{\partial t} + \frac{\partial v}{\partial x} = 2Bv\delta(x) \tag{4.30}$$
$$\frac{\partial v}{\partial t} + \frac{\partial p}{\partial x} = 2Ap\delta(x) \tag{4.31}$$

where A and B are two coefficients applied to the source terms. In this test case, their values are determined such that a perfectly reflecting boundary condition is achieved at $x = 0$.
The characteristic waves are defined as $a = (p+v)/2$ and $b = (p-v)/2$. They satisfy the following advection equations:

$$\frac{\partial a}{\partial t} + \frac{\partial a}{\partial x} = Ap\delta(x) + Bv\delta(x) = 2Ia\delta(x) + 2Jb\delta(x) \tag{4.32}$$
$$\frac{\partial b}{\partial t} - \frac{\partial b}{\partial x} = -Ap\delta(x) + Bv\delta(x) = -2Ja\delta(x) - 2Ib\delta(x) \tag{4.33}$$

with the parameters:

$$I = \frac{A+B}{2}, \qquad J = \frac{A-B}{2} \tag{4.34}$$

A plane incident wave $a(x < 0, t) = \exp(\mathrm{i}kx)\exp(-\mathrm{i}\omega t)$ is considered. The transmitted wave is expressed as $a(x > 0, t) = T\exp(\mathrm{i}kx)\exp(-\mathrm{i}\omega t)$, and the reflected wave as $b(x < 0, t) = R\exp(-\mathrm{i}kx)\exp(-\mathrm{i}\omega t)$. The transmission and reflection conditions at $x = 0$ are then derived from Eqs. (4.32) and (4.33):

$$a(0^+, t) - a(0^-, t) = I(a(0^+, t) + a(0^-, t)) + J(b(0^+, t) + b(0^-, t)) \tag{4.35}$$
$$-(b(0^+, t) - b(0^-, t)) = -J(a(0^+, t) + a(0^-, t)) - I(b(0^+, t) + b(0^-, t)) \tag{4.36}$$

that gives:

$$T - 1 = I(T + 1) + JR \tag{4.37}$$
$$R = -J(T + 1) - IR \tag{4.38}$$

The equations above can be reformulated as

$$T(1 - I) = 1 + I + RJ \tag{4.39}$$
$$R(1 + I) = -J - TJ \tag{4.40}$$

Finally, one obtains:

$$T = \frac{1 + 2I + I^2 - J^2}{1 - I^2 - J^2} = \frac{1 + A + B + AB}{1 - AB} \tag{4.41}$$

$$R = \frac{-2J}{1 - I^2 - J^2} = \frac{B - A}{1 - AB} \tag{4.42}$$

The reflection and transmission coefficients are thus expressed as functions of the source term coefficients in the characteristics equations. To model a perfectly rigid, non-porous wall, the coefficients are then set to $R = 1$ and $T = 0$. By using Eqs. (4.39) and (4.40), one obtains:

$$I + J = -1 \tag{4.43}$$

which gives $A = -1$ and $B = 0$, ensuring total reflection with no transmission.

4.3.2 Integral Formulation

An integral formulation of the method is now presented. In this case, the convention $\exp(-\mathrm{i}\omega t)$ is adopted for wave propagation according to Euler's formula. The governing equations are expressed as follows:

$$-\mathrm{i}\omega p + \frac{\mathrm{d}v}{\mathrm{d}x} = \delta(x - x_s) \tag{4.44}$$

$$-\mathrm{i}\omega v + \frac{\mathrm{d}p}{\mathrm{d}x} = \delta(x - x_s) + Ap(0)\delta(x) \tag{4.45}$$

with x_s the source position. As in the previous case, the coefficient A is determined to enforce perfect reflection, thereby preventing wave transmission into the obstacle.
A spatial Fourier transform is now applied:

$$\hat{p}(k) = \int_{-\infty}^{+\infty} p(x)\,\mathrm{e}^{-\mathrm{i}kx}\,\mathrm{d}x \qquad \hat{v}(k) = \int_{-\infty}^{+\infty} v(x)\,\mathrm{e}^{-\mathrm{i}kx}\,\mathrm{d}x \tag{4.46}$$

This gives:

$$-\mathrm{i}\omega\hat{p} + \mathrm{i}k\hat{v} = \mathrm{e}^{-\mathrm{i}kx_s} \tag{4.47}$$

$$-\mathrm{i}\omega\hat{v} + \mathrm{i}k\hat{p} = \mathrm{e}^{-\mathrm{i}kx_s} + Ap(0) \tag{4.48}$$

Equation (4.48) is now multiplied by $\mathrm{i}k$, that reads:

$$-\mathrm{i}\omega\mathrm{i}k\hat{v} + (\mathrm{i}k)^2\hat{p} = \mathrm{i}k\,\mathrm{e}^{-\mathrm{i}kx_s} + A\mathrm{i}kp(0) \tag{4.49}$$

Equations (4.47) and (4.49) are then combined:

$$-\mathrm{i}\omega\mathrm{e}^{-\mathrm{i}kx_s} - (\mathrm{i}\omega)^2\hat{p} + (\mathrm{i}k)^2\hat{p} = \mathrm{i}k\,\mathrm{e}^{-\mathrm{i}kx_s} + A\mathrm{i}kp(0), \tag{4.50}$$

The expression above is reformulated:

$$[(\mathrm{i}k)^2 - (\mathrm{i}\omega)^2]\hat{p} = (\mathrm{i}k + \mathrm{i}\omega)\,\mathrm{e}^{-\mathrm{i}kx_s} + A\mathrm{i}kp(0). \tag{4.51}$$

This gives:

$$\begin{aligned}\hat{p} &= \frac{\mathrm{i}k + \mathrm{i}\omega}{(\mathrm{i}k)^2 - (\mathrm{i}\omega)^2}\,\mathrm{e}^{-\mathrm{i}kx_s} + A\frac{\mathrm{i}k}{(\mathrm{i}k)^2 - (\mathrm{i}\omega)^2}p(0) \\ &= \frac{1}{\mathrm{i}k - \mathrm{i}\omega}\,\mathrm{e}^{-\mathrm{i}kx_s} + \frac{A}{2}\left(\frac{1}{\mathrm{i}k - \mathrm{i}\omega} + \frac{1}{\mathrm{i}k + \mathrm{i}\omega}\right)p(0)\end{aligned} \tag{4.52}$$

The first term of Eq. (4.52) is now considered:

$$p_1 = \frac{1}{2\pi}\int_{-\infty}^{+\infty} \frac{1}{\mathrm{i}k - \mathrm{i}\omega}\,\mathrm{e}^{-\mathrm{i}kx_s}\,\mathrm{e}^{\mathrm{i}kx}\,\mathrm{d}k. \tag{4.53}$$

To introduce dissipation, ω is replaced by $\omega + \mathrm{i}\epsilon$, with $\epsilon > 0$, such that the amplitude of a right-propagating wave decreases as x increases, and that of a left-propagating wave decreases as x decreases. This yields:

$$p_1 = -\frac{\mathrm{i}}{2\pi}\int_{-\infty}^{+\infty} \frac{1}{k - \omega - \mathrm{i}\epsilon}\,\mathrm{e}^{\mathrm{i}k(x-x_s)}\,\mathrm{d}k. \tag{4.54}$$

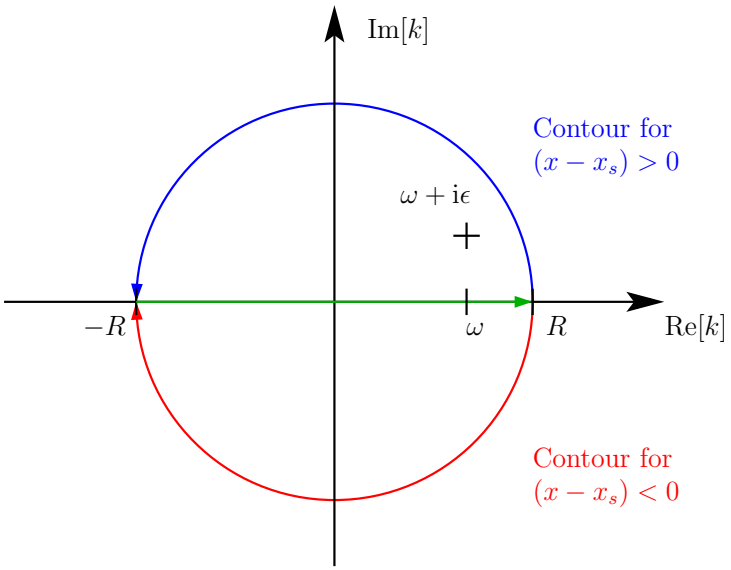

Figure 4.3: Integration path used to evaluate Eq. (4.54)

The integrand then exhibits a pole at $k_p = \omega + \mathrm{i}\epsilon$. The calculation follows from applying Jordan's lemma. For $x - x_s > 0$, the integration contour is closed with a semicircle centered at the origin in the upper half-plane, while for $x - x_s < 0$, the semicircle lies in the lower half-plane. The contributions along both semicircles are null. When $x - x_s > 0$, only the contribution from the pole at k_p remains. When $x - x_s < 0$, the integral is zero. The integration path along the two semicircular contours is illustrated in Fig. 4.3. Taking the limit as $\epsilon \to 0$, one obtains:

$$p_1 = \mathrm{e}^{\mathrm{i}\omega(x-x_s)} H(x - x_s). \tag{4.55}$$

The same strategy is applied to:

$$p_2 = \frac{1}{2\pi} \int_{-\infty}^{+\infty} \frac{A}{2} \left(\frac{1}{\mathrm{i}k - \mathrm{i}\omega} + \frac{1}{\mathrm{i}k + \mathrm{i}\omega} \right) p(0) \mathrm{e}^{\mathrm{i}kx} \, \mathrm{d}k \tag{4.56}$$

This finally gives:

$$p = \mathrm{e}^{\mathrm{i}\omega(x-x_s)} H(x - x_s) + \frac{A}{2} p(0) (\mathrm{e}^{\mathrm{i}\omega x} H(x) - \mathrm{e}^{-\mathrm{i}\omega x} H(-x)). \tag{4.57}$$

- For $x_s > 0$, $p(0) = 0$, and the solution is $p = \mathrm{e}^{\mathrm{i}\omega(x-x_s)} H(x - x_s)$, regardless of the value of A. Consequently, only a wave propagating in the positive x-direction is present, and the source term does not influence the solution.

- For $x_s < 0$, $p(0) = \mathrm{e}^{-\mathrm{i}\omega x_s}$, which gives:

$$p = \mathrm{e}^{\mathrm{i}\omega(x-x_s)} H(x - x_s) + \frac{A}{2} \left(\mathrm{e}^{\mathrm{i}\omega(x-x_s)} H(x) - \mathrm{e}^{-\mathrm{i}\omega(x+x_s)} H(-x) \right). \tag{4.58}$$

  With $A = -2$, one obtains:

$$p = \mathrm{e}^{\mathrm{i}\omega(x-x_s)} [H(x - x_s) - H(x)] + \mathrm{e}^{-\mathrm{i}\omega(x+x_s)} H(-x). \tag{4.59}$$

  The signal cancels for $x > 0$, and a reflected wave is generated for $x < 0$ with the same amplitude as the incident wave.

For the acoustic velocity v, this can be calculated from Eq. (4.45):

$$-\mathrm{i}\omega v = -\frac{\mathrm{d}p}{\mathrm{d}x} + \delta(x - x_s) - 2\mathrm{e}^{-\mathrm{i}\omega x_s} \delta(x) \tag{4.60}$$

This yields:

$$\begin{aligned} \frac{\mathrm{d}p}{\mathrm{d}x} &= \mathrm{e}^{\mathrm{i}\omega(x-x_s)} \left(\mathrm{i}\omega [H(x - x_s) - H(x)] + [\delta(x - x_s) - \delta(x)] \right) - \mathrm{e}^{-\mathrm{i}\omega(x+x_s)} \left(\mathrm{i}\omega H(-x) + \delta(x) \right) \\ &= \mathrm{i}\omega \mathrm{e}^{\mathrm{i}\omega(x-x_s)} [H(x - x_s) - H(x)] - \mathrm{i}\omega \mathrm{e}^{-\mathrm{i}\omega(x+x_s)} H(-x) + \delta(x - x_s) - 2\mathrm{e}^{-\mathrm{i}\omega x_s} \delta(x) \end{aligned} \tag{4.61}$$

This finally gives:

$$v = \mathrm{e}^{\mathrm{i}\omega(x-x_s)} [H(x - x_s) - H(x)] - \mathrm{e}^{-\mathrm{i}\omega(x+x_s)} H(-x) \tag{4.62}$$

4.3.3 Integral Formulation with a Gaussian Distribution

This integral formulation employing a Gaussian distribution is introduced to elucidate the operation of the reflection method in numerical simulations, where volumetric source terms are

weighted by a Gaussian support function.
The governing equations are expressed as follows:

$$-\mathrm{i}\omega p + \frac{\mathrm{d}v}{\mathrm{d}x} = \delta(x - x_s) \tag{4.63}$$

$$-\mathrm{i}\omega v + \frac{\mathrm{d}p}{\mathrm{d}x} = \delta(x - x_s) + Ap(0)\delta_B(x) \tag{4.64}$$

with x_s the source position and δ_B is a normalized Gaussian distribution defined as

$$\delta_B(x) = \frac{1}{\sqrt{\pi}b} \exp\left(-\frac{x^2}{b^2}\right) \tag{4.65}$$

A spatial Fourier transform is now applied:

$$\hat{p}(k) = \int_{-\infty}^{+\infty} p(x)\,\mathrm{e}^{-\mathrm{i}kx}\,\mathrm{d}x \qquad \hat{v}(k) = \int_{-\infty}^{+\infty} v(x)\,\mathrm{e}^{-\mathrm{i}kx}\,\mathrm{d}x \tag{4.66}$$

This gives:

$$-\mathrm{i}\omega\hat{p} + \mathrm{i}k\hat{v} = \mathrm{e}^{-\mathrm{i}kx_s} \tag{4.67}$$

$$-\mathrm{i}\omega\hat{v} + \mathrm{i}k\hat{p} = \mathrm{e}^{-\mathrm{i}kx_s} + Ap(0)\exp\left(-\frac{k^2b^2}{4}\right) \tag{4.68}$$

Equation (4.68) is now multiplied by $\mathrm{i}k$, that reads:

$$-\mathrm{i}\omega\mathrm{i}k\hat{v} + (\mathrm{i}k)^2\hat{p} = \mathrm{i}k\,\mathrm{e}^{-\mathrm{i}kx_s} + A\mathrm{i}kp(0)\exp\left(-\frac{k^2b^2}{4}\right) \tag{4.69}$$

By combining Eqs. (4.67) and (4.69), one obtains:

$$[(\mathrm{i}k)^2 - (\mathrm{i}\omega)^2]\hat{p} = (\mathrm{i}k + \mathrm{i}\omega)\,\mathrm{e}^{-\mathrm{i}kx_s} + A\mathrm{i}kp(0)\exp\left(-\frac{k^2b^2}{4}\right). \tag{4.70}$$

This gives:

$$\hat{p} = \frac{\mathrm{i}k + \mathrm{i}\omega}{(\mathrm{i}k)^2 - (\mathrm{i}\omega)^2}\,\mathrm{e}^{-\mathrm{i}kx_s} + A\frac{\mathrm{i}k}{(\mathrm{i}k)^2 - (\mathrm{i}\omega)^2}p(0)\exp\left(-\frac{k^2b^2}{4}\right) \tag{4.71}$$

$$= \frac{1}{\mathrm{i}k - \mathrm{i}\omega}\,\mathrm{e}^{-\mathrm{i}kx_s} + \frac{A}{2}\left(\frac{1}{\mathrm{i}k - \mathrm{i}\omega} + \frac{1}{\mathrm{i}k + \mathrm{i}\omega}\right)p(0)\exp\left(-\frac{k^2b^2}{4}\right). \tag{4.72}$$

Three integrals are now defined:

$$p_1 = \frac{1}{2\pi}\int_{-\infty}^{+\infty} \frac{1}{\mathrm{i}k - \mathrm{i}\omega}\, \mathrm{e}^{-\mathrm{i}kx_s}\, \mathrm{e}^{\mathrm{i}kx}\, \mathrm{d}k \tag{4.73}$$

$$p_2 = \frac{1}{2\pi}\int_{-\infty}^{+\infty} \frac{\exp\left(-\dfrac{k^2b^2}{4}\right)}{\mathrm{i}k - \mathrm{i}\omega}\, \mathrm{e}^{\mathrm{i}kx}\, \mathrm{d}k \tag{4.74}$$

$$p_3 = \frac{1}{2\pi}\int_{-\infty}^{+\infty} \frac{\exp\left(-\dfrac{k^2b^2}{4}\right)}{\mathrm{i}k + \mathrm{i}\omega}\, \mathrm{e}^{\mathrm{i}kx}\, \mathrm{d}k \tag{4.75}$$

The integral p_1 in Eq. (4.73) has already been solved and the solution is given in Eq. (4.55). A detailed resolution for the integrals p_2 and p_3 is given in Appendix C.
The integral p_2 gives:

$$p_2 = \frac{1}{2}\exp\left(-\frac{\omega^2b^2}{4}\right)\exp\left(\mathrm{i}\omega x\right)\operatorname{erfc}\left(-\frac{x}{b} - \frac{\mathrm{i}\omega b}{2}\right) \tag{4.76}$$

The integral p_3 gives:

$$p_3 = \frac{1}{2}\exp\left(-\frac{\omega^2b^2}{4}\right)\exp\left(-\mathrm{i}\omega x\right)\operatorname{erfc}\left(\frac{x}{b} - \frac{\mathrm{i}\omega b}{2}\right) \tag{4.77}$$

By combining the three solutions, the resulting pressure field is given by:

$$\begin{aligned} p = \mathrm{e}^{\mathrm{i}\omega(x-x_s)}H(x-x_s) + \frac{A}{4}p(0)\exp\left(-\frac{\omega^2b^2}{4}\right) \\ \left[\mathrm{e}^{\mathrm{i}\omega x}\operatorname{erfc}\left(-\frac{x}{b} - \frac{\mathrm{i}\omega b}{2}\right) - \mathrm{e}^{-\mathrm{i}\omega x}\operatorname{erfc}\left(\frac{x}{b} - \frac{\mathrm{i}\omega b}{2}\right)\right] \end{aligned} \tag{4.78}$$

For $x/b \ll -1$ the complementary error function $\operatorname{erfc}(x/b)$ tends to 2, for $x/b \gg 1$ it tends to 0. For $x = 0$, $\operatorname{erfc}(0) = 1$.

- For $x_s > 0$, $p(0) = 0$, and the solution is $p = \mathrm{e}^{\mathrm{i}\omega(x-x_s)}H(x-x_s)$, regardless of the value of A.
- For $x_s < 0$, $p(0) = \mathrm{e}^{-\mathrm{i}\omega x_s}$, which gives:

$$\begin{aligned} p = \mathrm{e}^{\mathrm{i}\omega(x-x_s)}H(x-x_s) + \frac{A}{4}\exp\left(-\frac{\omega^2b^2}{4}\right) \\ \left[\mathrm{e}^{\mathrm{i}\omega(x-x_s)}\operatorname{erfc}\left(-\frac{x}{b} - \frac{\mathrm{i}\omega b}{2}\right) - \mathrm{e}^{-\mathrm{i}\omega(x+x_s)}\operatorname{erfc}\left(\frac{x}{b} - \frac{\mathrm{i}\omega b}{2}\right)\right] \end{aligned} \tag{4.79}$$

If $|x|/b \gg 1$, the complementary error function could be approximated by a Heaviside function

$\operatorname{erfc}(x/b) \simeq 2H(-x)$. This yields the simplified formula:

$$p \simeq \mathrm{e}^{\mathrm{i}\omega(x-x_s)}H(x-x_s) + \frac{A}{2}\exp\left(-\frac{\omega^2 b^2}{4}\right)(\mathrm{e}^{\mathrm{i}\omega(x-x_s)}H(x) - \mathrm{e}^{-\mathrm{i}\omega(x+x_s)}H(-x)). \tag{4.80}$$

A reflection coefficient r and a transmission coefficient t are then defined as:

$$r = -\frac{A}{2}\exp\left(-\frac{\omega^2 b^2}{4}\right) \tag{4.81}$$

$$t = 1 + \frac{A}{2}\exp\left(-\frac{\omega^2 b^2}{4}\right) \tag{4.82}$$

With $A = -2$, one obtains:

$$p = \mathrm{e}^{\mathrm{i}\omega(x-x_s)}H(x-x_s) - \frac{1}{2}\exp\left(-\frac{\omega^2 b^2}{4}\right) \left[\mathrm{e}^{\mathrm{i}\omega(x-x_s)}\operatorname{erfc}\left(-\frac{x}{b} - \frac{\mathrm{i}\omega b}{2}\right) - \mathrm{e}^{-\mathrm{i}\omega(x+x_s)}\operatorname{erfc}\left(\frac{x}{b} - \frac{\mathrm{i}\omega b}{2}\right)\right] \tag{4.83}$$

with the simplified formula:

$$p \simeq \mathrm{e}^{\mathrm{i}\omega(x-x_s)}\left[H(x-x_s) - \exp\left(-\frac{\omega^2 b^2}{4}\right)H(x)\right] + \exp\left(-\frac{\omega^2 b^2}{4}\right)\mathrm{e}^{-\mathrm{i}\omega(x+x_s)}H(-x) \tag{4.84}$$

and the reflection and transmission coefficients become:

$$r = \exp\left(-\frac{\omega^2 b^2}{4}\right) \tag{4.85}$$

$$t = 1 - \exp\left(-\frac{\omega^2 b^2}{4}\right) \tag{4.86}$$

If $\omega b \ll 1$, the signal effectively cancels for $x > 0$, and a reflected wave with the same amplitude than the incident wave is generated for $x < 0$.
As previously, the velocity is calculated from Eq. (4.64):

$$-\mathrm{i}\omega v = -\frac{\mathrm{d}p}{\mathrm{d}x} + \delta(x-x_s) - 2\mathrm{e}^{-\mathrm{i}\omega x_s}\delta_b(x) \tag{4.87}$$

This yields:

$$v = \mathrm{e}^{\mathrm{i}\omega(x-x_s)}H(x-x_s) - \frac{1}{2}\exp\left(-\frac{\omega^2 b^2}{4}\right) \left[\mathrm{e}^{\mathrm{i}\omega(x-x_s)}\operatorname{erfc}\left(-\frac{x}{b} - \frac{\mathrm{i}\omega b}{2}\right) + \mathrm{e}^{-\mathrm{i}\omega(x+x_s)}\operatorname{erfc}\left(\frac{x}{b} - \frac{\mathrm{i}\omega b}{2}\right)\right] \tag{4.88}$$

In particular, the velocity at $x = 0$ is given by :

$$v(x=0) = \mathrm{e}^{-\mathrm{i}\omega x_s}\left[1 - w\left(\frac{\omega b}{2}\right)\right] \tag{4.89}$$

which tends to 0 as $\omega b/2 \to 0$.

4.3.4 1D Pulse on a Perfectly Rigid Wall

The first academic case considers the reflection of a one-dimensional acoustic pulse from a rigid wall. The pulse propagates along the x-axis and the wall is located at $x = x_w$. The pulse has a Gaussian spatial distribution and is defined as follows:

$$p' = a\frac{\sqrt{\log 2}}{\sqrt{\pi}b_0}\exp\left[-\log 2\frac{(x-x_0)^2}{b_0^2}\right] \tag{4.90}$$

where a is a dimensionless coefficient, x_0 is the pulse initial position, b_0 is the half-width of the Gaussian support. For this case, the parameters are set to $a = 10^{-5}$, $x_0 = 25$, $b_0 = 0.8$ and $x_w = 40$.

The source term for the momentum conservation equation used to impose reflection at the wall is the same as that derived in Section 4.2. In this case, the wall is located exactly at a mesh point $x = x_w$, allowing the wall pressure $p_w(t) = p(x_w, t)$ to be directly evaluated at each sub-step of the Runge-Kutta loop without the need for interpolation. The source term is then defined as $\Lambda_{\rho u}(t) = -2p_w(t)\delta_b$, where δ_b is the Gaussian support defined in Eq. 3.50, with $b = \Delta x$. It should be noted that if the wall were located to the left of the acoustic pulse, i.e. $x_w < x_0$, the wall normal would point in the positive x-direction, and the corresponding source term would therefore have a positive sign.

To validate the method, the numerical solution is directly compared with the analytical solution for the considered case. The analytical solution for the pressure and the velocity field is given by:

$$p_{ex} = AH\left(x_w - x\right)\left[\exp\left(-\log 2\frac{(x-x_0-c_0t)^2}{b^2}\right) + \exp\left(-\log 2\frac{(x+x_0-2x_w+c_0t)^2}{b^2}\right)\right] \tag{4.91}$$

$$u_{ex} = AH\left(x_w - x\right)\left[\exp\left(-\log 2\frac{(x-x_0-c_0t)^2}{b^2}\right) - \exp\left(-\log 2\frac{(x+x_0-2x_w+c_0t)^2}{b^2}\right)\right] \tag{4.92}$$

where $A = a\dfrac{\sqrt{\log 2}}{\sqrt{\pi}b}$ and $H(x)$ is the Heaviside function such that $H(0) = 1$.

A convergence study was conducted to assess order of the reflection method. Four simulations were carried out using progressively refined spatial resolutions, with the mesh spacing Δx ranging

from 0.1 to 0.0125. This corresponds to a number of points per wavelength ranging from 44 to 352.

The relative error between the analytical and numerical solutions at a given time step of the simulation is computed as follows:

$$\varepsilon_r = \frac{|p_{num} - p_{ex}|_\infty}{|p_{ex}|_\infty} \tag{4.93}$$

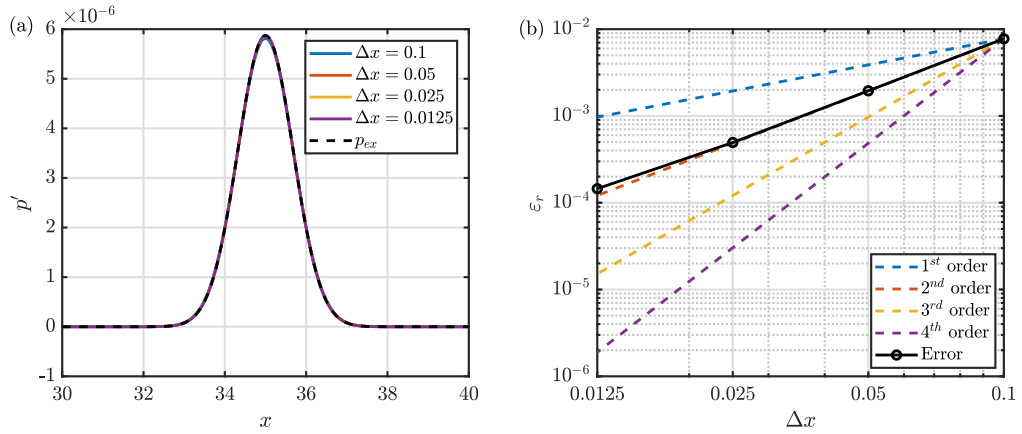

Figure 4.4: (a) Comparison of the analytical solution p_{ex} with simulations using different mesh spacings Δx at $t = 20$ s, and (b) relative numerical error ε_r plotted as a function of the spatial step Δx.

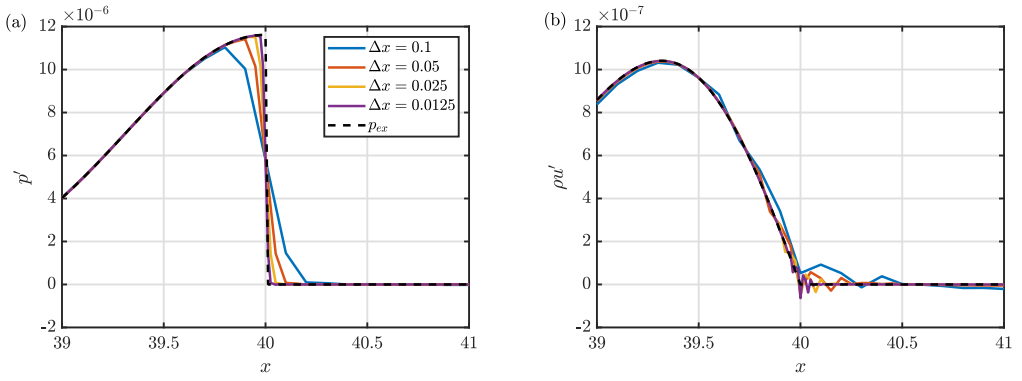

Figure 4.5: Comparison of the analytical solution with simulations using different spatial steps Δx at $t = 14.9$ s for (a) pressure and (b) momentum.

For the case considered, with the chosen parameters, reflection occurs for $t \in [13, 17]$ s. The analytical and numerical solutions at $t = 20$ s are compared in Fig. 4.4(a), showing that both the amplitude and phase of the numerical solution closely match the analytical solution. The corresponding relative error ε_r is presented in Fig. 4.4(b). The results confirm that the proposed numerical method achieves second-order accuracy when the wall is aligned with a mesh point.

The pressure and momentum of the signal reflected at the wall at $t = 14.9$ s are shown in Fig. 4.5(a) and Fig. 4.5(b), respectively. As the mesh is refined, the numerical solution increasingly

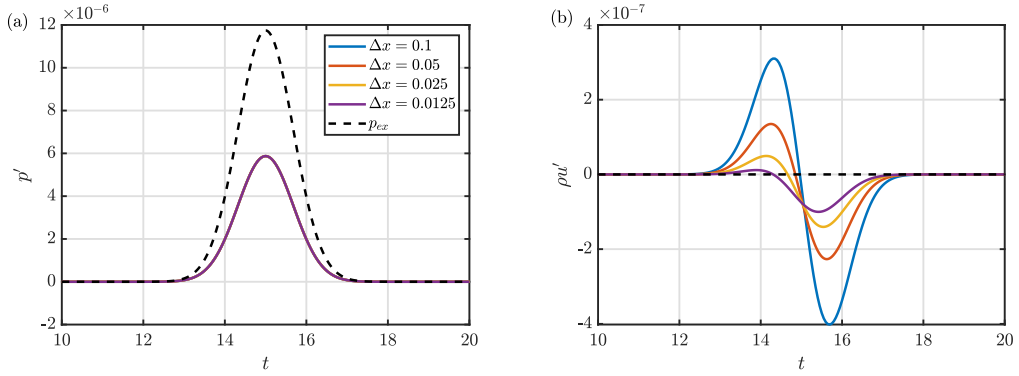

Figure 4.6: Comparison of the analytical solution with simulations using different spatial steps Δx at $x = x_w$ s for (a) pressure and (b) momentum.

aligns with the analytical solution near $x = x_w$. This behavior is inherent to the method, as the volumetric source term is applied precisely at $x = x_w$, centering the Gaussian support on the wall. This ensures high accuracy throughout the domain, except at points within the Gaussian, whose half-width is Δx. Numerical oscillations are observed in the velocity near $x = x_w$ and are damped using the selective filter applied across the computational domain.

The pressure and momentum time histories recorded at $x = x_w$ are presented in Fig. 4.6(a) and Fig. 4.6(b), respectively. As the mesh is refined, the wall pressure signal remains unchanged and corresponds to exactly half of the analytical solution. This behavior ensures the correct definition of the wall source term, since the signal measured at the wall is effectively doubled. Conversely, the velocity signal progressively approaches zero with mesh refinement.

Interpolation

The case where the wall position does not coincide with a mesh point is now considered. The wall is now positioned at $x_w = 40.068$, a location that does not coincide with any mesh points used in the convergence study. In this configuration, the wall pressure signal p_w is not directly available and must be obtained through interpolation to compute the corresponding reflection source term. A convergence study was conducted using Lagrange polynomial interpolations.

Lagrange interpolation is a technique used to construct a polynomial that passes exactly through a given set of known points (x_i, f_i), where $f_i = f(x_i)$. If there are N distinct points (x_1, f_1), (x_2, f_2), ..., (x_N, f_N), then the Lagrange interpolating polynomial is:

$$P(x) = \sum_{i=1}^{N} f_i L_i(x) \tag{4.94}$$

where $L_i(x)$ is the Lagrange basis polynomial defined as:

$$L_i(x) = \prod_{\substack{j=1 \\ j \neq i}}^{N} \frac{x - x_j}{x_i - x_j} \tag{4.95}$$

The resulting polynomial is therefore of degree $N-1$.

In this case, interpolation was carried out using an equal number of points on each side of the wall. A spatial convergence study was then conducted for different Lagrange polynomials with a total of $N = 2$, 4, 6, 8, 10 and 20 points.

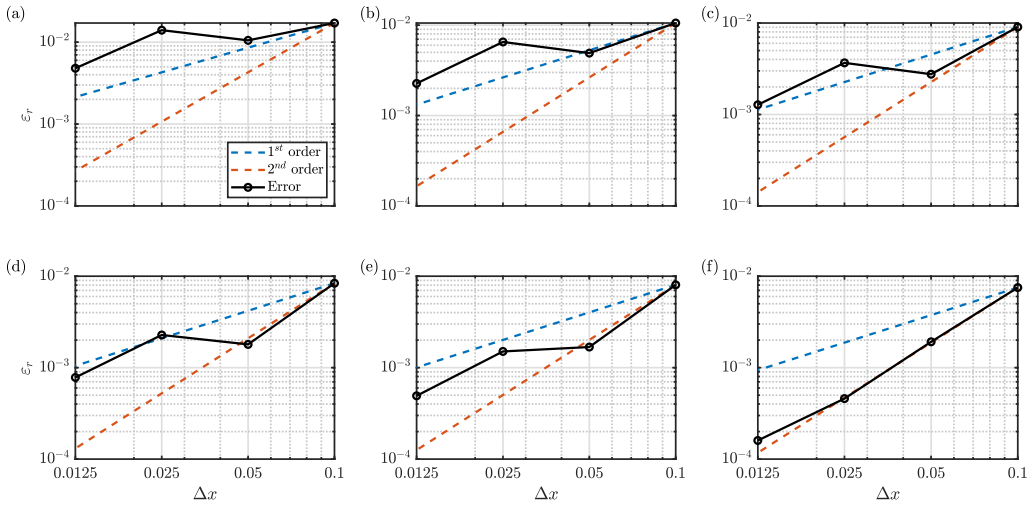

Figure 4.7: Relative error between the analytical and numerical solutions for different spatial mesh steps and number of interpolation points (a) $N = 2$, (b) $N = 4$, (c) $N = 6$, (d) $N = 8$, (e) $N = 10$, and (f) $N = 20$.

The relative error between the analytical and numerical solutions for different Lagrange polynomial orders is shown in Fig. 4.7. As the number of interpolation points N increases, the overall accuracy improves. The error decreases by roughly one order of magnitude as N increases from 2 to 10. For $N \geq 6$, the error exhibits a second-order slope between $\Delta x = 0.1$ and $\Delta x = 0.05$, followed by a slight increase between $\Delta x = 0.05$ and $\Delta x = 0.025$. This behavior may stem from the use of equispaced interpolation nodes, which are not always optimal depending on the function being interpolated. For $N = 20$, the method achieves second-order accuracy, as in the case where the wall position coincides with a mesh point.

Reflection and Transmission Coefficients

The case of a non-rigid wall is now considered, for which part of the incident wave is reflected and part is transmitted. The reflection and transmission coefficients for a Gaussian-supported volumetric source term, denoted as r and t respectively, are defined in Eqs. (4.81-4.82). The objective is to compare the theoretical coefficients with those obtained numerically.

A series of simulations are conducted using a constant mesh spacing of $\Delta x = 0.025$, while varying the coefficient A. Simulations are now performed for $A = 0.5$, 1, 1.5 and 2. Note that the case with $A = 2$ corresponds to a perfectly rigid, fully reflective wall. The Gaussian support half-width is set to $b_w = \Delta x/\sqrt{\log 2} = 0.03$.

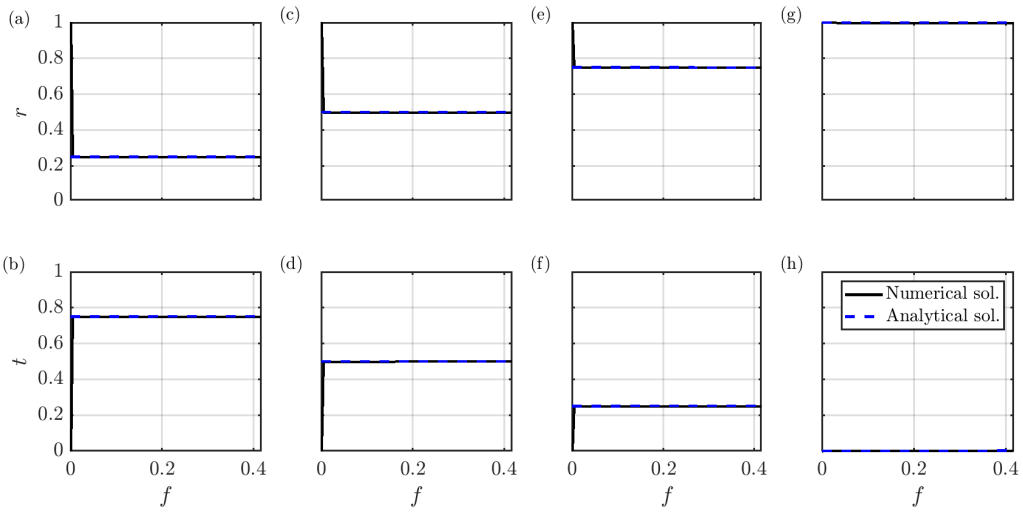

Figure 4.8: Comparison between the analytical and the numerical reflection and transmission coefficients for (a-b) $A = 0.5$, (c-d) $A = 1$, (e-f) $A = 1.5$ and (g-h) $A = 2$.

The analytical and numerical solutions for the reflection and transmission coefficients for the selected values of A are compared in Fig. 4.8. The two solutions coincide in all cases for frequencies up to $f = 1/b_w = 0.4167$, confirming the validity of the proposed method and its ability to prescribe the wall impedance characteristics as desired in the one-dimensional configuration.

4.3.5 2D Pulse with Uniform Mean Flow

The present case considers a two-dimensional acoustic pulse in a uniform mean flow along the y-axis $M_y = 0.8$ reflecting off a perfectly rigid, non-porous wall located at $x_w = 25$. The computational domain extends 30 units in both the x- and y-directions, with a total simulation time of $T = 100$ s. The pulse is initially centered at $(x_0, y_0) = (10, 15)$ and is defined as follows:

$$p' = a \exp\left[-\log 2 \frac{(x - x_0)^2 + (y - y_0)^2}{b_0^2}\right] \tag{4.96}$$

with $a = 10^{-5}$ and $b_0 = 0.8$.

The source term is identical to that used in the one-dimensional case presented in Subsection 4.3.4. The wall is vertical, and the unit normal vector pointing outward from the wall is $\mathbf{n} = (-1, 0)$. Consequently, only one source term appears in the momentum conservation equation along the x-direction, that is $\Lambda_{\rho u} = -2p_w(y,t)\delta_b(x - x_w)$, with $p_w(y,t) = p'(x_w, y, t)$ and δ_b is the Gaussian support defined in Eq. (3.50), with $b = \Delta x$.

The analytical solution for the acoustic pressure field is given by Tam [66]:

$$p_{ex} = \frac{a}{2\alpha} \int_0^\infty \mathrm{e}^{-\frac{\xi^2}{4\alpha}} \cos(\xi t) \left[J_0(\xi\eta) + J_0(\xi\zeta)\right] \xi \, \mathrm{d}\xi \tag{4.97}$$

with $J_0(z)$ the Bessel function of order 0 and

$$\alpha = (\log 2)/b_0^2, \quad \eta = \sqrt{(x-x_0)^2 + (y-y_0-Mt)^2}, \quad \zeta = \sqrt{(x+x_0-2x_w)^2 + (y-y_0-Mt)^2}.$$

A convergence study was conducted to evaluate the spatial order of accuracy of the reflection method in this academic case. Three simulations were then performed using the reflection method with source terms presented in Section 4.2, employing mesh spacings of $\Delta x = 0.1$, 0.05, and 0.025. The relative numerical error was computed in the infinity norm, as defined in Eq. (4.93).

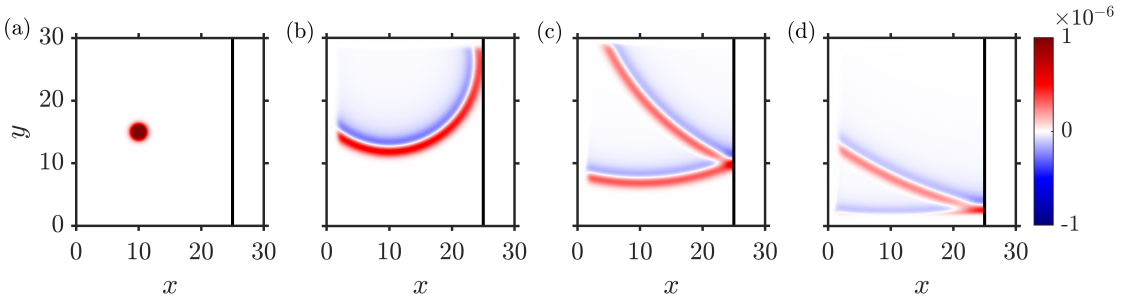

Figure 4.9: Snapshots of the acoustic pressure field at different time instants: (a) $t = 0$ s, (b) $t = 14$ (c) $t = 40$ s, and (d) $t = 70$ s.

Snapshots of the acoustic pressure field are presented in Fig. 4.9(a-d). The pulse is initially centered at $x = x_0$ and propagates asymmetrically within the computational domain due to convective effects induced by the uniform flow M_y. It eventually impinges on the vertical wall at $x = x_w$, where it is reflected. It should be noted that the acoustic wave is fully reflected by the wall, with no transmission through it.

Three probes are placed within the computational domain to record the pressure signal over time. Their positions are $(x_1, y_1) = (24.8, 15)$, $(x_2, y_2) = (24.5, 15)$, and $(x_3, y_3) = (15, 15)$. The comparison between the reference simulation using ghost points and the simulations employing source-term-based reflection for different spatial mesh resolutions is shown in Fig. 4.10(a-c) at the position of the three probes. The numerical solutions show good agreement with the reference results in both amplitude and phase.

In this case as well, the method exhibits second-order accuracy, as indicated by the error reduction observed at the three probes in Fig. 4.10(d–f). In particular, for the probe located at (x_1, y_1), shown in Fig. 4.10(d), a faster error decrease occurs between $\Delta x = 0.1$ and $\Delta x = 0.05$. This behavior arises because the probe is positioned very close to the wall. For the coarser mesh, the probe still lies within the Gaussian support of the source term, leading to reduced numerical accuracy, as previously discussed in Subsection 4.3.4.

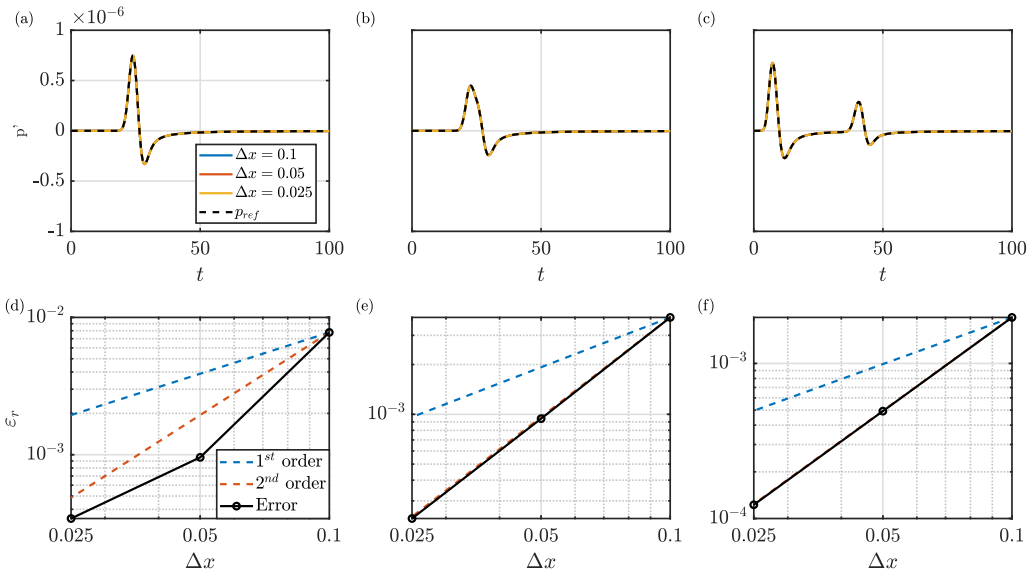

Figure 4.10: Comparison of acoustic pressure time signals at three probe locations: (a) $(x_1, y_1) = (24.8, 15)$, (b) $(x_2, y_2) = (24.5, 15)$, and (c) $(x_3, y_3) = (15, 15)$, and (d-f) the corresponding numerical error.

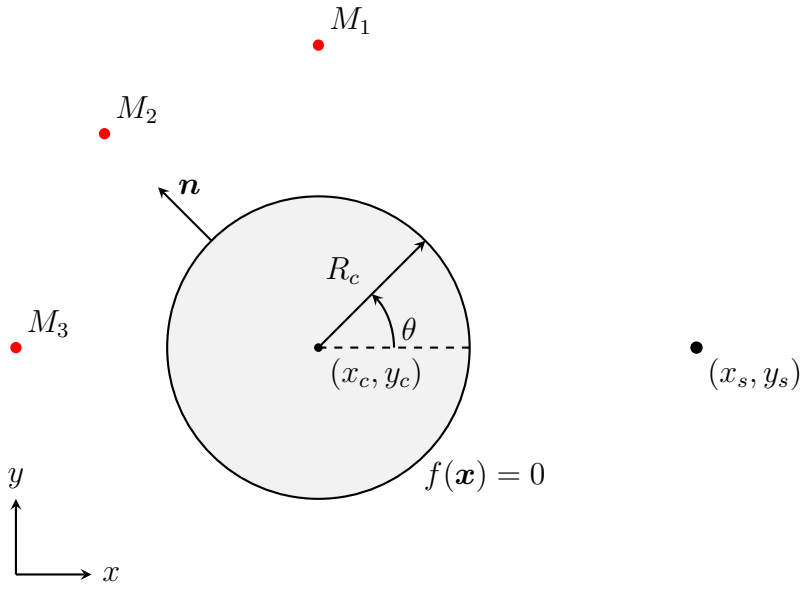

Figure 4.11: Schematic of the computational domain for a pulse scattered by a cylinder.

4.3.6 Scattering of a Pulse by a Cylinder

The scattering of an acoustic pulse by a cylinder is now examined. This configuration represents a classical benchmark in the scientific literature [67]. A schematic of the computational domain is shown in Fig. 4.11. The cylinder has a radius $R_c = 3$ and is centered at $(x_c, y_c) = (15, 15)$. The angular coordinate θ increases in the counterclockwise direction. The acoustic pulse is initially located at $(x_s, y_s) = (25, 15)$ and is defined as follows:

$$p' = a\frac{\log 2}{\pi b_0^2}\exp\left[-\log 2\frac{(x-x_s)^2+(y-y_s)^2}{b_0^2}\right] \tag{4.98}$$

with $a = 10^{-4}$ and $b_0 = 0.8$.

Three probes, M_1, M_2, and M_3, are placed at the same radial distance $r_s = 3.4$ from the cylinder center, at $\theta = \pi/2$, $3\pi/4$, and π, respectively.

The analytical solution for the acoustic field generated by the diffraction of a pulse by a cylinder can be expressed by introducing a velocity potential $\phi(x, y, t)$ such that:

$$u = \frac{\partial\phi}{\partial x}, \quad v = \frac{\partial\phi}{\partial y}, \quad p = -\frac{\partial\phi}{\partial t} \tag{4.99}$$

The analytical solution is derived from the wave equation formulated in polar coordinates for the velocity potential. Using the method of superposition, the potential is decomposed into ϕ_i, representing the incident pulse, and ϕ_r, corresponding to the wave reflected by the cylinder. The resulting pressure field is therefore given by:

$$p(r, \theta, t) = -\frac{\partial\phi}{\partial t} = -\int_0^\infty A(r, \theta, \omega)\,\omega\cos(\omega t)\,\mathrm{d}\omega \tag{4.100}$$

where ω is the pulse angular frequency and A is a coefficient whose definition can be found in [67].

The derivation of the source terms for the scattering of a pulse by a cylinder follows the same reasoning explained in Section 4.2. The wall condition must be satisfied at every point along the cylinder surface:

$$\boldsymbol{u}\cdot\boldsymbol{n} = 0, \quad \forall(x, y) \in \mathcal{C} \tag{4.101}$$

with $\boldsymbol{n} = (\cos\theta, \sin\theta)$ for the cylinder case. The source terms governing total reflection at the wall are thus obtained by using Eqs. (4.25-4.27):

$$\Lambda_\rho = 0 \tag{4.102}$$

$$\Lambda_{\rho u} = 2p_i\cos\theta\delta(f) \tag{4.103}$$

$$\Lambda_{\rho v} = 2p_i\sin\theta\delta(f) \tag{4.104}$$

$$\Lambda_{\rho e} = 0 \tag{4.105}$$

Because a uniform Cartesian mesh is used, the points on the cylinder surface do not necessarily

coincide with the mesh nodes. In this case, bilinear interpolation is used to evaluate the pressure field at the cylinder surface points.

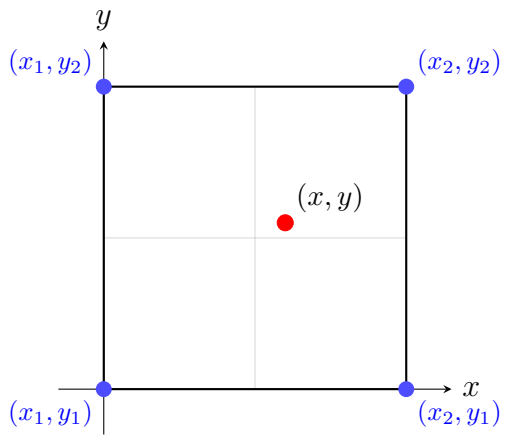

Figure 4.12: Schematic of bilinear interpolation on a square cell.

A schematic of the bilinear interpolation is illustrated in Fig. 4.12. The red point (x, y) denotes the location where the interpolation is required, while the four blue points (x_1, y_1), (x_1, y_2), (x_2, y_1), (x_2, y_2) represent the nodes of the Cartesian mesh. The pressure values at the mesh nodes are known, whereas the pressure at the wall point must be obtained by interpolation. For simplicity, the pressure at the mesh nodes is denoted as $p_{ij} = p(x_i, y_j)$ with $i, j = 1, 2$. Interpolation is first performed between (x_1, y_1) and (x_2, y_1), and then between (x_1, y_2) and (x_2, y_2):

$$p(x, y_1) = p_{11}\frac{x_2 - x}{x_2 - x_1} + p_{21}\frac{x - x_1}{x_2 - x_1} \tag{4.106}$$

$$p(x, y_2) = p_{12}\frac{x_2 - x}{x_2 - x_1} + p_{22}\frac{x - x_1}{x_2 - x_1} \tag{4.107}$$

Interpolation is then carried out along the y-direction:

$$p(x, y) = p(x, y_1)\frac{y_2 - y}{y_2 - y_1} + p(x, y_2)\frac{y - y_1}{y_2 - y_1} \tag{4.108}$$

These three steps in Eqs. (4.106-4.108) can be combined into a single expression to streamline the interpolation process:

$$p(x, y) = (1 - t_x)(1 - t_y)p_{11} + t_x(1 - t_y)p_{21} + (1 - t_x)t_y p_{12} + t_x t_y p_{22} \tag{4.109}$$

with $t_x = (x - x_1) / (x_2 - x_1)$ and $t_y = (y - y_1) / (y_2 - y_1)$.

Snapshots of the acoustic pressure field at three different time instants are presented in Fig. 4.13(a-c). The pulse propagates from its initial position, impacts the cylinder (indicated by a black circle), and is subsequently reflected, producing diffraction patterns throughout the computational domain.

A comparison between the analytical and numerical solutions of the temporal signals at probes M_1, M_2, and M_3 is presented in Fig. 4.14(a–c). The results show good agreement in both

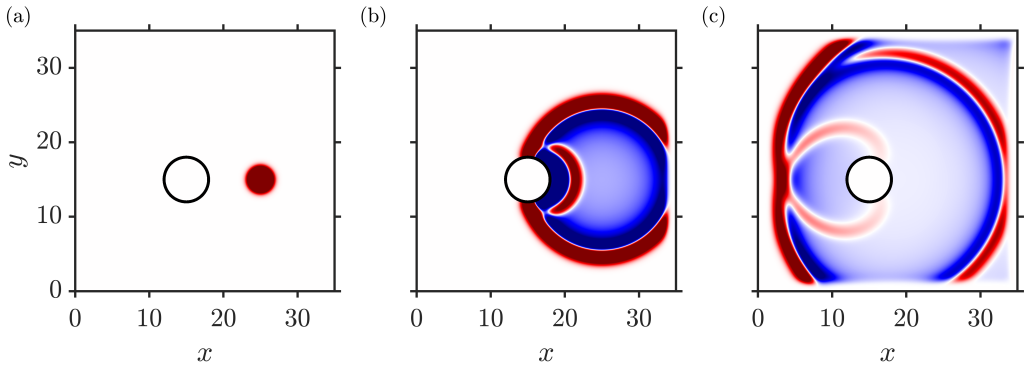

Figure 4.13: Snapshots of the acoustic pressure field at different time instants: (a) $t = 0$ s, (b) $t = 10$ s, and (c) $t = 22.5$ s.

phase and amplitude of the diffracted wave. The relative error at the three probes is reported in Fig. 4.14(d–f), displaying a first-order decrease. This trend is attributed to the bilinear interpolation, which limits the overall accuracy of the method. Alternative interpolation techniques in two-dimensional domains could be employed to improve the convergence order, as discussed in Subsection 4.3.4 for the one-dimensional case.

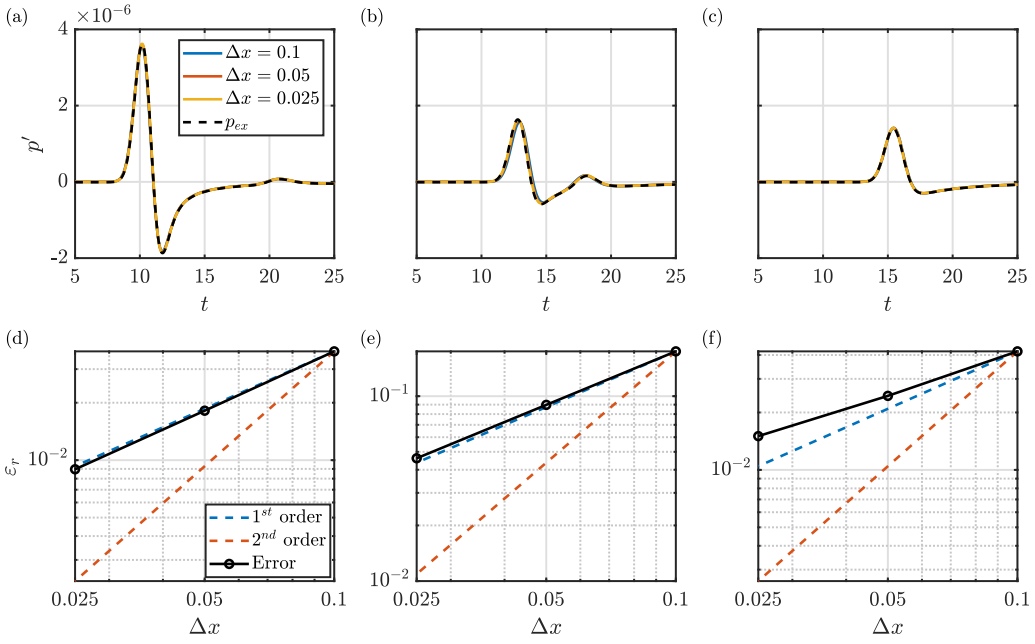

Figure 4.14: Comparison between the analytical and numerical time signals at probes (a) M_1, (b) M_2, and (c) M_3, with panels (d–f) showing the corresponding numerical errors.

4.4 Conclusion

This chapter presented a new method for simulating the reflection of acoustic waves from a physical obstacle. This original approach employs volumetric source terms within the momentum conservation equations to achieve full reflection of incident acoustic waves, with almost no transmission inside the obstacle. These sources are precisely located on the obstacle surface.
The method utilizes the inherent simplicity and efficiency of structured Cartesian meshes, which is a significant advantage for managing complex geometric configurations. Unlike traditional approaches, this method avoids the complications associated with generating curvilinear body-fitted grids.
The effectiveness of method was verified across several academic test cases. A spatial convergence analysis demonstrated that the method achieves second-order accuracy when the mesh conforms to the obstacle geometry. This high accuracy was maintained in non-conforming one-dimensional cases by employing adequate high-order Lagrange interpolation.
However, when the obstacle is immersed within the mesh, as seen in the cylinder scattering benchmark, the method exhibited first-order accuracy. This reduction in convergence order is directly attributed to the limitation of the bilinear interpolation used to evaluate the pressure field at the surface points. Thus, the overall accuracy of the method is highly dependent on the interpolation technique selected for immersed boundaries.

5 Application to unducted single fan

This chapter presents a detailed numerical investigation into the acoustic signature impressed upon an aircraft fuselage by an unducted single fan, focusing on the non-linear propagation of associated shock waves and the effect of boundary layer shielding. The results confirm that non-linear effects are present but exerts only a modest influence on the Sound Pressure Level on the fuselage, leading to a maximum reduction of 1.6 dB for acoustic waves propagating against the mean flow. The study identifies the refraction of sound waves by the fuselage boundary layer as the dominant mechanism governing the acoustic load on the fuselage. A parametric study demonstrates that increasing boundary layer thickness progressively enhances the acoustic shielding. The shielding effect is most pronounced for the thickest turbulent boundary layer considered. In this configuration, referring to the fuselage region upstream of the engine, a maximum reduction of 8 dB is observed on the fuselage portion directly exposed to the engine, whereas a significantly larger reduction of up to 22 dB is achieved in the shadow region. Conversely, the influence of the downstream turbulent boundary layer is found to be negligible.

5.1 Introduction

Unducted aero-engines are currently investigated to reduce environmental footprint of aviation. However, given the absence of a nacelle with acoustic liners around the fan blades and the outlet guide vane (OGV), the propagation of shock-waves generated on the blades and their impact on the fuselage need to be investigated. A tonal noise study for free-field propagation was carried out by Lewis *et al.* [68] using a hybrid approach that couples a Reynolds-averaged Navier-Stokes (RANS) simulation with the Ffowcs-William Hawkings integral formulation. This methodology is representative of the current state of the art in industrial aeroacoustics, where RANS simulations are commonly combined with the FWH acoustic analogy.

For configurations with unducted rotors, the interaction between the engine sound field and the airframe, commonly referred to as installation effects, can influence the acoustic loads on the

fuselage surface. It should be noted, however, that installation effects may also alter the noise generation mechanisms at the source. In the present work, these source-related effects are not addressed: the acoustic source is assumed to be known a priori and is prescribed as an input to the CAA simulations. The analysis therefore focuses exclusively on installation effects associated with sound propagation and scattering. In this context, a central element of the interaction is the fuselage and its turbulent boundary layer, which can refract and scatter the incoming acoustic waves.

Early studies established the fundamental approaches for analyzing these phenomena. Initial two-dimensional models, using plane-wave sources and step-function velocity profiles, showed that the fuselage boundary layer could provide strong acoustic shielding, especially at high cruise Mach numbers [69]. This work was soon extended through more comprehensive three-dimensional theories that represented the fuselage as an infinitely long rigid cylinder. Studies including Hanson *et al.* [70], Lu [71], and McAninch *et al.* [72] combined near-field propeller source models with numerical solutions of wave propagation inside the boundary layer, consistently predicting significant sound attenuation on the forward fuselage surface.

A major difficulty in these formulations was the critical layer singularity in the governing equations, which was resolved through Frobenius series solutions. These models were later validated against flight test data [73], showing good agreement and confirming the importance of accounting for boundary layer effects in noise prediction.

Subsequent contributions refined these models by enhancing source representation, geometric details, and solution methods. Because simplified point sources can introduce large errors, studies by Belyaev [74], Brouwer [75], and Gaffney *et al.* [76] employed more realistic distributed sources, including detailed propeller models, contra-rotating open rotors (CRORs), and spinning ducted fan modes, respectively. While most analytical models are restricted to circular fuselages, Schippers *et al.* [77] developed a hybrid finite element approach that accommodates non-circular cross-sections, showing that geometry can strongly affect the radiated sound field. In parallel, to reduce the cost of numerical integration, Rouvas *et al.* [78] proposed analytical models with simplified linear or step-function velocity profiles. These were shown to approximate the refraction produced by more realistic turbulent power-law profiles, particularly when the shape factor is matched.

While most previous studies examined refraction through a steady mean boundary layer, the critical role of turbulence has also been emphasized. Dierke *et al.* [79] and Siefert *et al.* [80] solved the Linearized Euler Equations, introducing stochastic turbulent fluctuations with the Random-Particle-Method. Their results showed that scattering by unsteady turbulent vortices strongly modifies the surface pressure field, increasing sound levels in the shadow zone, shifting energy to higher frequencies through Doppler effects, and producing spectral broadening or haystacking.

At a more fundamental level, Howe [81] argued that wall shear stress fluctuations - often regarded as dipole sound sources - contribute to acoustic propagation rather than generation. His analysis suggests that surface shear stress reduces, rather than enhances, boundary layer noise radiation,

particularly at low Mach numbers, providing theoretical support for the boundary layer's role in shaping the sound field.

Despite these advances, most studies still rely on linearized formulations, such as the Pridmore–Brown equation [82] or the Linearized Euler Equations, which neglect non-linear propagation effects. Moreover, investigations addressing the most recent unducted single fan configurations remain scarce in the literature [83–88]. Among these, the work of Proskurov *et al.* [89] investigates the acoustic signature on the fuselage by using a frequency domain fast multipole boundary element method (FM-BEM), though it neglects the influence of the boundary layer.

The present study extends previous investigations by considering the non-linear propagation of sound from an unducted single fan through the resolution of the full Euler equations. This approach enables the evaluation of sound levels on the fuselage surface while capturing potential non-linear effects induced by propagation through the strong shear of the boundary layer, though the turbulent field is neglected. Particular focus is placed on the role of boundary layer thickness, a parameter identified as critical in earlier studies, to provide a more comprehensive understanding of the acoustic environment on the aircraft fuselage.

5.2 Numerical setup

The non-linear Euler equations are solved in their conservative form in Cartesian coordinates, as shown in Eq. (3.49). The source term vector $\mathbf{\Lambda}$ is defined over a cylindrical control surface around the rotor, defined by $f(\boldsymbol{x}_s) = 0$. The source terms are computed using the same formulation described in Section 3.4.4.

Note that the equations are solved for perturbative variables with respect to a given based flow. The variables are initialized with their ambient values, that is $\boldsymbol{U}(\mathbf{x}, t = 0) = \big(\rho_0, \rho_0 u_0, \rho_0 v_0, \rho_0 w_0, (\rho e_t)_0\big)$, where the notation $(\cdot)_0$ denotes the base flow quantities, assumed to be known as the governing equations are formulated exclusively for perturbations.

In the present study, the conservative variables field introduced into the computational domain is extracted from a RANS simulation, performed in a configuration where only the rotor is present. The CFD simulation is carried out using the elsA CFD solver [90]. The calculation is performed on a single blade-passage rotor-alone configuration in a moving reference frame, which is then reconstructed over 360° by applying periodicity in the azimuthal direction. The resulting signal is interpolated onto the cylindrical control surface of radius $R_s > R$, where R denotes the rotor radius. The rotor plane lies in the plane $x = 0$. The perturbation field $\big(\rho', (\rho u_i)', (\rho e_t)', p'\big)$ at each point on the cylindrical surface is computed by subtracting the azimuthal mean from the conservative variables extracted from the RANS simulation. The reference frame coincides with that shown in Fig. 3.14, and the simulation is conducted under cruise conditions, with a uniform flow M_x aligned along the x-axis and no incidence. The fuselage is modeled using the reflection method described in Chapter 4. Its geometry is simplified to a cylindrical shape for the purposes

of this study. However, this assumption is not restrictive, as the injection method presented in Chapter 3 is applicable to arbitrary surface geometries.

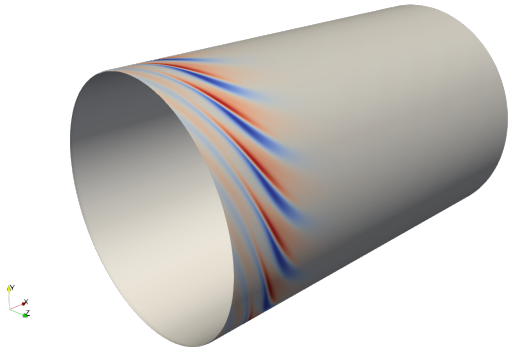

Figure 5.1: Isometric view of the pressure oscillations field extracted from the RANS simulation on a cylindrical control surface.

The input cylindrical surface around the rotor is shown in Fig. 5.1. Since the RANS simulation is performed on a single blade sector, the resulting signal is periodic. This signal is then rotated at each iteration around the x-axis of the cylindrical surface according to the rotor's angular velocity, defined as $\Omega = \Delta\theta/\Delta t$, where $\Delta\theta$ is the angular displacement per time step Δt. Two complete rotations are performed in the simulation.

The Euler equations are solved on a uniformly spaced Cartesian grid, with $\Delta x = \Delta y = \Delta z$ where Δx, Δy, Δz are the grid sizes in the x-, y-, and z- direction, respectively. Spatial derivatives are evaluated using a fourth-order, 11-point finite difference scheme with low dispersion and dissipation [5]. Time integration is carried out with a six-stage, fourth-order low-storage Runge–Kutta scheme. The source terms are introduced at the final sub-step of each iteration. A selective 11-point filter is applied across the domain to suppress spurious grid-to-grid oscillations. Perfectly Matched Layers (PML) [8] are implemented at the domain boundaries to damp outgoing acoustic waves. All simulations are performed with a Courant–Friedrichs–Lewy number of 0.5.

A schematic of the computational domain is shown in Fig. 5.2. The left side contains the cylindrical control surface enclosing the unducted single fan engine, while the fuselage is positioned on the right side. The coordinate system is defined with the x-axis aligned with the freestream, the z-axis oriented horizontally toward the fuselage, and the y-axis directed upward. The simulation is carried out under cruise conditions, with a fixed uniform freestream Mach number $M_x \in [0.75, 0.8]$ and no incidence. The fuselage is modeled as a cylinder of radius R_f, located at a distance d from the engine, and is surrounded by a uniform boundary layer of thickness δ. The angle θ is defined with respect to the center of the fuselage, and specifies the angular position on its surface. It increases counterclockwise, with $\theta = 0$ corresponding to the side of the fuselage shielded from the engine and $\theta = \pi$ corresponding to the side facing the engine.

A first set of simulations, presented in Section 5.3, was conducted without the fuselage in the computational domain to compare acoustic propagation predicted by the Euler solver with that obtained using the Ffowcs Williams–Hawkings analogy. A second set of simulations, presented in

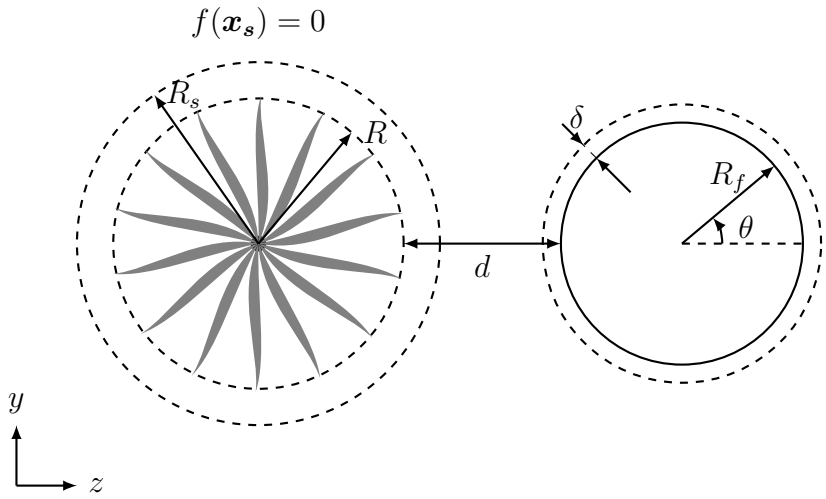

Figure 5.2: Sketch of the computational domain on the yz-plane at $x = 0$. On the left, the unducted single fan engine with radius R and the cylindrical control surface of radius R_s where the sources are defined. On the right, fuselage with radius R_f, located at a distance d from the engine, surrounded by a uniform boundary layer of thickness δ.

Section 5.4, includes the fuselage and was performed to investigate the resulting acoustic signature on the fuselage in the presence of a boundary layer.

5.3 Comparison with Ffowcs-Williams Hawkings

This section presents the results of shock-wave propagation generated by an unducted single fan in a free-field configuration. The objective is to assess non-linear propagation effects and to compare the predictions of the Euler solver with those obtained using the Ffowcs Williams–Hawkings analogy.

The Euler computational domain consists of $241 \times 255 \times 334$ points in the x, y, and z directions, respectively, with 24 points per wavelength in the upstream-propagating wave region. The resulting acoustic pressure field generated by the source terms distributed along the cylindrical surface is shown in Fig. 5.3.

The signal primarily propagates outward from the cylindrical surface and is subsequently absorbed by the PML at the domain boundaries. Due to the presence of a uniform flow M_x, acoustic waves propagating upstream against the flow direction undergo a reduction in wavelength, whereas waves propagating downstream experience an increase in wavelength. However, a small portion of the signal penetrates into the surface. This effect is likely attributable to the fact that the source signal is extracted directly from a RANS simulation, rather than being analytically defined as in the previous more academic cases. Nevertheless, this does not compromise the validity of the results, as demonstrated by the comparison with the FWH method for Sound Pressure Level (SPL) computation on the xz-plane, presented in Fig. 5.4. The highest SPL is observed in the vicinity of the rotor plane at $x/R_s = 0$ and gradually decreases upstream and downstream, as

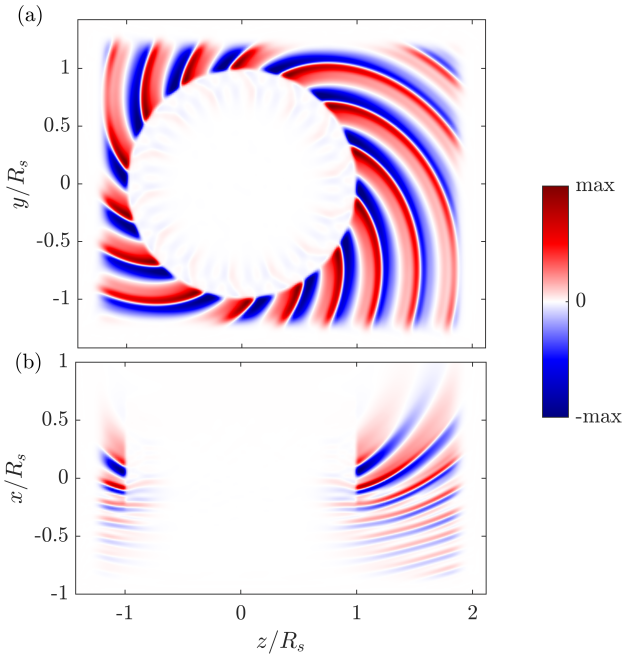

Figure 5.3: Pressure field generated by an unducted single fan in (a) the yz-plane and (b) the xz-plane.

well as along z.

A more quantitative comparison between the two approaches is presented in Fig. 5.5. The SPL is plotted along three lines on the xz-plane at $y = 0$, corresponding to normalized vertical positions $z/R_s = 1.03$, 1.41, and 1.72 in Figs. 5.5 (a), (b), and (c), respectively. In all cases, the curves show excellent agreement, with near-complete overlap, confirming the proposed method as a valid alternative to the FWH integral formulation.

Assessment of Non-linear Effects

Shockwaves generated by rotor blade tips during cruise flight may experience non-linear acoustic propagation effects. To evaluate the significance of these effects on the SPL, the source intensity is progressively increased. Two additional simulations are conducted by introducing a scaling factor α that multiplies all source terms in the governing equations. For each simulation, the SPL is computed and normalized by the corresponding scaling factor, enabling direct comparison among the different numerical cases.

Before presenting the results, it is useful to recall the findings reported in Section 3.4.2 concerning the evolution of shockwaves in the presence of a uniform flow. The presence of a mean flow reduces the shock formation distance for waves propagating upstream and increases it for waves propagating downstream. This phenomenon has been recognized in the scientific literature for several decades. To the author's knowledge, the first study to report the shock formation distance $\bar{x}$ in a uniform flow was published by Polyakova [91] in 1961. Subsequent studies have further examined the shock formation distance in ducts [92, 93]. This distance is defined as the distance

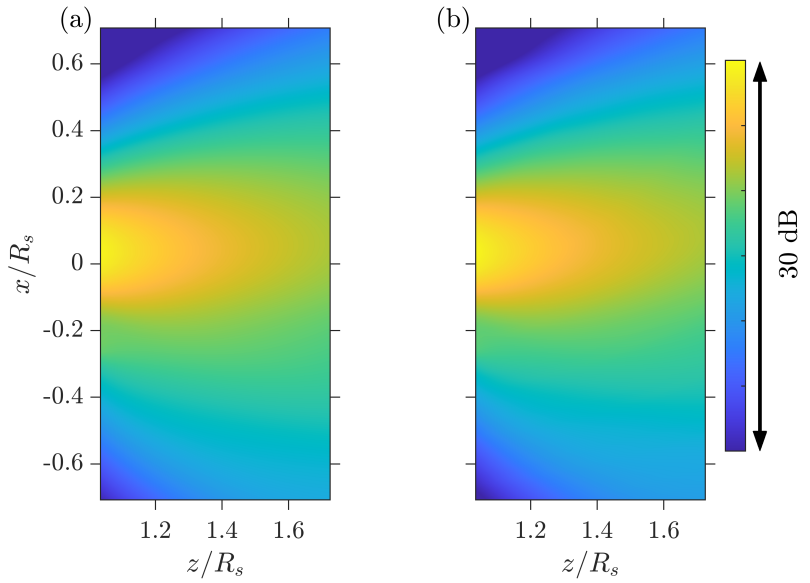

Figure 5.4: SPL in the xz-plane at $y = 0$ for (a) the Ffowcs Williams-Hawkings integral formulation and (b) the present method.

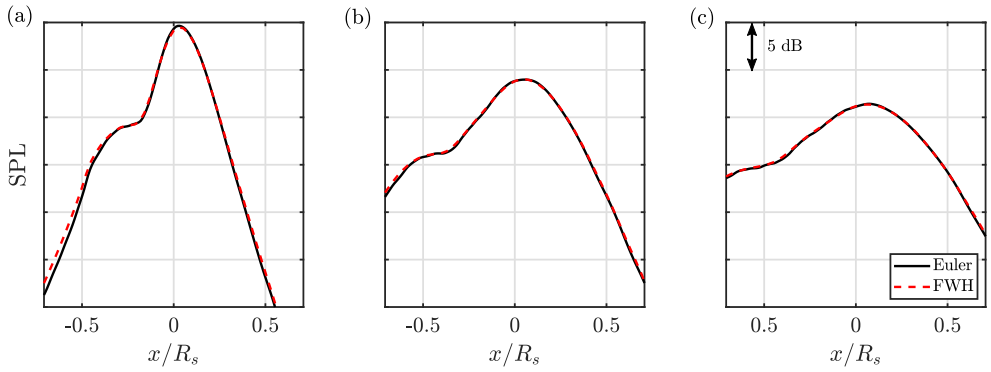

Figure 5.5: Comparison of the sound pressure level between the Ffowcs Williams-Hawkings integral formulation and the present method in the xz-plane at $y = 0$ at (a) $z/R_s = 1.03$, (b) $z/R_s = 1.41$ and (c) $z/R_s = 1.72$.

required for a sinusoidal plane wave to first present a vertical tangent. It is expressed as:

$$\bar{x} = \frac{c_0^2 \left(1 \pm M_0\right)^2}{\beta u_0 \omega} \tag{5.1}$$

where M_0 is the Mach number, u_0 is the peak flow velocity, and β is the non-linear coefficient defined as

$$\beta = \frac{\gamma + 1}{2} \tag{5.2}$$

for air considered as an ideal gas. It is noted that in Eq. (5.1) the minus sign applies to waves propagating against the flow, while the plus sign applies to waves propagating with the flow.
The SPL predicted by the FWH method with that obtained from the three Euler simulations at three locations along the x-axis are compared in Fig. 5.6. The linear case corresponds to

the configuration used for the comparison with the FWH formulation, whereas the "NL1" and "NL2" cases represent the two non-linear configurations with scaling factor α equal to 10 and 100, respectively.

Downstream of the rotor, for $x > 0$, the results are identical for all simulations, with complete overlap between the Euler and the FWH curves. This behavior is expected, as waves propagating with the flow do not exhibit non-linear effects for the chosen domain length. Upstream of the rotor, for $x < 0$, the Euler solution progressively diverges from the FWH prediction as α increases. A detailed view of the upstream region is provided in Fig. 5.7, which clearly illustrates the impact of non-linear effects on wave propagation.

For the unducted single-fan configuration under investigation, cruise conditions are assumed, with a fixed free-stream Mach number in the range $M_x \in [0.75, 0.8]$. Using the problem data, the predicted shock formation distance is $\bar{x}/R_s = 0.18$ for upstream-propagating waves and $\bar{x}/R_s = 11$ for downstream-propagating waves. This difference accounts for the slight discrepancy observed between the non-linear Euler simulation and the FWH integral method exclusively upstream of the engine.

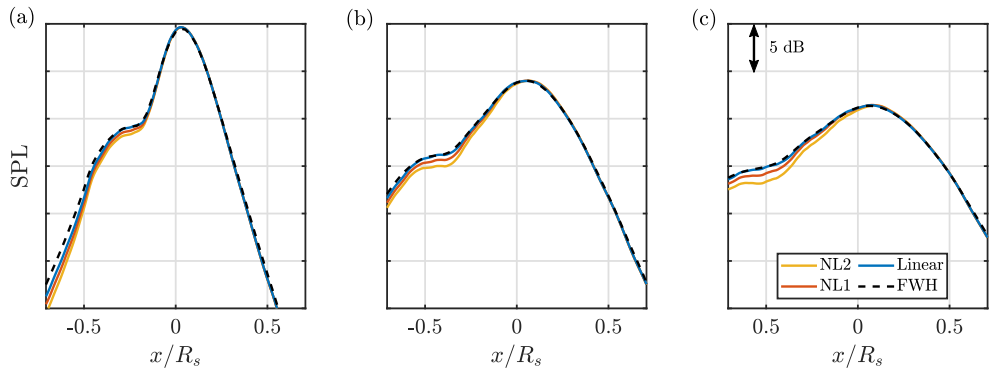

Figure 5.6: Normalized comparison of the sound pressure level between the Ffowcs Williams-Hawkings integral formulation and the present method at $z/R_s = 1.03$ (a), 1.41 (b) and 1.72 (c) for different sources intensities.

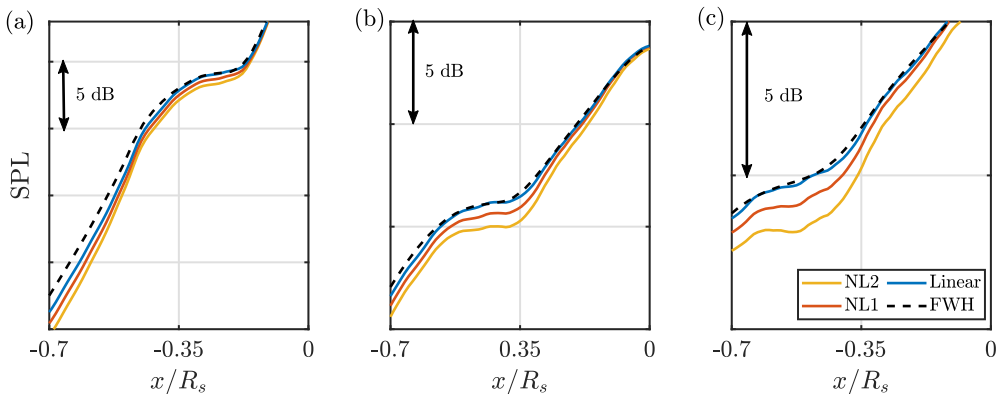

Figure 5.7: Close-up of the region $-0.7 \leq x/R_s \leq 0$ in Fig. 5.6.

5.4 Acoustic Signature on the Fuselage

5.4.1 Non-linear Effects

In an unducted single fan engine, weak shock waves may form at the blade tips under cruise conditions. In such cases, it is important to assess the role of non-linear propagation effects. The non-linear Euler equations account for these effects, which, although small, slightly alter the acoustic signature on the fuselage.

To evaluate their influence, two simulations were carried out. In the first, the source terms were prescribed to reproduce the conservative variable field on the cylindrical control surface extracted from the RANS simulation. In the second, the same source terms were reduced by a factor of 100, effectively removing non-linear effects from propagation. In both cases, the fuselage was modeled without the presence of a boundary layer and assuming slip flow over its surface.

The quantity ΔSPL_{NL} is defined as :

$$\Delta\text{SPL}_{NL} = \text{SPL}_L - \text{SPL}_{NL} \tag{5.3}$$

where SPL_L and SPL_{NL} are the SPL for the linear and the non-linear simulation, respectively. To assess the impact of non-linear effects, the Sound Pressure Level (SPL) is computed on the fuselage surface for both simulations. The distribution of ΔSPL_{NL} over the entire fuselage is presented in Fig. 5.8. Non-linear effects are more pronounced upstream of the rotor, for negative x, and within the shadow region corresponding to $\theta \in [-\pi/2, \pi/2]$.

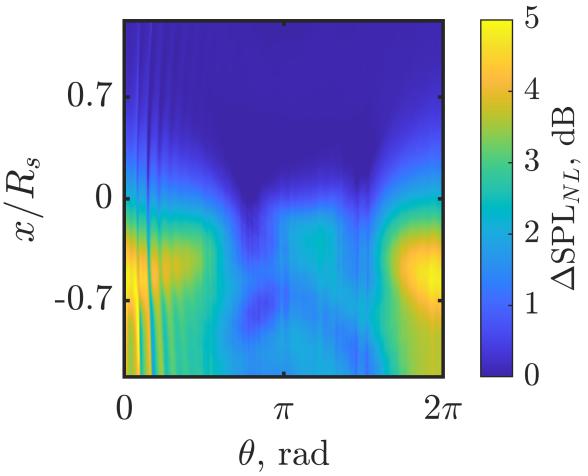

Figure 5.8: Difference in ΔSPL_{NL} on the fuselage surface.

For a more detailed comparison, the sound pressure levels and the corresponding ΔSPL_{NL} are plotted as functions of x at $\theta = \pi$ in Figs. 5.9(a) and 5.9(b), respectively. The results indicate that non-linear effects are most pronounced upstream of the engine, where acoustic waves propagate

against the mean flow. For the case considered, these effects lead to a maximum reduction of 1.8 dB in the SPL on the fuselage at $\theta = \pi$. For waves propagating with the flow, i.e. in the positive x-direction, non-linear effects are negligible, with variations on the order of 0.1 dB.

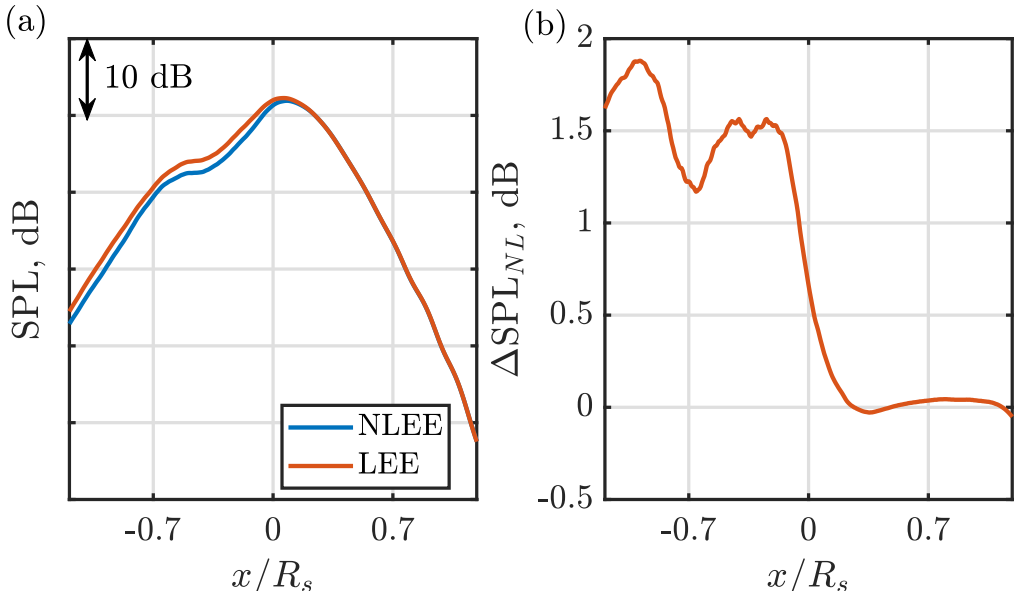

Figure 5.9: (a) Sound Pressure Level and (b) difference in Sound Pressure Level ΔSPL_{NL} between linear and non-linear behavior on the fuselage along the x-coordinate at $\theta = \pi$.

The SPL and ΔSPL_{NL} distributions along the x-direction within the shadow region at $\theta = 0$ are shown in Figs. 5.10(a) and 5.10(b), respectively. In this region, non-linear effects are more significant, with a maximum difference of approximately 5 dB between the linear and non-linear solutions observed upstream of the engine. This peak exceeds the corresponding value at $\theta = \pi$. This behavior can be attributed to the longer propagation distance required for the shock waves to reach the shadow region. When combined with convection effects associated with the presence of a uniform flow, these conditions enhance non-linear effects on propagation.

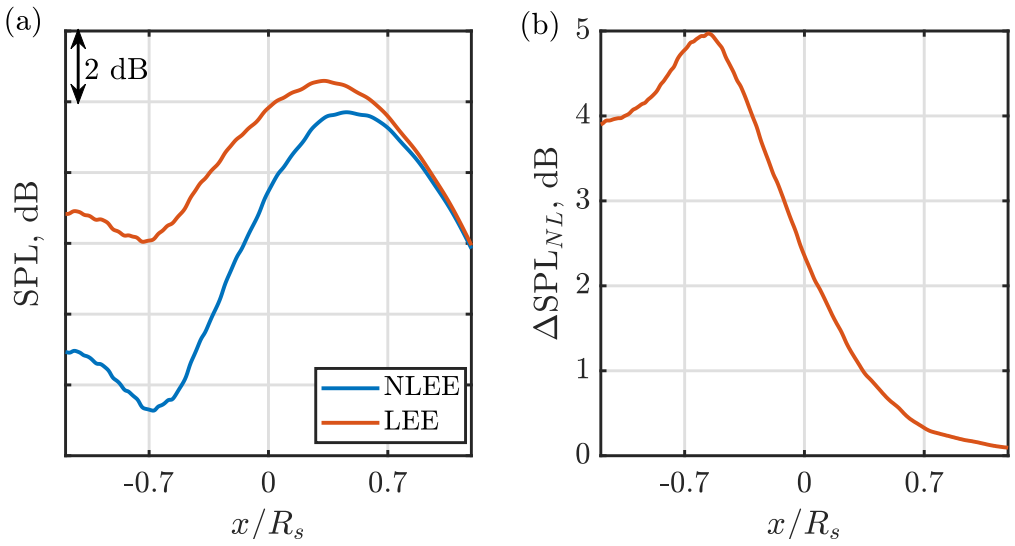

Figure 5.10: (a) Sound Pressure Level and (b) difference in Sound Pressure Level ΔSPL_{NL} between linear and non-linear behavior on the fuselage along the x-coordinate at $\theta = 0$.

Figures 5.11(a) and 5.11(b) present, respectively, the SPL obtained from the two simulations and the corresponding ΔSPL_{NL} as functions of the angular coordinate θ on the rotor plane located at $x = 0$. As previously noted, non-linear effects intensify when approaching the shadow region on the fuselage, reaching a maximum difference of approximately 2.5 dB at $\theta = 0$. These effects become more pronounced when the same distribution is evaluated on yz-planes located further upstream of the engine, whereas they diminish on planes situated further downstream.

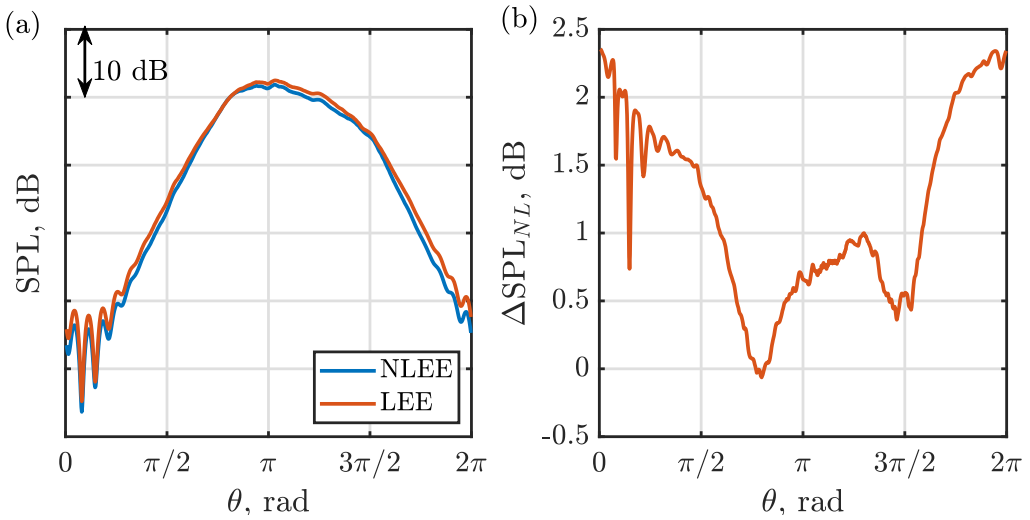

Figure 5.11: (a) Sound Pressure Level and (b) difference in Sound Pressure Level ΔSPL_{NL} between linear and non-linear behavior on the fuselage along the θ-coordinate at $x = 0$.

5.4.2 Boundary layer effects around the fuselage

The boundary layer around the fuselage strongly modifies its acoustic signature, as mentioned in Section 5.1. This shielding effect arises because the velocity gradient near the wall refracts upstream-propagating acoustic waves away from the fuselage [78]. The ratio of acoustic wavelength to boundary layer thickness plays a central role in this process: refraction becomes more pronounced when the wavelength is comparable to or smaller than the boundary layer thickness [76]. Two sets of numerical simulations were conducted to investigate boundary layer effects: one employing a laminar profile and the other employing a turbulent profile. It should be emphasized, however, that given the Reynolds numbers involved, the boundary layer is physically expected to be turbulent; the laminar case is therefore considered as an idealized reference configuration for comparison purposes.

Acoustic ray-based interpretation of boundary layer effects

To provide a qualitative interpretation of the boundary layer effects on the acoustic signature measured on the fuselage, it is useful to adopt a high-frequency asymptotic framework based on geometrical acoustics. In this approach, acoustic propagation is described in terms of rays, which represent the trajectories of wave energy in a moving, inhomogeneous medium. Although this assumption does not strictly apply to the present case, which is characterized by relatively low frequencies, we consider such a description to be valuable for providing physical insight into the underlying refraction mechanism.

Under the geometrical acoustics approximation, sound propagation in a steady, non-uniform mean flow is governed by ray equations derived from the eikonal formulation of the convected wave equation. The local propagation velocity of an acoustic disturbance is given by the superposition of the mean flow velocity and the sound speed in the direction of the local wave vector. Consequently, spatial gradients of the mean velocity field induce refraction of acoustic rays. In vector form, the ray equations can be written as:

$$\frac{d\mathbf{x}}{dt} = \boldsymbol{U}(\mathbf{x}) + c\frac{\mathbf{k}}{|\mathbf{k}|} \tag{5.4}$$

$$\frac{d\mathbf{k}}{dt} = -\mathbf{k}\cdot\nabla\boldsymbol{U} - \nabla c\,|\mathbf{k}| \tag{5.5}$$

where $\mathbf{x}(t)$ is the ray position at a given time t, $\mathbf{k}(t)$ is the local wave vector, $\boldsymbol{U}$ is the steady mean velocity field, and c is the local speed of sound. Equation (5.4) describes the group velocity, given by the superposition of mean flow convection and sound propagation relative to the fluid, while Eq. (5.5) governs refraction due to spatial gradients of the mean flow and of the speed of sound. We now consider a two dimensional domain (x, y) with a vertical wall, where x is the wall-normal coordinate, and y is the streamwise direction. The wall is located at $x = 0$ and the mean flow is parallel to the wall and varies only in the wall normal direction, i.e. $\boldsymbol{U}(x) = \big(0, v(x)\big)$, where $v(x)$ represents the boundary layer profile, increasing from its wall value to the free-stream velocity

V_∞. The position vector is $\boldsymbol{x} = (x, y)$ and the wave vector is $\mathbf{k} = (k_x, k_y)$. The speed of sound c is assumed to be constant. The ray equations described in Eqs. (5.4-5.5) then become:

$$\frac{\mathrm{d}x}{\mathrm{d}t} = c\frac{k_x}{|\mathbf{k}|} \tag{5.6}$$

$$\frac{\mathrm{d}y}{\mathrm{d}t} = V(x) + c\frac{k_y}{|\mathbf{k}|} \tag{5.7}$$

$$\frac{\mathrm{d}k_x}{\mathrm{d}t} = -k_y\frac{\mathrm{d}v}{\mathrm{d}x} \tag{5.8}$$

$$\frac{\mathrm{d}k_y}{\mathrm{d}t} = 0 \tag{5.9}$$

The streamwise component k_y is conserved, while the wall-normal component k_x evolves proportionally to the velocity gradient $\mathrm{d}v/\mathrm{d}x$. Thus the refraction occurs exclusively in the wall-normal direction.

For waves propagating upstream ($k_y < 0$), the interaction with the positive shear $\mathrm{d}v/\mathrm{d}x > 0$ produces systematic bending of rays away from the wall. This reduces the density of rays impinging on the surface in the upstream region, thereby decreasing the local acoustic level.

In contrast, the waves propagating downstream ($k_y > 0$) experience refraction in the opposite sense, which does not lead to the same degree of energy depletion at the wall. This asymmetry explains the preferential attenuation observed upstream of the rotor.

For example, the velocity profile for a laminar boundary layer can be described by the following expression:

$$v(x) = V_\infty \tanh\left(2\frac{x}{\delta}\right) \tag{5.10}$$

where V_∞ denotes the freestream velocity and δ represents the boundary layer thickness, defined as the location at which the velocity reaches 95% of the freestream value, i.e., $v(\delta) = 0.95V_\infty$. A Mach number of 0.8 is considered. In addition, a point source located at $(x_s, y_s) = (1, 0)$ emits rays over the angular range $\theta \in [\pi/2, 3\pi/2]$.

The system of equations defined by Eqs. (5.6-5.9) is solved to determine the ray trajectories, as illustrated in Fig. 5.12 for boundary layer thicknesses $\delta/R_f \in [0, 0.1]$. In Fig. 5.12(a), the flow is uniform and no boundary layer is present; consequently, the rays are influenced solely by convection and undergo a single reflection upon reaching the wall at $x = 0$. As the boundary layer thickness increases, upstream-propagating rays experience refraction due to the velocity gradient, and this effect becomes progressively more pronounced, as shown in Figs. 5.12(b–d). In contrast, the influence on downstream-propagating rays is comparatively weaker.

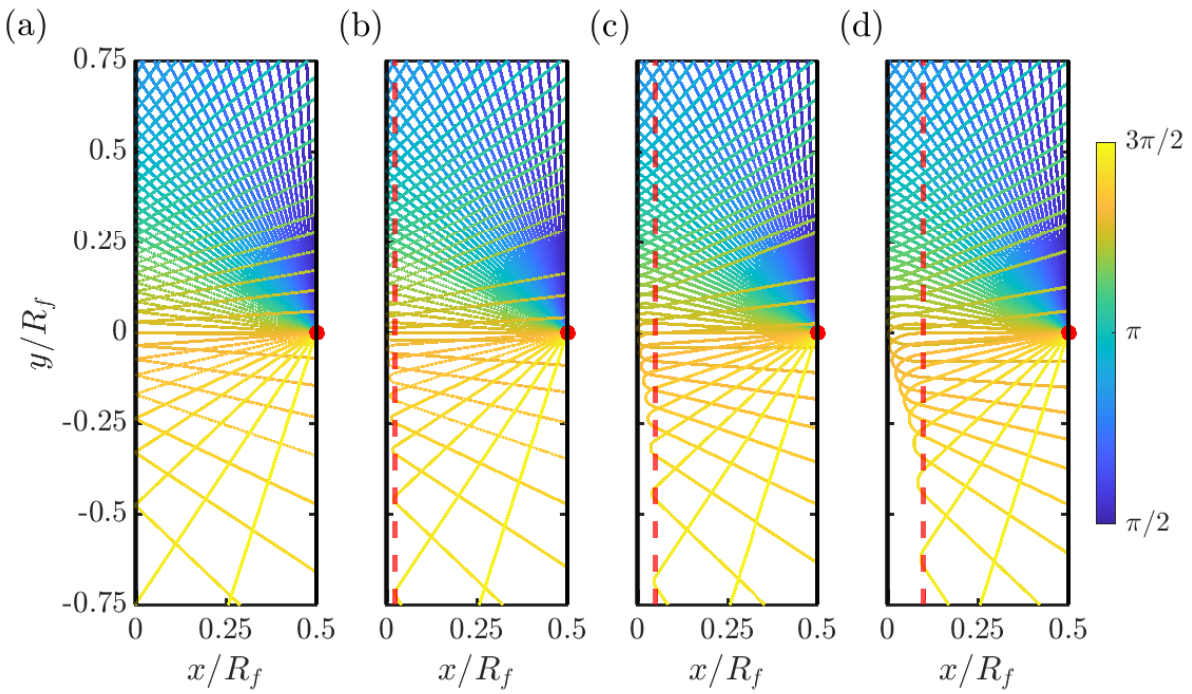

Figure 5.12: Acoustic ray trajectories in the presence of a laminar flow $v(x)$ for varying boundary layer thicknesses: (a) $\delta/R_f = 0$; (b) $\delta/R_f = 0.025$; (c) $\delta/R_f = 0.05$; (d) $\delta/R_f = 0.1$. The red dashed line denotes the location $x = \delta/R_f$; the red bullet represents the source.

The formulation is now extended to a three-dimensional configuration representative of the application case, with a cylindrical geometry. Let (x, y, z) denote Cartesian coordinates, with an infinite cylinder of radius R aligned with the z-axis. The mean flow is parallel to z and the velocity varies radially due to the presence of a boundary layer around the cylinder. The radial coordinate is defined as $r = \sqrt{x^2 + y^2}$, and the mean velocity field is $\boldsymbol{U}(r) = \big(0, 0, w(r)\big)$. The position vector is $\mathbf{x} = (x, y, z)$ and the wave vector is $\mathbf{k} = \big(k_x, k_y, k_z\big)$.

The ray equations system described in Eqs. (5.4-5.5) then become:

$$\frac{\mathrm{d}x}{\mathrm{d}t} = c\frac{k_x}{|\mathbf{k}|} \tag{5.11}$$

$$\frac{\mathrm{d}y}{\mathrm{d}t} = c\frac{k_y}{|\mathbf{k}|} \tag{5.12}$$

$$\frac{\mathrm{d}z}{\mathrm{d}t} = w(r) + c\frac{k_z}{|\mathbf{k}|} \tag{5.13}$$

$$\frac{\mathrm{d}k_x}{\mathrm{d}t} = -k_z\frac{\mathrm{d}w}{\mathrm{d}r}\frac{x}{r} \tag{5.14}$$

$$\frac{\mathrm{d}k_y}{\mathrm{d}t} = -k_z\frac{\mathrm{d}w}{\mathrm{d}r}\frac{y}{r} \tag{5.15}$$

$$\frac{\mathrm{d}k_z}{\mathrm{d}t} = 0 \tag{5.16}$$

In this case, the axial component k_z is conserved, while refraction occurs in the radial plane. Upstream-propagating waves ($k_z < 0$) are refracted outward, away from the cylinder surface. The boundary layer therefore acts as a refractive shield surrounding the cylinder. This geometric redistribution of acoustic energy leads to a decrease in the sound pressure level measured on the fuselage upstream of the rotor, since the ray density is lower.

Laminar boundary layer

A parametric study is conducted to assess the influence of boundary layer thickness δ on the fuselage SPL. In this case, δ is defined as the wall-normal distance at which the velocity reaches 95% of the free-stream velocity. The laminar boundary layer velocity profile around the fuselage is given by:

$$u(r) = u_0 \tanh\left[2\left(r - R_f\right)/\delta\right], \quad r \geq R_f \tag{5.17}$$

where u_0 is the mean flow, R_f is the fuselage radius, and $r = \sqrt{(z - z_f)^2 + (y - y_f)^2}$ is the distance from the center of the fuselage (z_f, y_f) in the yz-plane.

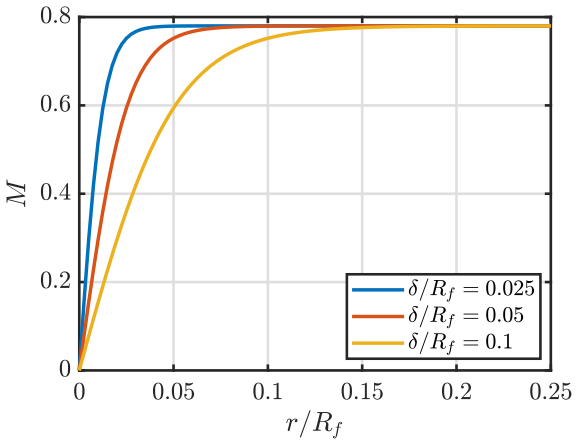

Figure 5.13: Laminar boundary-layer velocity profiles for different thicknesses δ/R_f.

Four simulations were carried out, each with a different boundary layer thickness $\delta/R_f \in [0, 0.1]$.

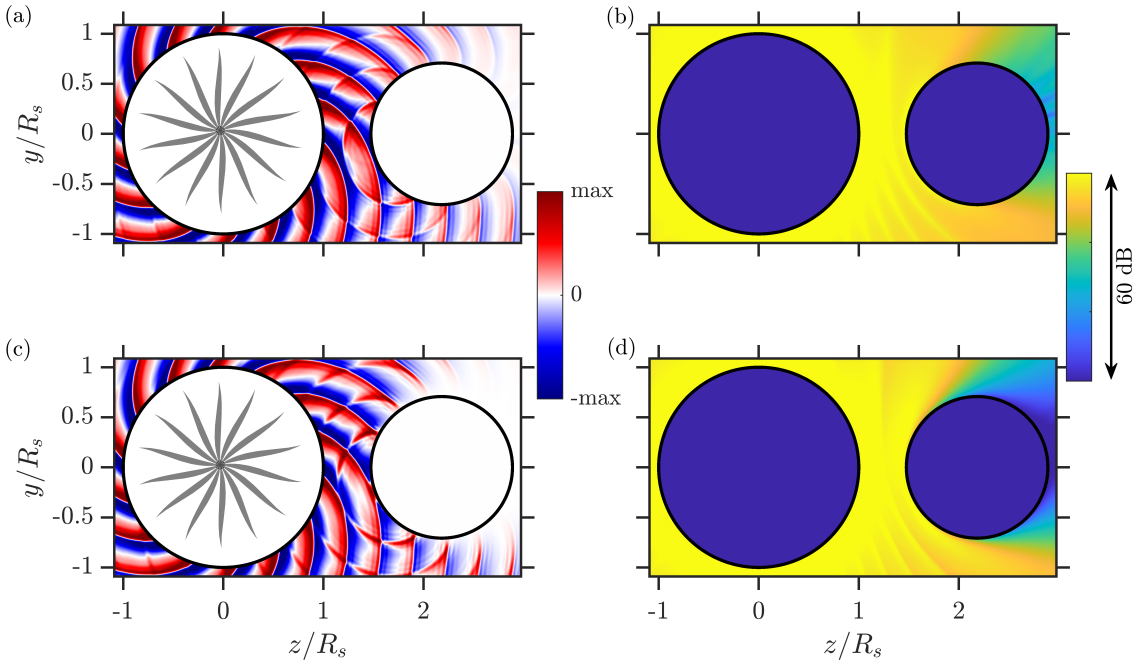

Figure 5.14: Snapshots of the acoustic pressure field on the left, and Sound Pressure Level on the right, for a laminar boundary layer, in the yz-plane at $x = 0$ for (a-b) $\delta/R_f = 0$ and (c-d) $\delta/R_f = 0.05$.

Figure 5.14 compares the case without a boundary layer to the case with a 0.1 m boundary layer thickness on the yz-plane at $x = 0$. The cylindrical control surface enclosing the unducted single fan engine, represented schematically, is positioned on the left side of the domain, while the fuselage is located on the right. Figures 5.14(a) and 5.14(c) show the instantaneous acoustic pressure field at the final iteration. The results indicate that the boundary layer increases the shadow zone for angles θ between 0 and $\pi/2$ and between $3\pi/2$ and 2π. The SPL distributions in Figs. 5.14(b) and 5.14(d) further show that the diffraction lobes are reduced in amplitude when the boundary layer is present. However, it is important to note that in a realistic configuration with two engines mounted on opposite sides of the fuselage, no true shadow zone exists. Consequently, the relevant region for this analysis corresponds to θ angles between approximately $\pi/2$ and $3\pi/2$, which represent the area directly exposed to the engine.

The distribution of acoustic pressure over the fuselage surface at the final iteration is presented in Fig. 5.15 for four boundary layer thickness configurations. In all cases, the acoustic pressure reaches its maximum in the vicinity of the rotor plane, located on the yz plane at $x = 0$. The convective effects induced by the mean flow velocity cause an increase in the wavelength of the pressure signal propagating downstream of the engine, in the positive x direction, while the wavefronts are compressed in the upstream region, towards negative x values. Within the angular range $\theta \in [-\pi/2, \pi/2]$, the diffraction of the acoustic field around the cylindrical fuselage results in a reduction of the acoustic pressure level. Furthermore, a progressive attenuation

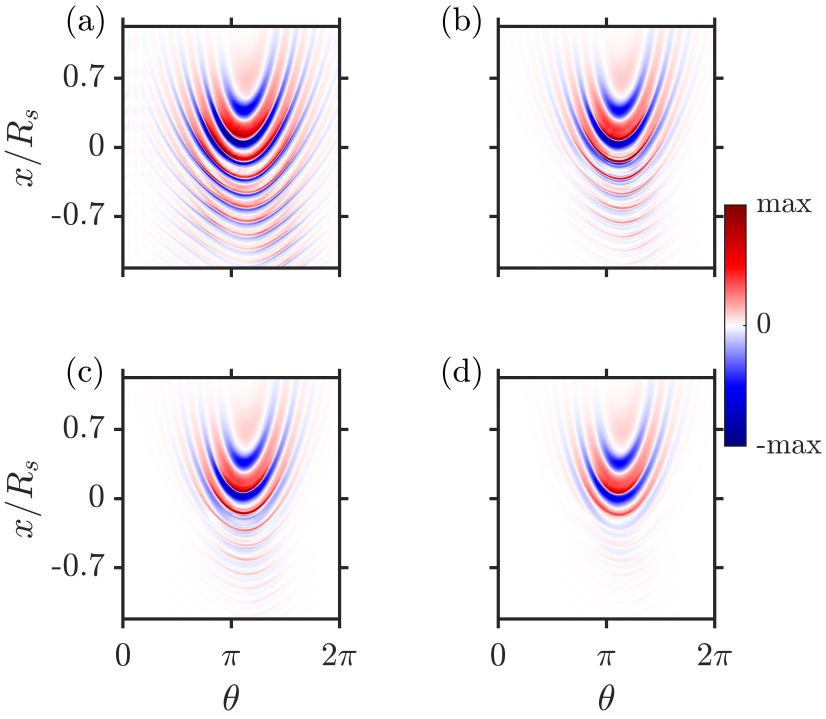

Figure 5.15: Acoustic pressure field on the fuselage at the final iteration for a laminar boundary layer with (a) $\delta/R_f = 0$, (b) $\delta/R_f = 0.025$, (c) $\delta/R_f = 0.05$, and (d) $\delta/R_f = 0.1$.

of the acoustic signature is observed with increasing boundary layer thickness, particularly in the upstream region of the engine. In contrast, the downstream region, in the vicinity of $\theta = \pi$, exhibits a comparatively weaker sensitivity to boundary layer effects. This behaviour is consistent with the results obtained using the ray-tracing method.

The SPL distribution around the fuselage for all the simulations is shown in Fig. 5.16. As the boundary layer thickness δ increases from Fig. 5.16(a) to Fig. 5.16(d), the SPL progressively decreases, particularly in the upstream region at negative x. The diffraction lobes near $\theta = 0$ also vanish upstream for thickness $\delta/R_f \geq 0.025$, as illustrated in Figs. 5.16(b-d). The shielding effect is strongest for $\delta/R_f = 0.1$, where most of the SPL is concentrated around $\theta = \pi$, corresponding to the region directly exposed to the acoustic waves.

The quantity ΔSPL_{BL} is now defined as:

$$\Delta\text{SPL}_{BL} = \text{SPL}_{\delta} - \text{SPL}_{\delta=0} \tag{5.18}$$

where SPL_{δ} and $\text{SPL}_{\delta=0}$ are the SPL with and without boundary layer, respectively.

A detailed comparison of the SPL for different boundary layer thicknesses δ is presented in Fig. 5.17. Figure 5.17(a) shows the SPL distribution along the x-direction at $\theta = \pi$, while Fig. 5.17(b) reports the corresponding values of ΔSPL_{BL} at the same locations. Upstream of the engine, at negative x, a reduction in SPL is observed, which becomes more pronounced with increasing boundary layer thickness. At $x/R_s = -1.17$, the reduction increases from -10 dB for

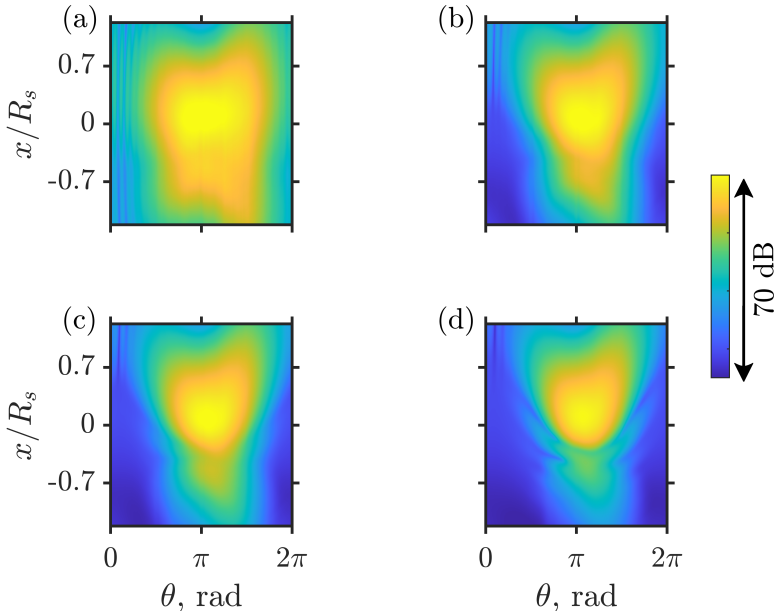

Figure 5.16: Sound Pressure Level on the fuselage for a laminar boundary layer with (a) $\delta/R_f = 0$, (b) $\delta/R_f = 0.025$, (c) $\delta/R_f = 0.05$, and (d) $\delta/R_f = 0.1$.

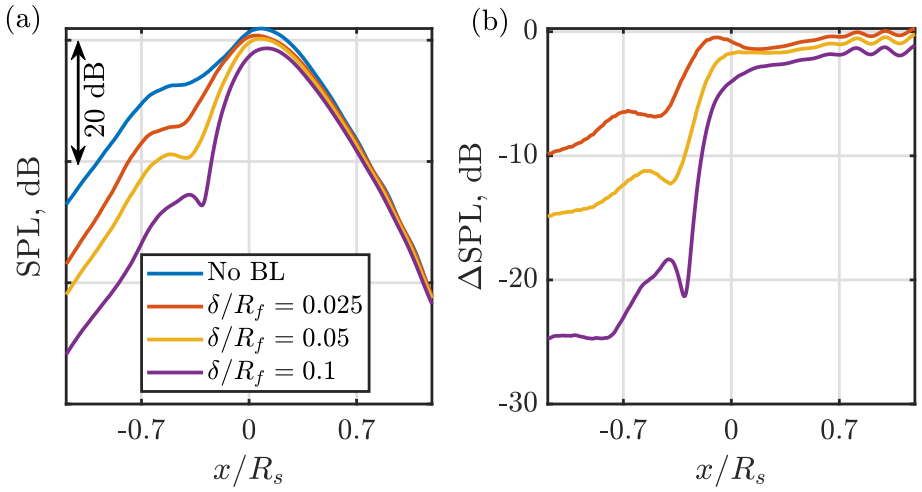

Figure 5.17: (a) Sound Pressure Level and (b) difference in Sound Pressure Level ΔSPL_{BL} on the fuselage along the x-coordinate at $\theta = \pi$ for a laminar boundary layer.

$\delta/R_f = 0.025$ to -25 dB for $\delta/R_f = 0.1$. Downstream of the engine, at positive x, the shielding effect is weaker, with a maximum SPL reduction of approximately -3 dB for $\delta/R_f = 0.1$.

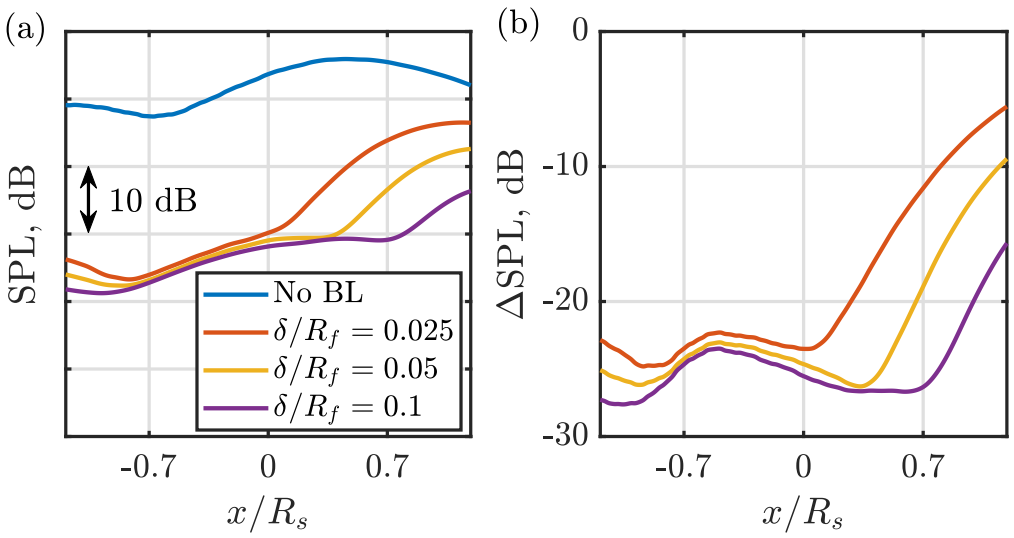

Figure 5.18: (a) Sound Pressure Level and (b) difference in Sound Pressure Level ΔSPL_{BL} on the fuselage along the x-coordinate at $\theta = 0$ for a laminar boundary layer.

A similar trend is observed for the SPL along x in the shadow zone at $\theta = 0$, as shown in Fig. 5.18. The shielding effect is evident upstream of the engine even for $\delta/R_f = 0.025$, with a minimum reduction of -6 dB. This occurs because acoustic waves must travel a longer path around the fuselage in the presence of a velocity gradient to reach the shadow zone, which enhances diffraction effects even for small boundary layer thicknesses δ. In this case, the downstream reduction is also similar to the angular position $\theta = \pi$, reaching up to a minimum of -27.5 dB for $\delta = 0.1$.

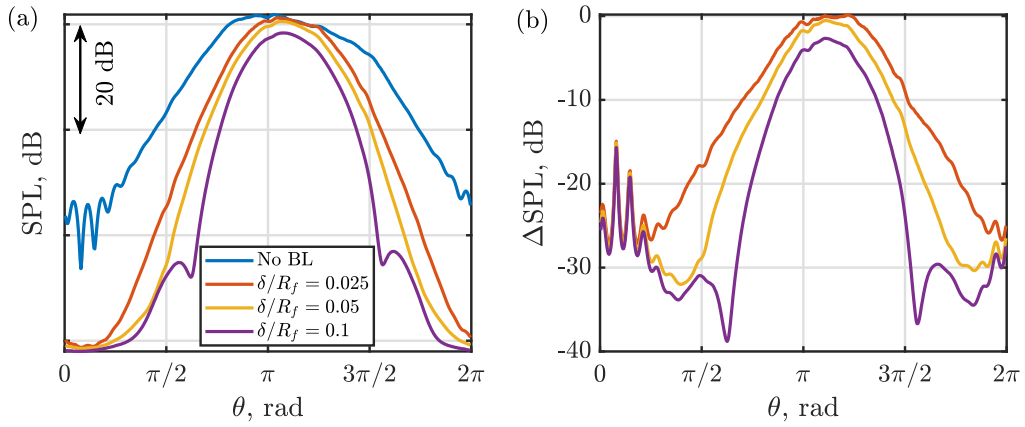

Figure 5.19: (a) Sound Pressure Level and (b) difference in Sound Pressure Level ΔSPL_{BL} on the fuselage along the θ-coordinate at $x = 0$ for a laminar boundary layer.

The SPL distribution on the fuselage along θ in the rotor plane at $x = 0$ is given in Fig. 5.19. In Fig. 5.19(a), the maximum SPL occurs near $\theta = \pi$ and decreases symmetrically on both sides. As the boundary layer thickness δ increases, the peak level decreases and the distribution narrows

around $\theta = \pi$. Strong oscillations are observed for $0 < \theta < \pi/4$, corresponding to diffraction lobes, which disappear for $\delta/R_f \geq 0.025$. Figure 5.19(b) plots the quantity ΔSPL_{BL}, showing that the reduction due to the boundary layer thickness δ is more pronounced in the shadow zone, specifically for $0 < \theta < \pi/2$ and $3\pi/2 < \theta < 2\pi$.

Turbulent boundary layer

In this case, the boundary layer is prescribed using a semi-empirical model of a turbulent boundary layer, assuming statistically steady conditions and spatial uniformity along the fuselage axis. The boundary layer is therefore considered fully developed, with the mean velocity profile depending solely on the wall-normal coordinate expressed in wall units r^+. The model is formulated under the assumption of zero pressure gradient.
The mean velocity is expressed in non-dimensional form as

$$U(r^+) = \frac{u(r)}{u_\tau} \tag{5.19}$$

where u_τ denotes the friction velocity and r^+ is the wall-normal coordinate in viscous units, defined as

$$r^+ = \frac{r u_\tau}{\nu} \tag{5.20}$$

The boundary-layer thickness δ is defined as the distance from the wall at which the mean velocity reaches the free-stream value u_0. The reference Reynolds number is accordingly defined as

$$Re^+ = \frac{u_\tau \delta}{\nu} \tag{5.21}$$

with ν denoting the kinematic viscosity of the fluid.
The velocity profile is obtained by solving the ordinary differential equation

$$\frac{\mathrm{d}U}{\mathrm{d}r^+} = \frac{2\tau(r^+)}{1 + \sqrt{1 + \left(2\ell_m(r^+)\right)^2 \tau(r^+)}} \tag{5.22}$$

where $\tau(r^+)$ represents the normalized total shear-stress distribution across the boundary layer. In the absence of a pressure gradient, it is modeled as

$$\tau(r^+) = 1 - 3\left(\frac{r^+}{Re^+}\right)^2 - 2\left(\frac{r^+}{Re^+}\right)^3 \tag{5.23}$$

which ensures that the shear stress vanishes at the boundary-layer edge.
The mixing length ℓ_m is defined through a formulation that smoothly connects the inner and

outer regions of the boundary layer. In the inner region, the mixing length is given by

$$\ell_{m,\text{inner}} = \kappa r^+ \left[1 - \exp\left(-\frac{r^+}{A_0}\right)\right] \tag{5.24}$$

where $\kappa = 0.41$ is the von Kármán constant and $A_0 = 26$ is the Van Driest [94] damping constant. In the outer region, the mixing length is limited to a maximum value

$$\ell_{m,\text{outer}} = A_w Re^+ \tag{5.25}$$

with $A_w = 0.085$ being an empirical constant. The overall mixing length is finally obtained through the relation

$$\ell_m = \ell_{m,\text{outer}} \tanh\left(\frac{\ell_{m,\text{inner}}}{\ell_{m,\text{outer}}}\right) \tag{5.26}$$

which ensures a smooth and continuous transition between the inner and outer regions.
The velocity profiles of the turbulent boundary layer employed in the simulations are presented in Fig. 5.20. For all three selected boundary layer thicknesses, the model predicts a nearly vertical velocity gradient up to $M = 0.5$ in the region immediately adjacent to the wall. This near-wall viscous region, characterized by a high velocity gradient, is very small relative to the wavelength of the case considered and therefore has a negligible influence on boundary-layer-induced diffraction effects. In contrast, the subsequent region, where the velocity gradient decreases progressively, contributes more significantly to diffraction phenomena. This region extends over a larger spatial range, corresponding approximately to the boundary layer thickness.
The resulting velocity profile is used as the initial condition in the simulations and, in the absence of mechanisms leading to temporal or spatial evolution of the mean flow, remains unchanged throughout the computation.

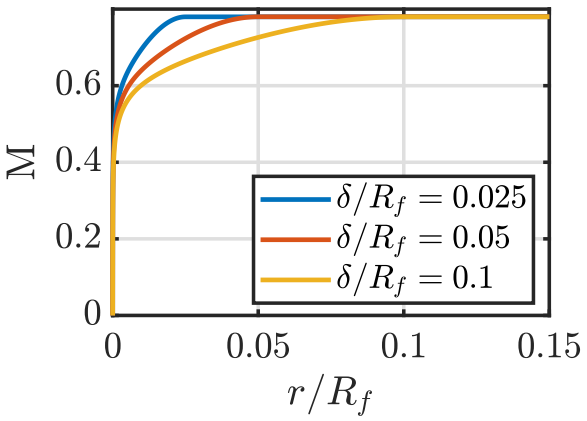

Figure 5.20: Turbulent boundary layer velocity profiles for different thicknesses δ.

The distribution of the acoustic pressure field on the fuselage surface in the presence of a turbulent boundary layer is presented in Fig. 5.21. The results exhibit a behaviour analogous to that

observed in the laminar boundary layer case, though with less pronounced effects. A reduction in the acoustic pressure level is observed with increasing boundary layer thickness, with the attenuation being most significant in the upstream region of the engine, towards negative x values.

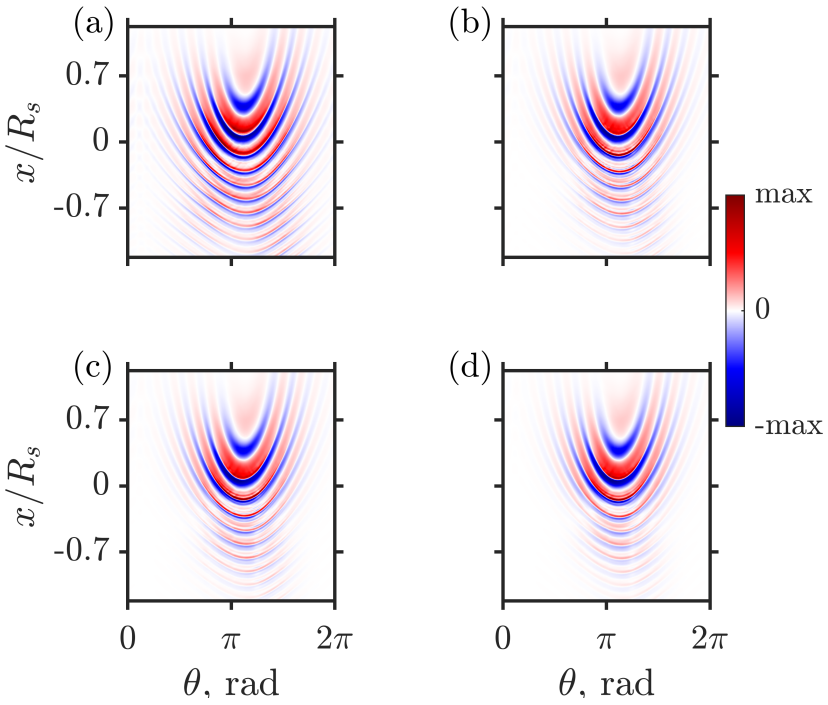

Figure 5.21: Acoustic pressure field on the fuselage at the final iteration for a turbulent boundary layer with (a) $\delta/R_f = 0$, (b) $\delta/R_f = 0.025$, (c) $\delta/R_f = 0.05$, and (d) $\delta/R_f = 0.1$.

The SPL distribution on the fuselage surface for different boundary layer thicknesses is presented in Fig. 5.22, ranging from $\delta/R_f = 0$ in Fig. 5.22(a) to $\delta/R_f = 0.1$ in Fig. 5.22(d). Consistent with the previously analyzed laminar boundary layer case, an increase in boundary layer thickness in the turbulent regime leads to a reduction in SPL. This reduction is more pronounced upstream of the rotor and less evident downstream. The maximum SPL occurs at $\theta = \pi$ on the rotor plane at $x = 0$.

A detailed comparison of the SPL distribution along the fuselage x-axis at $\theta = \pi$ is provided in Fig. 5.23(a). The SPL attains its maximum near $x = 0$ on the rotor plane, and this peak decreases with increasing boundary layer thickness. Upstream of the rotor, the SPL reduction becomes progressively more significant as the boundary layer thickens, whereas the effect remains comparatively weaker in the downstream region. As shown in Fig. 5.23(b), the reduction reaches -8 dB for a turbulent boundary layer with a thickness of $\delta/R_f = 0.1$, which is substantially smaller than in the corresponding laminar boundary layer case, where a reduction of -25 dB is observed. This difference is attributed to the turbulent boundary layer velocity profile, which exhibits a very steep gradient in the region immediately adjacent to the fuselage wall, increasing from $M = 0$ at the wall to $M = 0.5$ at the neighboring mesh point in the simulation. The spatial

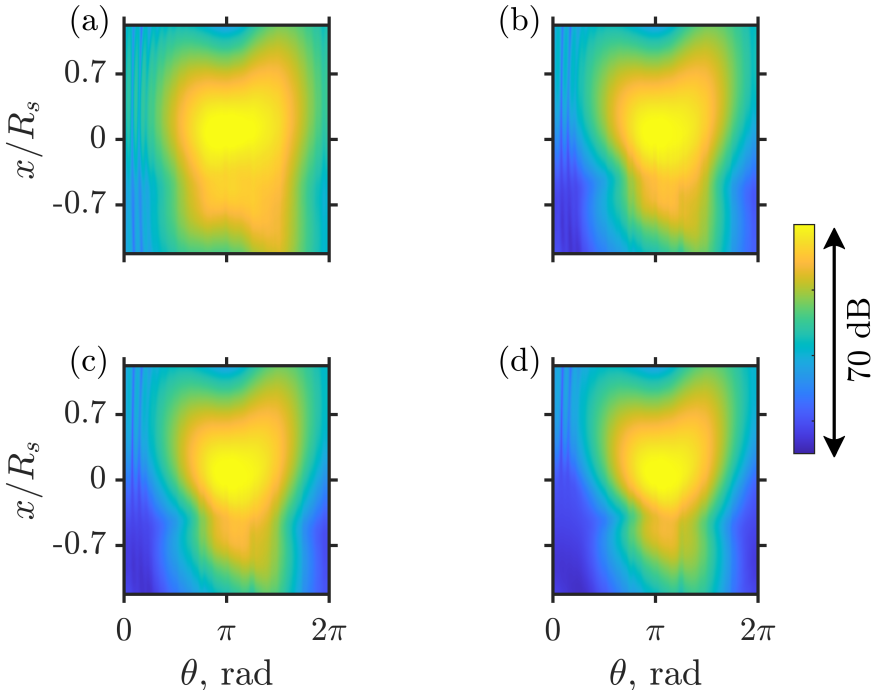

Figure 5.22: Sound Pressure Level on the fuselage for a turbulent boundary layer with (a) $\delta/R_f = 0$, (b) $\delta/R_f = 0.025$, (c) $\delta/R_f = 0.05$, (d) $\delta/R_f = 0.1$.

extent of this high–velocity-gradient region is much smaller than the acoustic wavelength of the case considered, which substantially reduces the shielding effect of the turbulent boundary layer relative to that of the laminar boundary layer.

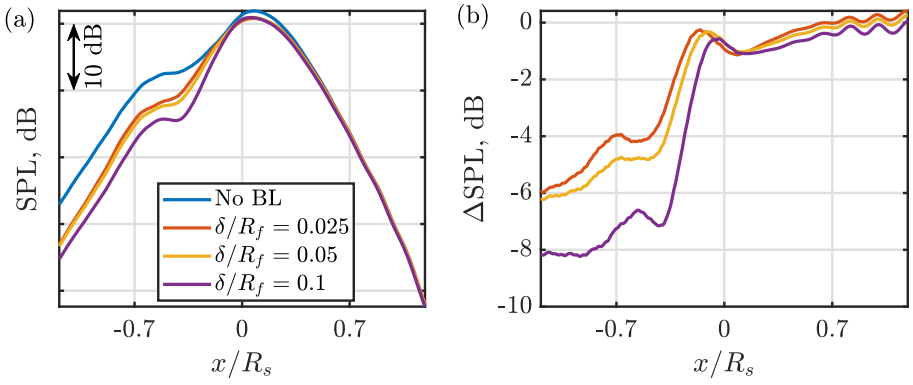

Figure 5.23: (a) Sound Pressure Level and (b) difference in Sound Pressure Level ΔSPL_{BL} on the fuselage along the $x-$coordinate at $\theta = \pi$ for a turbulent boundary layer.

The SPL distribution along the x-axis in the shadow region at $\theta = 0$ is shown in Fig. 5.24(a) for different boundary layer thicknesses. Overall, a behavior similar to that observed in the region directly exposed to the rotor is identified, with a more significant SPL reduction upstream than downstream. However, the downstream reduction is more pronounced than that observed at the angular position $\theta = \pi$. This difference arises because acoustic waves travel a longer

path around the fuselage to reach the shadow region, remaining within the boundary layer for a longer distance and experiencing stronger diffraction effects. The quantity ΔSPL_{BL} is plotted in Fig. 5.24(b), showing a maximum SPL reduction ranging from -18 dB for $\delta/R_f = 0.025$ to -22 dB for $\delta/R_f = 0.1$.

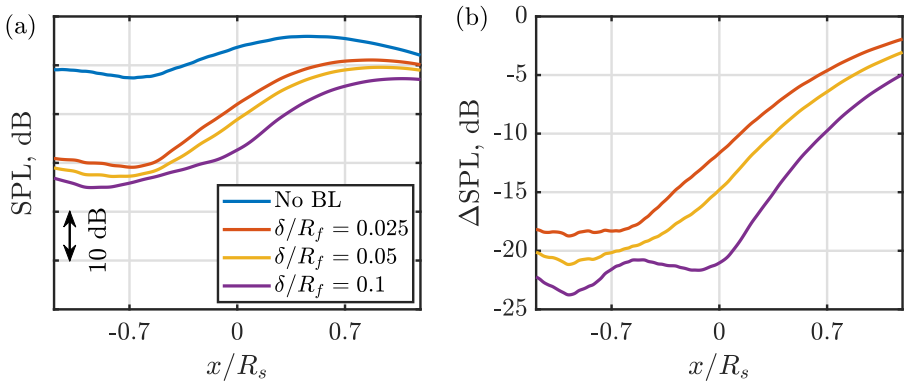

Figure 5.24: (a) Sound Pressure Level and (b) difference in Sound Pressure Level ΔSPL_{BL} on the fuselage along the x-coordinate at $\theta = 0$ for a turbulent boundary layer.

The SPL distribution as a function of the angular position θ on the rotor plane at $x = 0$ is shown in Fig. 5.25(a). Once again, the maximum peak occurs near $\theta = \pi$, with a symmetric decay on either side of this peak. This decay is accompanied by a progressive narrowing of the curve around the maximum. The oscillations observed near $\theta = 0$ correspond to diffraction lobes in the shadow region of the cylinder; these lobes vanish for $\delta/R_f = 0.1$. The quantity ΔSPL_{BL} is plotted in Fig. 5.25(b). The SPL reduction is less pronounced at $\theta = \pi$, as this location corresponds to the region of direct acoustic wave incidence, where the propagation path is minimal. The reduction becomes increasingly significant with increasing angular distance from the impact point, as the acoustic waves travel a longer path around the cylinder and diffraction effects progressively intensify. The maximum reduction increases from -12 dB for $\delta/R_f = 0.025$ to -25 dB for $\delta/R_f = 0.1$.

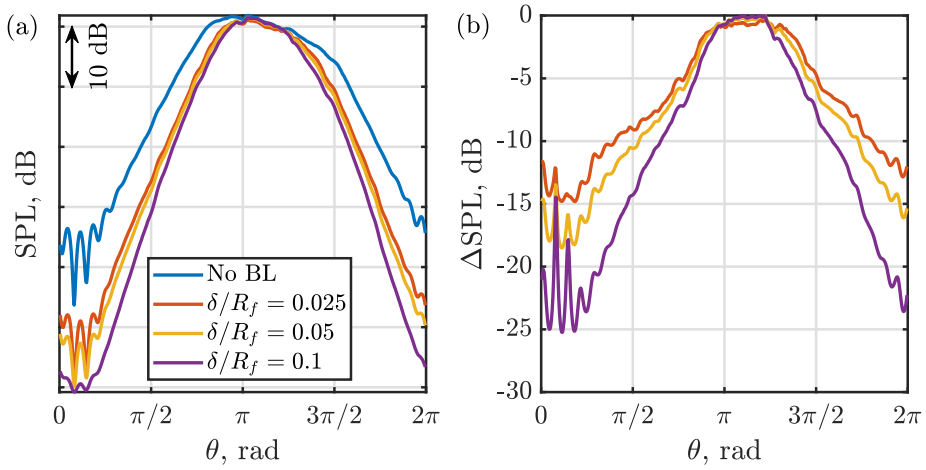

Figure 5.25: (a) Sound Pressure Level and (b) difference in Sound Pressure Level ΔSPL_{BL} on the fuselage along the θ-coordinate at $x = 0$ for a turbulent boundary layer.

Shielding coefficient

The surface sound pressure levels computed on the fuselage for both laminar and turbulent boundary layers of varying thickness indicate that the acoustic shielding effect is more pronounced in the laminar regime. To quantify this noise attenuation, an acoustic shielding coefficient S is introduced, defined as a function of the surface-averaged sound pressure levels obtained with and without a boundary layer. Following the formulation proposed by Gaffney *et al.* [95, 96], the shielding coefficient is expressed as a ratio of surface integrals:

$$S = \frac{\int_A \bar{p^2}_{\text{bl}}\,\mathrm{d}A}{\int_A \bar{p^2}\,\mathrm{d}A} \approx \frac{\sum_N \bar{p^2}_{\text{bl}}}{\sum_N \bar{p^2}} \tag{5.27}$$

where $\bar{p^2}_{\text{bl}}$ and $\bar{p^2}$ denote the mean square pressure in the presence and in the absence of a boundary layer, respectively, and $\mathrm{d}A$ is an infinitesimal surface element on the fuselage. The surface integrals can be approximated by summing the mean square pressure over all N grid elements comprising the fuselage surface. By construction, the coefficient $S \in [0, 1]$, where a value of 0 corresponds to total acoustic shielding and a value of 1 indicates the complete absence of a shielding effect.

The shielding coefficients S for laminar and turbulent boundary layers of varying thickness are shown in Fig. 5.26(a). The acoustic shielding effect is more pronounced in the laminar case than in the turbulent case, with the difference between the two coefficients increasing with boundary layer thickness. For $\delta/R_f = 0.1$, the coefficient S takes values of 0.25 and 0.55 for the laminar and turbulent cases, respectively.

Figure 5.26(b) presents the coefficients S^- and S^+, computed from Eq. (5.27) restricted to the upstream region ($x < 0$) and the downstream region ($x > 0$), respectively, thereby enabling a distinction between the shielding contributions upstream and downstream of the rotor. In both

the laminar and turbulent cases, the shielding effect is found to be greater upstream of the rotor than downstream, a result consistent with the trends previously observed in the sound pressure level distributions.

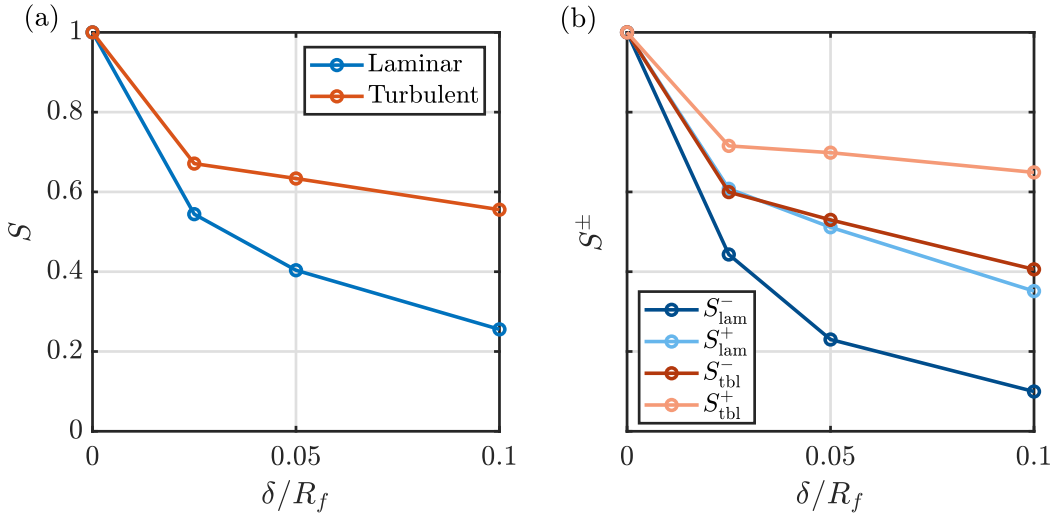

Figure 5.26: Shielding coefficient for laminar and turbulent boundary layer (a) over the entire fuselage surface, and (b) exclusively downstream (S^+) or upstream (S^-) of the rotor plane.

5.5 Conclusion

This chapter presents a comprehensive numerical investigation of the acoustic loading induced on an aircraft fuselage by an unducted single fan engine, with particular emphasis on non-linear shock wave propagation and the shielding effect of the fuselage boundary layer. The non-linear Euler equations were solved using source terms derived from a RANS simulation, providing a robust framework for assessing installation effects under cruise conditions. The methodology was validated against the Ffowcs Williams–Hawkings integral formulation, confirming the accuracy of the Euler-based approach while demonstrating its ability to capture non-linear phenomena that are not represented in conventional acoustic analogies.

The results indicate that non-linear effects are present, most notably for acoustic waves propagating upstream against the mean flow; however, their influence on the sound pressure level at the fuselage surface remains limited, with a maximum reduction of 1.6 dB. For waves propagating downstream with the flow, non-linear effects are negligible. These findings address the research objective of evaluating the relevance of non-linear formulations for unducted single fan noise prediction and suggest that linear models can provide a reasonable approximation over large regions of the fuselage, albeit with a slight overestimation of upstream noise levels.

The study identifies sound wave refraction by the fuselage boundary layer as the dominant mechanism governing the acoustic load. A parametric analysis of boundary layer thickness

demonstrates a monotonic increase in shielding effectiveness with increasing thickness, with the strongest attenuation observed in upstream and shadow regions. A key contribution of this chapter is the differentiation between laminar and turbulent boundary layer profiles. The results show that laminar boundary layers yield substantially greater shielding, with reductions of up to 40 dB in localized regions, compared with turbulent profiles. This disparity is attributed to the smoother near-wall velocity gradients in laminar boundary layers relative to the acoustic wavelength, which enhance refraction effects, whereas the steeper gradients in turbulent boundary layers significantly reduce shielding effectiveness.

Overall, this chapter advances the understanding of an unducted single fan and airframe acoustic interactions by demonstrating that boundary layer properties exert a substantially greater influence on the fuselage acoustic signature than non-linear propagation effects.

7 Conclusion

General synthesis of the thesis

The objective of this research work was to develop and validate a high-fidelity numerical framework to predict the acoustic signature on the fuselage. This required addressing two primary scientific and methodological gaps: the need for robust CFD/CAA coupling capable of injecting signals into a non-linear solver without generating spurious reflections, and the development of efficient boundary modeling for rigid obstacles within Cartesian grids to assess installation effects, specifically the role of the fuselage boundary layer in refracting and shielding acoustic energy.

This research has produced several original scientific and methodological contributions to the field of computational aeroacoustics through the development and application of an integrated numerical framework. A three-dimensional non-linear Euler solver was implemented using high-order, low-dispersion, and low-dissipation schemes, combined with a dedicated shock-capturing strategy based on WENO smoothness indicators. This approach proved essential for accurately resolving the sharp gradients associated with rotating shock waves while ensuring numerical stability in the presence of a mean flow.

Within this framework, an original volumetric source method was developed to prescribe incoming acoustic fields through source terms distributed along an arbitrary control surface. This technique enables one-way wave injection while effectively suppressing backward-propagating disturbances. Its flexibility allows acoustic signals extracted from independent RANS simulations to be introduced into a uniform Cartesian mesh without requiring conformity between the source surface and the computational grid. The results demonstrate high robustness across academic cases, such as oblique waves, N-waves, and monopole in a uniform flow. The validation of the proposed method against the Ffowcs Williams-Hawkings integral formulation confirmed its accuracy for the application case.

Furthermore, a novel reflection method was formulated to model perfectly rigid immersed boundaries by introducing forcing terms in the momentum conservation equations. These sources are applied at the obstacle surface on the basis of instantaneous wall pressure measurements, allowing full acoustic wave reflection to be achieved without the geometric complexity or computational cost associated with body-fitted curvilinear meshes. While the reflection method

achieves second-order accuracy when the mesh conforms to the geometry, it reduces to first-order accuracy for immersed boundaries due to the limitations of bilinear interpolation.

The combination of these numerical developments enabled a comprehensive assessment of non-linear propagation and installation effects on an unducted single fan acoustic signatures on the fuselage. The results demonstrate that, although non-linear effects produce a modest reduction in sound pressure level for waves propagating upstream against the mean flow, the refraction of sound waves by the fuselage boundary layer is the dominant mechanism governing the acoustic levels perceived at the airframe.

A key finding is the regime-dependent behavior of the boundary layer shielding. The study identified a monotonic increase in shielding effectiveness as the boundary layer thickens. Furthermore, laminar profiles were found to provide substantially greater attenuation than turbulent profiles. This highlights the critical importance of selecting representative velocity profiles when predicting noise in an installed environment. The boundary layer effects were evaluated using prescribed steady velocity profiles. In realistic flight conditions, unsteady turbulent fluctuations in the boundary layer can lead to scattering and spectral haystacking, which were not modeled in the present work.

Future work

Future research should build upon the numerical framework developed in this thesis by extending both its physical fidelity and its applicability to more realistic aircraft configurations. While the present work has focused on an unducted single fan installation interacting with an idealized fuselage geometry, a natural progression would be the simulation of a complete aircraft configuration featuring two symmetrically mounted unducted single fans. Such an extension would enable the prediction of the full fuselage acoustic signature, accounting for interference effects between multiple sources and for asymmetric propagation phenomena that cannot be captured in isolated-engine configurations.

Additional realism could be introduced through a more representative modeling of the fuselage geometry. Replacing the canonical cylindrical shape with a geometry closer to that of an actual aircraft would allow curvature effects, local variations in boundary layer development, and geometric scattering mechanisms to be more accurately captured. This extension would provide a more reliable assessment of installation effects and improve the relevance of the predictions for industrial design studies.

From a numerical standpoint, the current use of a uniform Cartesian grid could be enhanced by adopting a non-uniform Cartesian or locally refined mesh strategy. Targeted mesh refinement in regions of particular acoustic sensitivity, such as the vicinity of the volumetric source injection surface and the fuselage boundary layer, would improve spatial resolution while preserving the efficiency and simplicity of the Cartesian framework. Such an approach would also mitigate accuracy losses associated with immersed boundary treatments without resorting to fully body-fitted grids.

Further improvements are also required in the modeling of the fuselage boundary layer. In the present study, shielding effects were evaluated using prescribed steady velocity profiles. In realistic flight conditions, however, the boundary layer is inherently unsteady and turbulent, and its temporal fluctuations can induce additional scattering mechanisms and spectral broadening, commonly referred to as haystacking. Incorporating a time-evolving turbulent boundary layer model, either through synthetic turbulence or through coupling with higher-fidelity flow solvers, would represent a significant step toward more accurate noise predictions.

More broadly, the tools developed in this thesis provide a flexible platform for investigating a wide range of installation effects relevant to future unducted propulsion systems. Their application to increasingly complex configurations and flow conditions offers a clear path toward bridging the gap between high-fidelity aeroacoustic simulation and realistic aircraft noise assessment.

Acknowledgments

This material is based upon work supported by the ANRT (Association nationale de la recherche et de la technologie) with a CIFRE fellowship granted to Giovanni Coco. The study was performed within the framework of the industrial chair ARENA (ANR-18-CHIN-0004-01) co-financed by Safran Aircraft Engines and the French National Research Agency (ANR), and within the framework of the LABEX CeLyA (ANR-10-LABX-0060) of Université de Lyon, within the program "Investissements d'Avenir" (ANR-16- IDEX-0005) operated by the French National Research Agency (ANR). This work was granted access to the HPC resources of PMCS2I (Pôle de Modélisation et de Calcul en Sciences de l'Ingénieur de l'Information) of the École Centrale de Lyon, Écully, France.

A Convolution

The calculation of the convolution in Eq. (3.60) is detailed below. Complex notation is used to simplify the calculations. The convolution writes explicitly as:

$$p'(x,y,t) = \iiiint_{-\infty}^{+\infty} g_0(x-x', y-y', z-z', t-t') S(x',y',t') \, \mathrm{d}x' \mathrm{d}y' \mathrm{d}z' \mathrm{d}t' \tag{A.1}$$

where g_0 is the Green function in free field:

$$g_0(x,y,z,t) = \frac{1}{4\pi R} \delta\left(t - R/c_0\right). \tag{A.2}$$

with $R = \sqrt{x^2+y^2+z^2}$. The term S is given by $S = S_1 + S_2$ with:

$$S_1 \coloneqq \frac{\partial \Lambda_\rho}{\partial t} = -\mathrm{i}k_x A \exp\left(-\mathrm{i}\omega t + \mathrm{i}k_y y\right) \delta_b(x) \tag{A.3}$$

$$S_2 \coloneqq -\nabla \cdot \mathbf{\Lambda_{\rho u}} = -A \exp\left(-\mathrm{i}\omega t + \mathrm{i}k_y y\right) \delta_b'(x) \tag{A.4}$$

with $k_x = k_0 \cos\theta$ and $k_y = k_0 \sin\theta$. $\delta_b(x)$ is the normalized Gaussian distribution defined by Eq. (3.50) and $\delta_b'(x)$ is its derivative. For the sake of clarity, the integral is calculated by separating the two addends.

A.1 Calculation for S_1

The convolution between the Green's function g_0 and S_1 reads:

$$p_1(x,y,t) = \iiiint_{-\infty}^{+\infty} \frac{1}{4\pi R} \delta\left(t - t' - \frac{R}{c_0}\right) S_1(x',y',z',t') \, \mathrm{d}x' \, \mathrm{d}y' \, \mathrm{d}z' \, \mathrm{d}t'$$

The property of the Dirac distribution is used for integration over time by evaluating S_1 at $t' = t - R/c_0$:

$$p_1(x,y,t) = -A\frac{\mathrm{i}k_x}{\sqrt{\pi}b}\int_{-\infty}^{+\infty}\exp\left[-\frac{x'^2}{b^2}\right]\iint_{-\infty}^{+\infty}\frac{\exp\left(-\mathrm{i}\omega t+\mathrm{i}k_0R+\mathrm{i}k_y y'\right)}{4\pi R}\,\mathrm{d}y'\mathrm{d}z'\,\mathrm{d}x' \tag{A.5}$$

The resolution of the double integral is given in detail in Appendix A.4. Equation (A.17) is used and the integral reads:

$$p_1 = \frac{B}{2\sqrt{\pi}b}\int_{-\infty}^{+\infty}\exp\left[-\frac{x'^2}{b^2}\right]\exp\left(\mathrm{i}k_x\left|x-x'\right|\right)\,\mathrm{d}x' \tag{A.6}$$

with $B = A\exp\left(-\mathrm{i}\omega t+\mathrm{i}k_y y\right)$.
The assumption is made to be in the far field, i.e. $|x| \gg b$. At the first order, one obtains:

$$|x-x'| \approx |x|\left(1-\frac{x'}{x}\right) = |x| - x'\,\mathrm{sign}(x) \tag{A.7}$$

Equation (A.6) is then written as

$$p_1 = \frac{B}{2\sqrt{\pi}b}\exp\left(\mathrm{i}k_x|x|\right)\int_{-\infty}^{+\infty}\exp\left(-\frac{x'^2}{b^2}\right)\exp\left[-\mathrm{i}k_x x'\,\mathrm{sign}(x)\right]\mathrm{d}x' \tag{A.8}$$

The integral in the above equation corresponds to the Fourier transform of the Gaussian function, that is given by [97]:

$$\int_{-\infty}^{+\infty}\exp(-q^2x^2)\exp\left(\mathrm{i}px\right)\mathrm{d}x = \frac{\sqrt{\pi}}{q}\exp\left(-\frac{p^2}{4q^2}\right) \tag{A.9}$$

for p and q real numbers. Equation (A.9) is used in Eq. (A.8) leading to:

$$\begin{aligned} p_1 &= \frac{B}{2\sqrt{\pi}b}\exp\left(\mathrm{i}k_x|x|\right)\sqrt{\pi}b\exp\left(-\frac{k_x^2b^2}{4}\right) \\ &= \frac{A_b}{2}\exp\left(-\mathrm{i}\omega t+\mathrm{i}k_x|x|+\mathrm{i}k_y y\right) \end{aligned} \tag{A.10}$$

with:

$$A_b = A\exp\left(-\frac{k_x^2b^2}{4}\right) \tag{A.11}$$

A.2 Calculation for S_2

The convolution between the Green's function g_0 and S_2 reads:

$$p_2(x,y,t) = \frac{2A\exp\left(-i\omega t\right)}{\sqrt{\pi}b^3}\int_{-\infty}^{+\infty} x'\exp\left(-\frac{x'^2}{b^2}\right)\iint_{-\infty}^{+\infty}\frac{\exp\left(\mathrm{i}k_0R+\mathrm{i}k_y y'\right)}{4\pi R}\mathrm{d}x'\,\mathrm{d}y'\,\mathrm{d}z'$$

where the Dirac distribution property is used for the integration in time.
Once again, Eq. (A.17) is used to solve the double integral:

$$p_2 = C\int_{-\infty}^{+\infty} x'\exp\left(\mathrm{i}k_x|x-x'| - \frac{x'^2}{b^2}\right)\mathrm{d}x'$$

with $C = \mathrm{i}A\exp\left(-\mathrm{i}\omega t+\mathrm{i}k_y y\right)/(k_x\sqrt{\pi}b^3)$. The same first order approximation as in Eq. (A.7) is made:

$$p_2 = C\exp\left(\mathrm{i}k_x\,|x|\right)\int_{-\infty}^{+\infty} x'\exp\left(-\frac{x'^2}{b^2}\right)\exp\left(-\mathrm{i}k_x x'\mathrm{sign}\,(x)\right)\,\mathrm{d}x' \tag{A.12}$$

The integral above corresponds to the Fourier transform of the derivative of the Gaussian function. It can be written as:

$$\int_{-\infty}^{+\infty} x\exp(-q^2x^2)\exp(\mathrm{i}px)\,\mathrm{d}x = \frac{\mathrm{i}p}{2q^2}\frac{\sqrt{\pi}}{q}\exp\left(-\frac{p^2}{4q^2}\right)$$

for p and q real numbers. After appropriate simplifications, the pressure field generated by the source term S_2 is finally obtained:

$$p_2 = \frac{A_b}{2}\mathrm{sign}\,(x)\exp\left(-\mathrm{i}\omega t+\mathrm{i}k_x\,|x|+\mathrm{i}k_y y\right) \tag{A.13}$$

A.3 Total acoustic pressure field

The acoustic pressure field generated by S_1 and S_2 is calculated by the sum of Eqs. (A.10) and (A.13), i.e. $p' = p_1 + p_2$, yielding:

$$p'(x,y,t) = A_bH(x)\exp(-\mathrm{i}\omega t+\mathrm{i}k_x x+\mathrm{i}k_y y) \tag{A.14}$$

Taking the real part of the equation above leads to Eq. (3.60).

A.4 Integral calculation

In this appendix, we detail the calculation of the integral:

$$I(x,x',y) = \iint_{-\infty}^{+\infty}\frac{\exp\left(\mathrm{i}k_0R+\mathrm{i}k_y y'\right)}{4\pi R}\mathrm{d}y'\mathrm{d}z' \tag{A.15}$$

with $R = \sqrt{\rho^2+z'^2}$ and $\rho^2 = \left(x-x'\right)^2+\left(y-y'\right)^2$.

We first use the relation:

$$\int_{-\infty}^{+\infty} \frac{\exp\left(\mathrm{i}k_0 R\right)}{4\pi R}\mathrm{d}z' = \frac{\mathrm{i}}{4}H_0^{(1)}\left(k_0\rho\right)$$

where $H_0^{(1)}$ is the Hankel function of the first kind, which can be derived from Eqs. (3.714.2) and (3.714.3) in Gradshteyn and Ryzhik [97]. With this relation, Eq. (A.15) becomes:

$$I = D\int_{-\infty}^{+\infty} H_0^{(1)}\left(k_0\sqrt{\chi^2+y''^2}\right)\exp\left(-\mathrm{i}k_y y''\right)\mathrm{d}y''$$

with $D = \mathrm{i}\exp\left(\mathrm{i}k_y y\right)/4$, $\chi = x - x'$ and $y'' = y - y'$. By splitting the integral into $(-\infty; 0]$ and $[0; +\infty)$, it can be written as:

$$I = 2D\int_{0}^{+\infty} H_0^{(1)}\left(k_0\sqrt{\chi^2+y''^2}\right)\cos(k_y y'')\,\mathrm{d}y'' \tag{A.16}$$

Using Eqs. (6.677.3) and (6.677.4) in Gradshteyn and Ryzhik [97], it can be shown that:

$$\int_{0}^{+\infty} H_0^{(1)}\left(\alpha\sqrt{x^2+z^2}\right)\cos(\beta x)\,\mathrm{d}x = \frac{\exp\left(\mathrm{i}|z|\sqrt{\alpha^2-\beta^2}\right)}{\sqrt{\alpha^2-\beta^2}}$$

for $0 < \beta < \alpha$ and for z a real number. Using the above equation in Eq. (A.16) allows us to obtain:

$$I(x, x', y) = \frac{\mathrm{i}}{2k_x}\exp\left(\mathrm{i}k_x\left|x - x'\right| + \mathrm{i}k_y y\right) \tag{A.17}$$

B N-wave injection

This appendix presents an academic test case involving the injection of a single N-wave using the acoustic wave introduction method described in Chapter 3. The objective of this numerical simulation is to demonstrate the capability of the method to directly introduce shock waves with strong discontinuities.

An N-wave is characterized by an initial pressure peak Δp_0 and a positive phase length L_0, from which a characteristic time $\tau_N = L_0 \rho_0 c_0 / \beta \Delta p_0$ is defined. As shown by Pierce [41], the space–time evolution of an N-wave is given by:

$$p(x,t) = \frac{P(t)}{L(t)} \left(x - c_0 t\right) \tag{B.1}$$

for $-L(t) < x - c_0 t < L(t)$, with

$$P(t) = \frac{\Delta p_0}{\left(1 + t/\tau_N\right)^{1/2}} \tag{B.2}$$

$$L(t) = \left(1 + t/\tau_N\right)^{1/2} L_0 \tag{B.3}$$

As indicated by Eqs. (B.1-B.3), an N-wave retains its characteristic shape during propagation, with pressure peaks that decrease in amplitude and separate spatially as the wave travels.

The computational domain consists of 8001 grid points over a length of 100. The initial pressure peak of the N-wave is set to $\Delta p_0 = 0.3 p_0$, where p_0 denotes the ambient pressure, and the initial positive phase length is $L_0 = 5$. Perfectly matched layers are applied over 30 grid points at each boundary of the domain. The total simulation time is $T = 100$ s, with a Courant–Friedrichs–Lewy number of 0.5.

The space-time evolution of the N-wave in the computational domain is illustrated in Fig. B.1(a) at $t = 6.25$ s, Fig. B.1(b) at $t = 37.5$, and Fig. B.1(c) at $t = 87.5$. The N-wave is correctly introduced at $x = 0$ and propagates in the positive x-direction. The injection method remains effective in this academic test case, enabling the introduction of an N-wave with a strong discontinuity without inducing numerical oscillations. The numerical results show good agreement with the envelope of the analytical solution, accurately capturing both the progressive decay of

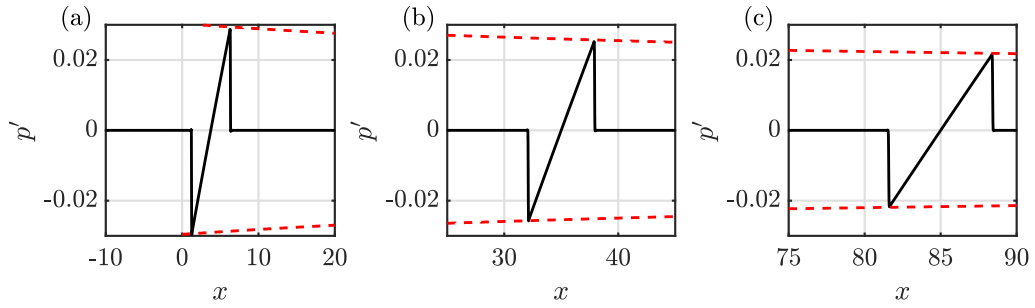

Figure B.1: Temporal evolution of the N-wave at three time instants: (a) $t = 6.25$, (b) $t = 37.5$, and (c) $t = 87.5$. Numerical results are shown by solid black lines (—), while the analytical envelope is indicated by red dashed lines (- -).

the pressure peaks and the increasing separation distance between them.

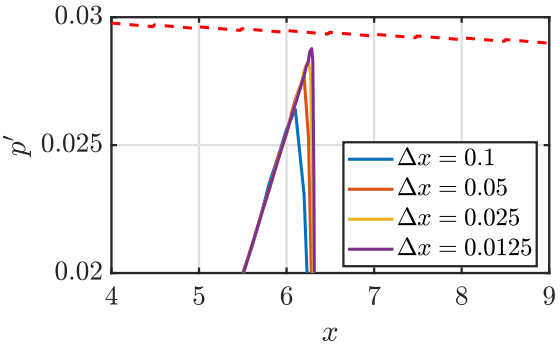

Figure B.2: Zoomed view of the positive peak of the N-wave at $t = 6.25$ for different mesh spacings Δx. The red dashed line (- -) denotes the envelope of the analytical solution.

Figure B.2 presents a zoomed view of the positive peak of the N-wave at $t = 6.25$ for different mesh spacings Δx. Progressive mesh refinement from $\Delta x = 0.1$ to $\Delta x = 0.0125$ improves the accuracy of the solution, with the numerical peak converging toward the analytical prediction. This behavior results from selecting the half-width of the Gaussian support as $b_w = \Delta x$, which renders the source increasingly compact as the mesh is refined.

C Integral calculation for the reflection method

C.1 Calculation of p_2 and p_3

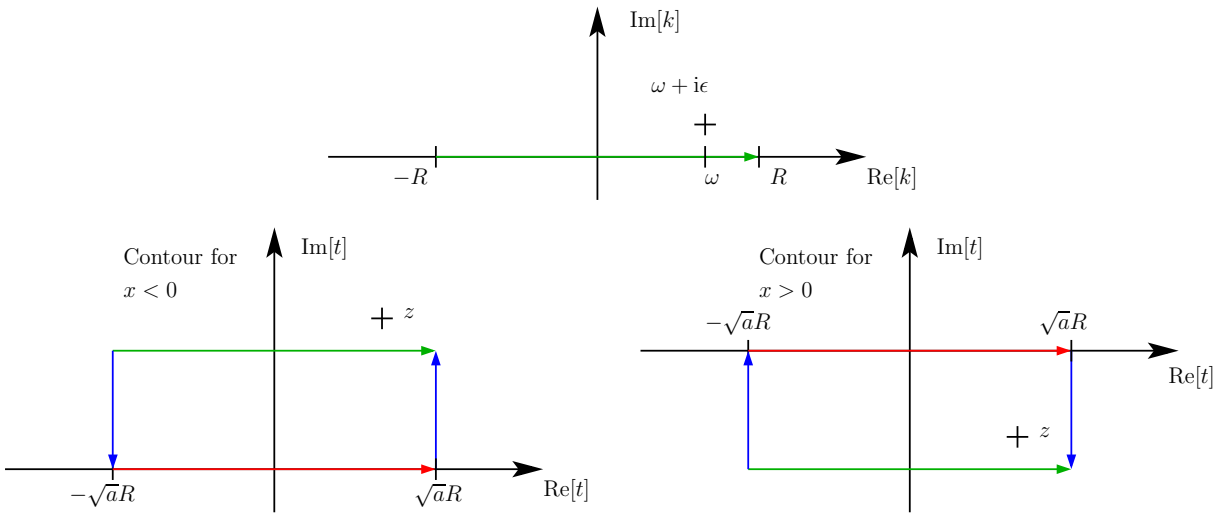

Figure C.1: Integration contour used to evaluate p_2.

Adding dissipation, Eq. (4.74) is recast as:

$$p_2 = -\frac{\mathrm{i}}{2\pi}\int_{-\infty}^{+\infty}\frac{\exp\left(\mathrm{i}kx - ak^2\right)}{k-\omega-\mathrm{i}\epsilon}\,\mathrm{d}k \tag{C.1}$$

with $a = b^2/4$. A change of variable is now made:

$$t = \sqrt{a}\left(k - \frac{\mathrm{i}x}{2a}\right) \Longleftrightarrow k = \frac{t}{\sqrt{a}} + \frac{\mathrm{i}x}{2a}, \quad \mathrm{d}k = \mathrm{d}t/\sqrt{a} \tag{C.2}$$

Equation (C.1) is then rewritten with the new variable t:

$$p_2 = -\frac{\mathrm{i}}{2\pi}\exp\left(-\frac{x^2}{4a}\right)\int_{-\infty-\frac{\mathrm{i}x}{2\sqrt{a}}}^{+\infty-\frac{\mathrm{i}x}{2\sqrt{a}}}\frac{\mathrm{e}^{-t^2}}{t-z}\,\mathrm{d}t \tag{C.3}$$

with $z = \sqrt{a}\omega - \mathrm{i}x/(2\sqrt{a}) + \mathrm{i}\epsilon\sqrt{a}$. In order to bring back the calculation to a known integral, we deform the contour as shown in Fig. C.1.

For $x < 0$, corresponding to $\Im(z) > 0$, the deformation is straightforward. This yields:

$$p_2 = -\frac{\mathrm{i}}{2\pi}\exp\left(-\frac{x^2}{4a}\right)\int_{-\infty}^{+\infty}\frac{\mathrm{e}^{-t^2}}{t-z}\,\mathrm{d}t = \frac{1}{2}w(z)\exp\left(-\frac{x^2}{4a}\right) \tag{C.4}$$

where Eq. (C.17) is used.

For $x > 0$, corresponding to $\Im(z) < 0$, the pole at $t = z$ lies within the integration contour and therefore contributes to the integral. This yields:

$$p_2 = -\frac{\mathrm{i}}{2\pi}\exp\left(-\frac{x^2}{4a}\right)\left(2\mathrm{i}\pi\mathrm{e}^{-z^2} + \int_{-\infty}^{+\infty}\frac{\mathrm{e}^{-t^2}}{t-z}\,\mathrm{d}t\right) = \frac{1}{2}\left[2\mathrm{e}^{-z^2} - w(-z)\right]\exp\left(-\frac{x^2}{4a}\right) \tag{C.5}$$

Note that $2\mathrm{e}^{-z^2} - w(-z) = \mathrm{e}^{-z^2}(2 - \mathrm{erfc}\,(\mathrm{i}z) = \mathrm{e}^{-z^2}\mathrm{erfc}\,(-\mathrm{i}z) = w(z)$. As a conclusion, for $x < 0$ or $x > 0$, one has:

$$p_2 = \frac{1}{2}w(z)\exp\left(-\frac{x^2}{4a}\right) = \frac{1}{2}\exp\left(-\frac{\omega^2 b^2}{4}\right)\exp\left(\mathrm{i}\omega x\right)\mathrm{erfc}\left(-\frac{x}{b} - \frac{\mathrm{i}\omega b}{2}\right) \tag{C.6}$$

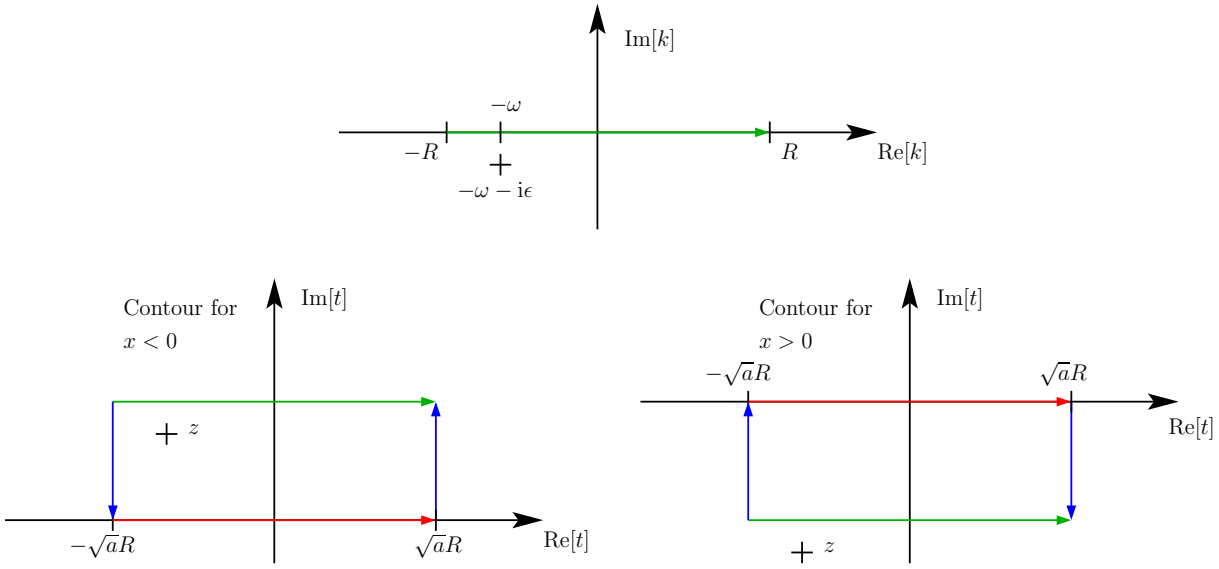

Figure C.2: Integration contour used to evaluate p_3.

Similarly, one can write:

$$p_3 = -\frac{\mathrm{i}}{2\pi}\int_{-\infty}^{+\infty}\frac{\exp\left(-\dfrac{k^2b^2}{4}\right)}{k+\omega+\mathrm{i}\epsilon}\,\mathrm{e}^{\mathrm{i}kx}\,\mathrm{d}k \tag{C.7}$$

After applying the same change of variable than for p_2, we obtain:

$$p_3 = -\frac{\mathrm{i}}{2\pi}\exp\left(-\frac{x^2}{4a}\right)\int_{-\infty-\frac{\mathrm{i}x}{2\sqrt{a}}}^{+\infty-\frac{\mathrm{i}x}{2\sqrt{a}}}\frac{\mathrm{e}^{-t^2}}{t-z}\,\mathrm{d}t \tag{C.8}$$

with $z = -\sqrt{a}\omega - \mathrm{i}x/(2\sqrt{a}) - \mathrm{i}\epsilon\sqrt{a}$. As for p_2, we deform the path of integration as indicated in Fig. C.2. For $x < 0$, corresponding to $\Im(z) > 0$, the pole at $t = z$ is crossed during the deformation. This yields:

$$p_3 = -\frac{\mathrm{i}}{2\pi}\exp\left(-\frac{x^2}{4a}\right)\left(-2\mathrm{i}\pi\exp(-z^2) + \int_{-\infty}^{+\infty}\frac{\mathrm{e}^{-t^2}}{t-z}\,\mathrm{d}t\right) = -\frac{1}{2}\exp\left(-\frac{x^2}{4a}\right)\Big(2\exp(-z^2) - w(z)\Big) \tag{C.9}$$

Finally, one obtains:

$$p_3 = -\frac{1}{2}\exp\left(-\frac{x^2}{4a}\right)w(-z) \tag{C.10}$$

For $x > 0$, corresponding to $\Im(z) < 0$, the deformation of the integration path does not cross the pole. One has:

$$p_3 = -\frac{\mathrm{i}}{2\pi}\exp\left(-\frac{x^2}{4a}\right)\int_{-\infty}^{+\infty}\frac{\mathrm{e}^{-t^2}}{t-z}\,\mathrm{d}t = -\frac{\mathrm{i}}{2\pi}\exp\left(-\frac{x^2}{4a}\right)[-\mathrm{i}\pi w(-z)] \tag{C.11}$$

which leads to the same formula than for $x < 0$. Finally, one has

$$p_3 = -\frac{1}{2}w(-z)\exp\left(-\frac{x^2}{4a}\right) = -\frac{1}{2}\exp\left(-\frac{\omega^2b^2}{4}\right)\exp\left(-\mathrm{i}\omega x\right)\operatorname{erfc}\left(\frac{x}{b} - \frac{\mathrm{i}\omega b}{2}\right) \tag{C.12}$$

C.2 Calculation of I

We detail the calculation of

$$I = \int_{-\infty}^{+\infty}\frac{\mathrm{e}^{-t^2}}{t-z}\,\mathrm{d}t \tag{C.13}$$

If $\Im(z) > 0$, the integral in Eq. (C.3) has a known solution given by Abramovitz *et al.* [98] in Eq. (7.1.4):

$$\int_{-\infty}^{+\infty}\frac{\mathrm{e}^{-t^2}}{t-z}\,\mathrm{d}t = \mathrm{i}\pi w(z) \quad \text{if} \quad \Im(z) > 0 \tag{C.14}$$

where $w(z) = \exp\left(-z^2\right)\operatorname{erfc}\left(-\mathrm{i}z\right)$ is the Faddeeva function and erfc is the complementary error function.

If $\Im(z) < 0$, one can write, using the change of variable $t' = -t$:

$$I = \int_{+\infty}^{-\infty} \frac{\mathrm{e}^{-t'^2}}{-t' - z} \, - \mathrm{d}t = - \int_{-\infty}^{+\infty} \frac{\mathrm{e}^{-t'^2}}{t' - z'} \, \mathrm{d}t \tag{C.15}$$

with $z' = -z$. As $\Im(z') = -\Im(z) > 0$, one can use Eq. (C.14) to write :

$$I = -\mathrm{i}\pi w(-z) \tag{C.16}$$

We can write overall:

$$\int_{-\infty}^{+\infty} \frac{\mathrm{e}^{-t^2}}{t - z} \, \mathrm{d}t = \mathrm{sign}[\Im(z)]\mathrm{i}\pi w(\mathrm{sign}[\Im(z)]z) \tag{C.17}$$

D Boundary conditions verification

In the numerical simulations performed in this work, Perfectly Matched Layers were applied to the last 30 grid points of the computational domain to absorb outgoing waves. This approach was combined with a numerical damping mask applied over the last 10 points, forcing all variables to zero. This additional treatment was necessary because the PML formulation in the presence of flow involves a parameter β, whose optimal value is difficult to determine. In fact, a dedicated stability analysis would be required to define it accurately; otherwise, spurious numerical instabilities may arise. This issue stems from the fact that acoustic waves can exhibit a negative phase velocity while maintaining a positive group velocity [8]. Without a precise variable transformation in the PML formulation, such waves are amplified instead of being absorbed, leading to instability.

To assess the effectiveness of the combined PML and numerical mask approach, two test simulations were performed for the unducted single fan free-field case for Configuration 1. Both simulations were conducted under identical conditions, except for the domain size. The baseline case consists of $241 \times 255 \times 334$ elements along the x-, y-, and z-directions, respectively, while the extended case includes $334 \times 334 \times 334$ elements. The cell spacing and CFL number are identical in both simulations, ensuring a valid comparison without altering other simulation parameters. The PML region extends over the last 30 grid points near the domain boundaries, while the numerical mask is applied to the last 10 points at the domain edges. A simulation time corresponding to two rotations was selected to ensure that any reflections from the boundaries of the larger domain could return to the probe locations used for recording the time signals. The temporal pressure fluctuations and Sound Pressure Levels were then compared to evaluate potential boundary effects that could affect the reliability of the numerical results.

Similarly, the comparison of SPL distributions along three lines on the $y = 0$ plane demonstrates complete overlap between the two simulations, as illustrated in Fig. D.2. These results confirm that the boundary conditions effectively damp outgoing waves, preventing any reflections.

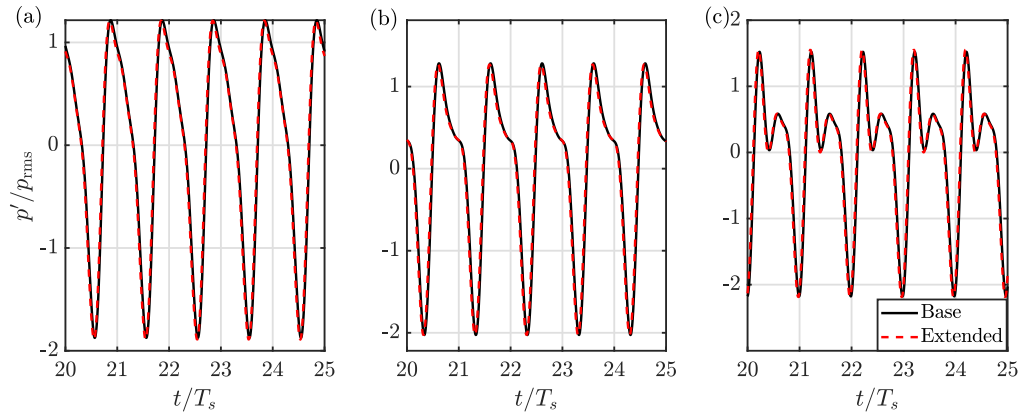

Figure D.1: Comparison of pressure fluctuation time signals from the baseline and extended simulations at three different locations at $y = 0$ for $\left(x/R_s, z/R_s\right)$ = (a) $(-0.23, 1.04)$, (b) $(-0.42, 1.41)$, and (c) $(-0.42, 1.73)$.

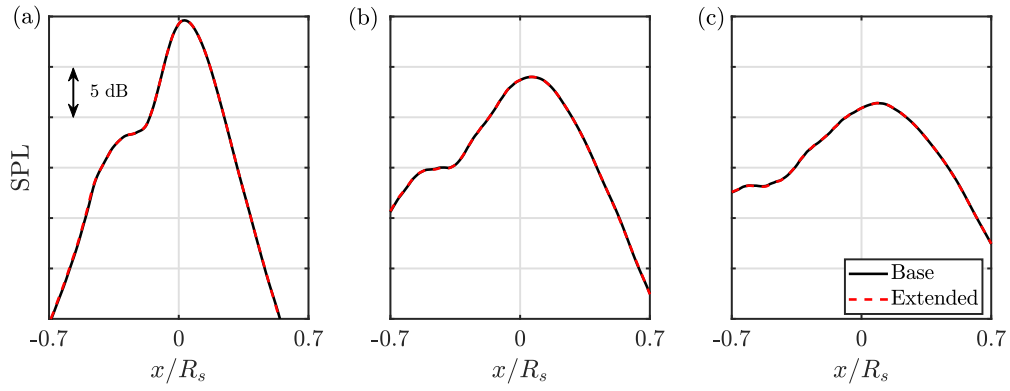

Figure D.2: Comparison of Sound Pressure Levels from the baseline and extended simulations at three different lines at $y = 0$: (a) $z/R_s = 1.04$, (b) $z/R_s = 1.41$, and (c) $z/R_s = 1.73$.

E Verification of acoustic pressure on the fuselage

As established in Chapter 4, under the conditions of total acoustic reflection and zero transmission in the obstacle, the numerical pressure signal recorded at wall points must correspond exactly to one half of the physical signal that would be expected at those locations. Furthermore, given that the fuselage is represented as a cylindrical surface embedded within a Cartesian computational mesh, a bilinear interpolation scheme was adopted to evaluate both the wall pressure signal and the requisite source terms for the reflection boundary condition.

The verification procedure is carried out as follows: the pressure signals recorded at the wall points are compared with those obtained at locations situated three grid points away from the wall in the wall-normal direction, at which the signal recovers its physical amplitude. The relationship between the two signals is expected to satisfy $p'(\mathbf{x}_\mathrm{w} + 3\Delta n\,\hat{\mathbf{n}}) = 2\,p'(\mathbf{x}_\mathrm{w})$, where $\mathbf{x}_\mathrm{w}$ denotes a point on the cylinder surface, $\hat{\mathbf{n}}$ is the outward unit normal to the wall at that point, and Δn is the local mesh spacing in the wall-normal direction. This confirms that the signal at the wall points is precisely half the expected value. It is worth noting that this condition is valid provided that the mesh spatial resolution is sufficiently fine relative to the acoustic wavelength, given that the volumetric source terms are distributed over a Gaussian support of half-width $b_w = \Delta x$.

The verification was performed at several locations on the fuselage surface at the final iteration of the simulation. A comparison of the acoustic pressure signals recorded at the wall and at three grid points away from the cylinder surface in the wall-normal direction is presented in Fig. E.1. Both signals are normalised with respect to the maximum absolute value of the pressure signal recorded at three grid points from the wall in the normal direction. The dashed line represents the wall signal multiplied by a factor of two, thereby enabling a direct comparison with the signal recorded at three grid points in the wall-normal direction.

In Fig. E.1(a), the signal is plotted along the x-axis for $\theta = \pi$, where it can be observed that the expected factor of two between the two signals is satisfied throughout the domain, with the exception of the region in the vicinity of the rotor plane at $x/R_s = 0$, where the pressure discontinuity associated with the shock waves is discretised over approximately five grid points.

In Fig. E.1(b), the pressure signal is plotted at $\theta = 0$, corresponding to the acoustic shadow zone, and the relationship is found to be satisfied across the entire domain, with a perfect agreement between twice the wall signal and the signal recorded at three grid points in the normal direction.

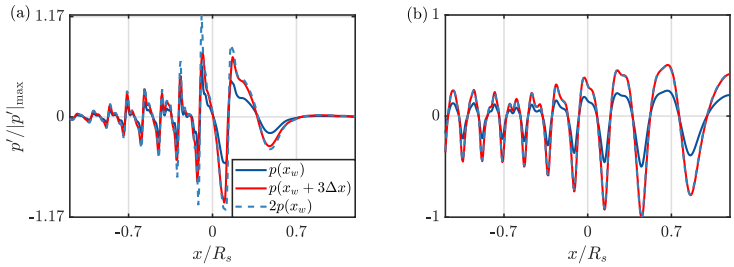

Figure E.1: Comparison between the acoustic pressure recorded at the wall, $p(x_w)$, the acoustic pressure evaluated at three mesh points from the wall, $p(x_w + 3\Delta x)$, and twice the wall acoustic pressure, for (a) $\theta = \pi$ and (b) $\theta = 0$.

An analogous comparison between the pressure signals, plotted as a function of the angular position θ, is performed on three distinct yz-planes located at $x/R_s = -0.7$, $x/R_s = 0$, and $x/R_s = 0.7$, corresponding to Figures E.2(a), E.2(b), and E.2(c), respectively. The expected factor of two between the wall pressure signal and the pressure signal recorded at three grid points in the wall-normal direction is observed to be satisfied over the majority of the domain. Localised discrepancies are nonetheless present in the regions where shock waves occur on the rotor plane and in the upstream portion of the domain, towards $\theta = \pi$, whereas a very good agreement between the two signals is obtained in the downstream region of the engine.

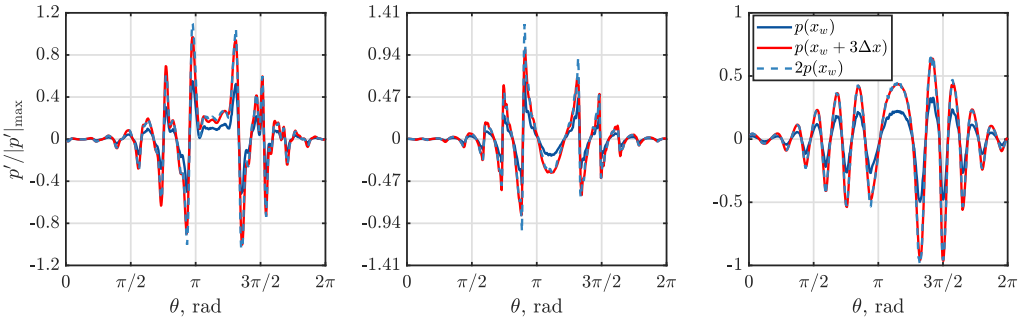

Figure E.2: Comparison between the acoustic pressure recorded at the wall, $p(x_w)$, the acoustic pressure evaluated at three mesh points from the wall, $p(x_w + 3\Delta x)$, and twice the wall acoustic pressure, for (a) $x/R_s = -0.7$, (b) $x/R_s = 0$, and (c) $x/R_s = 0.7$.

Bibliography

[1] International Air Transport Association (IATA). *Global Outlook for Air Transport: A World with Lower Oil Prices?* 2024.

[2] International Civil Aviation Organisation. *Manual on the Regulation of International Air Transport*. 3rd. 2018.

[3] International Civil Aviation Organisation. *Annex 16 - Environmental Protection - Volume I - Aircraft Noise*.

[4] L. Euler. "Principes généraux du mouvement des fluides". In: *Mémoires de l'académie des sciences de Berlin* (1757), pp. 274–315.

[5] C. Bogey and C. Bailly. "A family of low dispersive and low dissipative explicit schemes for flow and noise computations". en. In: *Journal of Computational Physics* 194.1 (2004), pp. 194–214.

[6] C. K. W. Tam and J. C. Webb. "Dispersion-Relation-Preserving Finite Difference Schemes for Computational Acoustics". In: *Journal of Computational Physics* 107.2 (1993), pp. 262–281.

[7] C. K. W. Tam, J. C. Webb, and Z. Dong. "A study of the short wave components in computational acoustics". In: *Journal of Computational Acoustics* 1.01 (1993), pp. 1–30.

[8] F. Q. Hu. "Development of PML absorbing boundary conditions for computational aeroacoustics: A progress review". In: *Computers & Fluids*. Turbulent Flow and Noise Generation 37.4 (2008), pp. 336–348.

[9] J. Berland, C. Bogey, and C. Bailly. "Low-dissipation and low-dispersion fourth-order Runge–Kutta algorithm". In: *Computers & Fluids* 35 (2006), pp. 1459–1463.

[10] R. Sabatini, O. Marsden, C. Bailly, and C. Bogey. "A numerical study of nonlinear infrasound propagation in a windy atmosphere". In: *The Journal of the Acoustical Society of America* 140 (2016), pp. 641–656.

[11] C. Bogey, N. de Cacqueray, and C. Bailly. "A shock-capturing methodology based on adaptative spatial filtering for high-order non-linear computations". In: *Journal of Computational Physics* 228 (2009), pp. 1447–1465.

[12] S. Pirozzoli. *CAA for Flow/Acoustic Interaction and High-Speed Flows with Shocks*. VKI Lecture Series 2005–2006, Von Karman Institute for Fluid Mechanics. 2006.

[13] C.-W. Shu. "Essentially non-oscillatory and weighted essentially non-oscillatory schemes". In: *Acta Numerica* 29 (2020), pp. 701–762.

[14] J.-P. Berenger. "A perfectly matched layer for the absorption of electromagnetic waves". In: *Journal of Computational Physics* 114.2 (1994), pp. 185–200.

[15] F. Q. Hu. "A stable, perfectly matched layer for linearized Euler equations in unsplit physical variables". In: *Journal of Computational Physics* 173.2 (2001), pp. 455–480.

[16] F. Q. Hu. "A perfectly matched layer absorbing boundary condition for linearized Euler equations with a non-uniform mean flow". In: *Journal of Computational Physics* 208.2 (2005), pp. 469–492.

[17] M. J. Lighthill. "On sound generated aerodynamically I. General theory". In: *Proceedings of the Royal Society of London. Series A. Mathematical and Physical Sciences* 211.1107 (1952), pp. 564–587.

[18] M. J. Lighthill. "On sound generated aerodynamically II. Turbulence as a source of sound". In: *Proceedings of the Royal Society of London. Series A. Mathematical and Physical Sciences* 222.1148 (1954), pp. 1–32.

[19] J. E. Ffowcs Williams and D. L. Hawkings. "Sound generation by turbulence and surfaces in arbitrary motion". In: *Philosophical Transactions of the Royal Society of London. Series A, Mathematical and Physical Sciences* 264.1151 (1997), pp. 321–342.

[20] F. Farassat and M. K. Myers. "Extension of Kirchhoff's formula to radiation from moving surfaces". In: *Journal of Sound and Vibration* 123.3 (1988), pp. 451–460.

[21] K. S. Brentner and F. Farassat. "Analytical Comparison of the Acoustic Analogy and Kirchhoff Formulation for Moving Surfaces". In: *AIAA Journal* 36.8 (1998), pp. 1379–1386.

[22] X. Gloerfelt, C. Bailly, and D. Juvé. "Direct computation of the noise radiated by a subsonic cavity flow and application of integral methods". In: *Journal of Sound and Vibration* 266.1 (2003), pp. 119–146.

[23] N. de Cacqueray and C. Bogey. "Noise of an Overexpanded Mach 3.3 Jet: Non-Linear Propagation Effects and Correlations with Flow". In: *International Journal of Aeroacoustics* 13.7-8 (2014), pp. 607–632.

[24] A. Emmanuelli, D. Dragna, S. Ollivier, and P. Blanc-Benon. "Characterization of topographic effects on sonic boom reflection by resolution of the Euler equations". In: *The Journal of the Acoustical Society of America* 149.4 (2021), pp. 2437–2450.

[25] A. Langenais, F. Vuillot, C. Peyret, G. Chaineray, and C. Bailly. "Assessment of a Two-Way Coupling Methodology Between a Flow and a High-Order Nonlinear Acoustic Unstructured Solvers". In: *Flow Turbulence and Combustion* 101 (2018), pp. 681–703.

[26] K. W. Thompson. "Time dependent boundary conditions for hyperbolic systems". In: *Journal of Computational Physics* 68.1 (1987), pp. 1–24.

[27] K. W. Thompson. "Time-dependent boundary conditions for hyperbolic systems, II". In: *Journal of Computational Physics* 89.2 (1990), pp. 439–461.

[28] T. J Poinsot and S. K Lele. "Boundary conditions for direct simulations of compressible viscous flows". In: *Journal of Computational Physics* 101.1 (1992), pp. 104–129.

[29] G. Daviller, G. Oztarlik, and T. Poinsot. "A generalized non-reflecting inlet boundary condition for steady and forced compressible flows with injection of vortical and acoustic waves". In: *Computers & Fluids* 190 (2019), pp. 503–513.

[30] J. Thisse, C. Polacsek, J. Mayeur, S. Khelladi, X. Gloerfelt, and A. Lafitte. "Numerical Simulations of Shock-Wave Propagation in Turbofan Intakes". In: *22nd AIAA/CEAS Aeroacoustics Conference*. 2016.

[31] M. Daroukh, C. Polacsek, and A. Chelius. "Shock wave generation and radiation from a turbofan engine under flow distortion". In: *AIAA Journal* 58.2 (2020), pp. 787–801.

[32] F. Nicoud. "Defining Wave Amplitude in Characteristic Boundary Conditions". In: *Journal of Computational Physics* 149.2 (1999), pp. 418–422.

[33] T. Colonius. "Modeling Artificial Boundary Conditions for Compressible Flow". In: *Annual Review of Fluid Mechanics* 36 (2004), pp. 315–345.

[34] K. Maeda and T. Colonius. "A source term approach for generation of one-way acoustic waves in the Euler and Navier–Stokes equations". In: *Wave Motion* 75 (2017), pp. 36–49.

[35] J. E. Ffowcs Williams. "Review Lecture - Anti-sound". In: *Proceedings of the Royal Society of London. A. Mathematical and Physical Sciences* 395 (1984), pp. 63–88.

[36] O. Kirkeby and P. A. Nelson. "Reproduction of plane wave sound fields". In: *The Journal of the Acoustical Society of America* 94.5 (1993), pp. 2992–3000.

[37] S. M. Kuo and D. R. Morgan. "Active noise control: a tutorial review". In: *Proceedings of the IEEE* 87.6 (1999), pp. 943–973.

[38] S. Ginter, M. Liebler, E. Steiger, T. Dreyer, and R. E. Riedlinger. "Full-wave modeling of therapeutic ultrasound: Nonlinear ultrasound propagation in ideal fluids". In: *Journal of the Acoustical Society of America* 111 (2002), pp. 2049–2059.

[39] J. Krimmel, T. Colonius, and M. Tanguay. "Simulation of the effects of cavitation and anatomy in the shock path of model lithotripters". In: *Urological Research* 38 (2010), pp. 505–518.

[40] K. Okita, K. Ono, S. Takagi, and Y. Matsumoto. "Development of high intensity focused ultrasound simulator for large-scale computing". In: *International Journal for Numerical Methods in Fluids* 65 (2011), pp. 43–66.

[41] A. D. Pierce. *Acoustics: An Introduction to Its Physical Principles and Applications*. Cham: Springer International Publishing, 2019.

[42] M. F. Hamilton and D. T. Blackstock. *Nonlinear acoustics*. Springer Nature, 2024.

[43] G. Coco, D. Dragna, C. Bailly, and H. Posson. "Injection of acoustic waves via volumetric sources on a control surface for computational aeroacoustics". In: *The Journal of the Acoustical Society of America* 159.2 (2026), pp. 1151–1162.

[44] C. S. Peskin. "Flow patterns around heart valves: A numerical method". In: *Journal of Computational Physics* 10.2 (1972), pp. 252–271.

[45] B. E. Griffith and N. A. Patankar. "Immersed Methods for Fluid–Structure Interaction". In: *Annual Review of Fluid Mechanics* 52.Volume 52, 2020 (2020), pp. 421–448.

[46] D. Goldstein, R. Handler, and L. Sirovich. "Modeling a No-Slip Flow Boundary with an External Force Field". In: *Journal of Computational Physics* 105.2 (1993), pp. 354–366.

[47] E.M. Saiki and S. Biringen. "Numerical Simulation of a Cylinder in Uniform Flow: Application of a Virtual Boundary Method". In: *Journal of Computational Physics* 123.2 (1996), pp. 450–465.

[48] P. Angot, C.-H. Bruneau, and P. Fabrie. "A penalization method to take into account obstacles in incompressible viscous flows". In: *Numerische Mathematik* 81.4 (1999), pp. 497–520.

[49] M. Specklin and Y. Delauré. "A sharp immersed boundary method based on penalization and its application to moving boundaries and turbulent rotating flows". In: *European Journal of Mechanics - B/Fluids* 70 (2018), pp. 130–147.

[50] J. Mohd-Yusof. "For Simulations of Flow in Complex Geometries". In: *Annual Research Briefs*. Center for Turbulence Research, Stanford University, 1997.

[51] E. A. Fadlun, R. Verzicco, P. Orlandi, and J. Mohd-Yusof. "Combined Immersed-Boundary Finite-Difference Methods for Three-Dimensional Complex Flow Simulations". In: *Journal of Computational Physics* 161.1 (2000), pp. 35–60.

[52] K. Taira and T. Colonius. "The immersed boundary method: A projection approach". In: *Journal of Computational Physics* 225.2 (2007), pp. 2118–2137.

[53] M. Rich and S. S. Blackman. *A method for Eulerian fluid dynamics*. Tech. rep. 1963.

[54] J. A. Viecelli. "A method for including arbitrary external boundaries in the MAC incompressible fluid computing technique". In: *Journal of Computational Physics* 4.4 (1969), pp. 543–551.

[55] J. A. Viecelli. "A computing method for incompressible flows bounded by moving walls". In: *Journal of Computational Physics* 8.1 (1971), pp. 119–143.

[56] K. A. Kurbatskii and C. K. W. Tam. "Cartesian Boundary Treatment of Curved Walls for High-Order Computational Aeroacoustics Schemes". In: *AIAA Journal* 35.1 (1997), pp. 133–140.

[57] R. Verzicco. "Immersed Boundary Methods: Historical Perspective and Future Outlook". In: *Annual Review of Fluid Mechanics* 55.Volume 55, 2023 (2023), pp. 129–155.

[58] C. Chung and P. J. Morris. "Acoustic Scattering from Two- and Three-Dimensional Bodies". In: *Journal of Computational Acoustics* 06.03 (1998), pp. 357–375.

[59] O. A. Laik and P. J. Morris. "Direct Simulation of Acoustic Scattering by Two- and Three-Dimensional Bodies". In: *Journal of Aircraft* 37.1 (2000), pp. 68–75.

[60] S. Lee, K. S Brentner, and P. J Morris. "Assessment of time-domain equivalent source method for acoustic scattering". In: *AIAA journal* 49.9 (2011), pp. 1897–1906.

[61] S. Lee. "Review: The Use of Equivalent Source Method in Computational Acoustics". In: *Journal of Computational Acoustics* 25.01 (2017), p. 1630001.

[62] O. Marsden, C. Bogey, and C. Bailly. "High-Order Curvilinear Simulations of Flows Around Non-Cartesian Bodies". In: *Journal of Computational Acoustics* 13.04 (2005), pp. 731–748.

[63] S. Bilbao. "Modeling impedance boundary conditions and acoustic barriers using the immersed boundary method: The one-dimensional case". In: *The Journal of the Acoustical Society of America* 153.4 (2023), pp. 2023–2036.

[64] S. Bilbao. "Immersed boundary methods in wave-based virtual acoustics". In: *The Journal of the Acoustical Society of America* 151.3 (2022), pp. 1627–1638.

[65] S. Bilbao. "Modeling impedance boundary conditions and acoustic barriers using the immersed boundary method: The three-dimensional case". In: *The Journal of the Acoustical Society of America* 154.2 (2023), pp. 874–885.

[66] C. K. W. Tam. *Computational aeroacoustics: a wave number approach*. Cambridge University Press, 2012.

[67] C. K. W. Tam and J. C. Hardin. *Second computational aeroacoustics (CAA) workshop on benchmark problems*. National Aeronautics and Space Administration, Langley Research Center, 1997.

[68] D. Lewis, C. Perrin, and F. Falissard. "Tonal Noise Predictions of a Generic Open-Fan Based on a Hybrid URANS Approach". In: *30th AIAA/CEAS Aeroacoustics Conference*. American Institute of Aeronautics and Astronautics, 2024.

[69] D. B. Hanson. "Shielding of prop-fan cabin noise by the fuselage boundary layer". In: *Journal of Sound and Vibration* 92.4 (1984), pp. 591–598.

[70] D. B. Hanson and B. Magliozzi. "Propagation of propeller tone noise through a fuselage boundary layer". In: *Journal of Aircraft* 22.1 (1985), pp. 63–70.

[71] H. Y. Lu. "Fuselage boundary-layer effects on sound propagation and scattering". In: *AIAA journal* 28.7 (1990), pp. 1180–1186.

[72] G. McAninch and J. W. Rawls Jr. "Effects of boundary layer refraction and fuselage scattering on fuselage surface noise from advanced turboprop propellers". In: *22nd Aerospace Sciences Meeting*. 1984.

[73] P. L. Spence. "Effects of fuselage boundary layer on noise propagation from advanced propellers". In: *Journal of Aircraft* 29.6 (1992), pp. 1005–1011.

[74] I. V. Belyaev. "The effect of an aircraft's boundary layer on propeller noise". In: *Acoustical Physics* 58.4 (2012), pp. 387–395.

[75] H. Brouwer. "The scattering of open rotor tones by a cylindrical fuselage and its boundary layer". In: *22nd AIAA/CEAS Aeroacoustics Conference*. 2016.

[76] J. Gaffney, A. McAlpine, and K. Michael. "Sound radiation of fan tones from an installed turbofan aero-engine: fuselage boundary-layer refraction effects". In: *22nd AIAA/CEAS Aeroacoustics Conference*. 2016.

[77] H. Schippers and J. A. Wensing. "Hybrid computational model for noise propagation through a fuselage boundary layer". In: *AIAA journal* 34.9 (1996), pp. 1785–1792.

[78] D. M. Rouvas and A. McAlpine. "An Analytical Model of Sound Refraction By the Fuselage Boundary Layer for Fan Tone Radiation from a Turbofan Aero-engine". In: *28th AIAA/CEAS Aeroacoustics 2022 Conference*. 2022.

[79] J. Dierke, R. Ewert, J. Delfs, C. Stoehr, and M. Rose. "The effect of a boundary layer on engine noise propagating to the fuselage at flight conditions". In: *19th AIAA/CEAS Aeroacoustics Conference*. 2013.

[80] M. Siefert, J. Delfs, and B. Caruelle. "Refraction and scattering in high Mach number boundary layers". In: *17th AIAA/CEAS Aeroacoustics Conference (32nd AIAA Aeroacoustics Conference)*. 2011.

[81] M. S. Howe. "The role of surface shear stress fluctuations in the generation of boundary layer noise". In: *Journal of Sound and Vibration* 65.2 (1979), pp. 159–164.

[82] D. C. Pridmore-Brown. "Sound propagation in a fluid flowing through an attenuating duct". In: *Journal of Fluid Mechanics* 4.4 (1958), pp. 393–406.

[83] S. Priebe, T. Wood, J. Yi, and A. Mousavi. "Large Eddy Simulation of an Open Rotor Fan Blade". In: *Proceedings of the ASME Turbo Expo 2022: Turbomachinery Technical Conference and Exposition*. 2022.

[84] S. Priebe, E. Jourdan, A. Mousavi, R. Karve, S. Chakrabarti, L. D'Aquila, J. Yi, M. Alhawwary, V. Bharadwaj Ananthan, K. Ramakrishnan, and T. Wood. "Large Eddy Simulation of an Open Fan Blade at Full-Scale Reynolds Number". In: *Journal of Turbomachinery* 147.7 (2024).

[85] V. Daydé-Thomas, C. Polacsek, S. Fauqueux, X. Gloerfelt, and J. Mardjono. "Tone noise characterization of an open-fan engine using source-mode integral formulations". In: *30th AIAA/CEAS Aeroacoustics Conference*. 2024.

[86] M. Lorteau, T. Le Garrec, and V. Daydé-Thomas. "Open Fan Noise Confinement Effects in a Closed Wind-Tunnel: Numerical Methodology and Evaluation". In: *30th AIAA/CEAS Aeroacoustics Conference*. 2024.

[87] D. Lewis, C. Perrin, and F. Falissard. "Tonal Noise Predictions of a Generic Open-Fan Based on a Hybrid URANS Approach". In: *30th AIAA/CEAS Aeroacoustics Conference*. 2024.

[88] C. Polacsek, V. Daydé-Thomas, S. Fauqueux, J. Mardjono, and M Descamps. "Acoustic characteristics of an open-fan model from semi-analytical predictions and wind tunnel tests". In: *Forum Acusticum Euronoise*. 2025.

[89] S. Proskurov, J. Dierke, A. Stürmer, R. Ewert, and J. Delfs. "Acoustic Simulation for Wing Mounted Open Rotor and Stator". In: *AIAA SCITECH 2025 Forum*. 2025.

[90] L. Cambier, S. Heib, and S. Plot. "The Onera elsA CFD software: input from research and feedback from industry". In: *Mechanics & Industry* 14 (2013), pp. 159–174.

[91] A. L. Polyakova. "Plane sound wave of finite amplitude in a moving medium". In: *Doklady Akademii Nauk*. Vol. 137. 6. Russian Academy of Sciences. 1961, pp. 1347–1349.

[92] A. H. Nayfeh, B. S. Shaker, and J. E. Kaiser. "Computation of nonlinear one-dimensional waves in near-sonic flows". In: *AIAA Journal* 16.11 (1978), pp. 1154–1159.

[93] N. J. Walkington and W. Eversman. "A numerical model of acoustic choking, Part I: Shock free solutions". In: *Journal of Sound and Vibration* 90.4 (1983), pp. 509–526.

[94] E. R. Van Driest. "On Turbulent Flow Near a Wall". In: *Journal of the Aeronautical Sciences* 23.11 (1956), pp. 1007–1011.

[95] J. Gaffney, A. McAlpine, and M. J. Kingan. "Fuselage boundary-layer refraction of fan tones radiated from an installed turbofan aero-enginea)". In: *The Journal of the Acoustical Society of America* 141.3 (2017), pp. 1653–1663.

[96] J. Gaffney, A. McAlpine, and M. J. Kingan. "A theoretical model of fuselage pressure levels due to fan tones radiated from the intake of an installed turbofan aero-engine". In: *The Journal of the Acoustical Society of America* 143.6 (2018), pp. 3394–3405.

[97] I. S. Gradshteyn and I. M. Ryzhik. *Table of Integrals, Series, and Products*. 7th. Academic Press, 2007.

[98] M. Abramowitz and I. A. Stegun. *Handbook of Mathematical Functions with Formulas, Graphs, and Mathematical Tables*. Tenth printing. Series 55. National Bureau of Standards Applied Mathematics, 1972.